Laser-Driven Anti-Resonant Fibers: Acceleration and Phase Space Manipulation of Relativistic Electron Beams

Dissertation

zur Erlangung des Doktorgrades
an der Fakultät für Mathematik, Informatik und Naturwissenschaften
Fachbereich Physik
der Universität Hamburg

vorgelegt von

Luca Genovese

aus Italy

Hamburg
2022

Gutachter/innen der Dissertation	Dr. Ralph Aßmann Prof. Dr.Wolfgang Hillert
Zusammensetzung der Prüfungskommission	Prof. Dr. Daniela Pfannkuche Dr. Ralph Aßmann Prof. Dr. Wolfgang Hillert Prof. Dr. Günter Sigl Dr. Klaus Flöttmann
Vorsitzende/r des Prüfungskommission	Prof. Dr. Daniela Pfannkuche
Datum der Disputation	26 July 2022
Vorsitzender des Fach-Promotionsausschusses Physik	Prof. Dr. Wolfgang Hansen
Leiter des Fachbereichs Physik	Prof. Dr. Günter Sigl
Dekan der Fakultät für Mathematik, Informatik und Naturwissenschaften	Prof. Dr. Heinrich Graener

Abstract

In this work of thesis, applications of photonic crystal fiber to advanced accelerator concepts are investigated. Due to the high damage threshold of dielectric material in the optical regime, dielectric laser accelerators can support $\mathcal{O}(\mathrm{GV/m})$ as accelerating field which motivates to investigate laser-driven dielectric structures.

Laser-driven hollow core photonic bandgap (PBG) fibers were proposed by Lin in 2001 as high-gradient accelerators. The central defect in the transversely periodic lattice supports an accelerating mode which collinearly propagates with the ultra-relativistic electron beam for synchronous acceleration. The optical frequencies in such dielectric laser accelerators motivate a sensitivity and tolerance study to overcome manufacturing imperfections. Moreover, the defining a tolerance range in which the modes properties in the fiber can be recovered tuning the laser wavelength seems to be very useful for the manufacturing where a tolerance range of 10% is generally required. Finally, in this thesis, the propagation characteristics of Lin fibers are discussed and it is found that small-bandwidth ($\approx$ ns) pulses would be needed for efficient acceleration over longer distances.

However, the central core diameter is comparable to the driving wavelength which makes both the technical manufacturing of the fiber and its use with conventional charged beams challenging. In behalf of the collaboration established with Philipp Russell division at Max Planck Institute in Erlangen, more recent anti-resonant fibers (ARFs) were investigated.

In conventional beam manipulation techniques, the interaction between electron beams and laser is provided by magnetic undulators which unfortunately require a balance between the electron beam energy, undulator parameters and laser wavelength. In this thesis we propose a novel scheme using laser-driven large-core anti-resonant optical fibers to manipulate electron beams. The accelerating TM_{01} and the dipole HE_{11} mode are investigated. In the former case, energy gain and large keV-level energy modulations can be achieved while maintaining the overall electron beam quality. Further, it is shown that with larger field strengths $\mathcal{O}(100\ \mathrm{MV/m})$ the resulting transverse forces can lead to the production of microbunch trains with a periodicity of the driving wavelength. Also, we investigate the application of the transverse dipole HE_{11} mode and find it suitable to support time-domain electron beam diagnostics with sub-attosecond resolutions.

Finally, a preliminary test of the feasibility of this novel beam manipulation techniques has been performed. At ARES/SINBAD laser laboratory, an experimental optical setup was implemented to investigate the laser beam coupling efficiency and laser induced damage threshold of the end-face of the ARF.

Zusammenfassung

In dieser Abschlussarbeit werden Anwendungen von photonischen Kristallfasern für fortschrittliche Beschleunigerkonzepte untersucht. Aufgrund der hohen Zerstörungsschwelle von dielektrischem Material im optischen Bereich können dielektrische Laserbeschleuniger $\mathcal{O}$(GV/m) als Beschleunigungsfeld unterstützen, was zur Untersuchung von lasergetriebenen dielektrischen Strukturen motiviert.

Lasergesteuerte Hohlkernfasern mit photonischer Bandlücke (PBG) wurden 2001 von Lin als Hochgradientenbeschleuniger vorgeschlagen. Der zentrale Defekt im transversal periodischen Gitter unterstützt eine Beschleunigungsmode, die sich kollinear mit dem ultra-relativistischen Elektronenstrahl ausbreitet, um eine synchrone Beschleunigung zu erreichen. Die optischen Frequenzen, in solchen dielektrischen Laserbeschleunigern, motivieren eine Empfindlichkeits- und Toleranzstudie, um Herstellungsmängel zu überwinden. Darüber hinaus scheint die Festlegung eines Toleranzbereichs, in dem die Modeneigenschaften in der Faser durch Abstimmung der Laserwellenlänge wiederhergestellt werden können, sehr nützlich für die Herstellung zu sein, bei der im Allgemeinen ein Toleranzbereich von 10% erforderlich ist. Schließlich werden in dieser Arbeit die Ausbreitungseigenschaften von Lin-Fasern erörtert, und es wird festgestellt, dass für eine effiziente Beschleunigung über größere Entfernungen, Pulse mit kleiner Bandbreite (ca. ns) benötigt würden. Der zentrale Kerndurchmesser ist jedoch vergleichbar mit der Antriebswellenlänge, was sowohl die technische Herstellung der Faser als auch ihre Verwendung mit konventionellen geladenen Strahlen zu einer Herausforderung macht. Im Rahmen der Zusammenarbeit mit der Abteilung von Philipp Russell am Max-Planck-Institut in Erlangen wurden neuere antiresonante Fasern (ARFs) untersucht.

In konventionellen Strahlmanipulationstechniken wird die Wechselwirkung zwischen Elektronenstrahlen und Laser durch magnetische Undulatoren gewährleistet, die leider ein Gleichgewicht zwischen der Elektronenstrahlenergie, den Undulatorparametern und der Laserwellenlänge erfordern. In dieser Arbeit schlagen wir ein neuartiges Verfahren zur Manipulation von Elektronenstrahlen mit Hilfe von lasergesteuerten antiresonanten optischen Fasern mit großem Kern vor. Der beschleunigende TM_{01}- und der Dipol HE_{11}-Modus werden analysiert. Im ersten Fall können Energiegewinn und große Energiemodulationen im keV-Bereich erreicht werden, während die Qualität des Elektronenstrahls insgesamt erhalten bleibt. Außerdem wird gezeigt, dass bei größeren Feldstärken $\mathcal{O}$(100 MV/m) die resultierenden Querkräfte zur Erzeugung von Mikrobunch-Zügen mit einer Periodizität der Antriebswellenlänge führen können. Außerdem analysieren wir die Anwendung der transversalen Dipol-HE_{11}-Mode und stellen fest, dass sie geeignet ist, die Diagnostik von Elektronenstrahlen im Zeitbereich mit Auflösungen im Sub-Attosekundenbereich zu unterstützen.

Zum Schluss, wurde ein vorläufiger Test der Machbarkeit dieser neuartigen Strahlmanipulationstechniken durchgeführt. Im ARES/SINBAD-Laserlabor wurde ein optischer Versuchsaufbau implementiert, um die Effizienz der Laserstrahlkopplung und die laserinduzierte Schadensschwelle der Endfläche des ARF zu untersuchen.

Contents

List of Figures

List of Tables

1
Introduction

The need to build particle accelerators capable of increasing the energy of particles is a logical consequence of the demand from high-energy physics to test different theories. When Rutherford predicted the possibility of splitting an atom in the early 1920s, he encouraged Cockcroft and Walton to develop the first DC accelerator. Since then, various technologies have been developed to accelerate the electron beams, as shown in the milestone Figure 1.1. Conventional accelerators not only play a fundamental role in investigating elementary physics, but also have considerable applications in fields such as biology, chemistry and medicine where attosecond pulses of X-ray generated by modern electron-based light sources can provide tools for probing electronic structures of matter with attosecond and picometer resolution in time and space, respectively.

Modern conventional accelerator are linacs based on radio-frequency (RF) technology. High charged beam in the order of nano Coulomb are routinely accelerate by centimeter long driven wavelengths with a repetition rate below 100 Hz. In circular machine such as cyclotrons and betatrons, charged particle beams are first accelerated in a linac and then injected into a storage ring producing synchrotron-radiation losses. The most brilliant storage ring-based X-ray source is PETRAIII. The 6 GeV nC electron beam with high transverse beam quality is injected into 2.3 km long storage ring producing transversely coherent radiation with pulse length $\mathcal{O}$(ps).

Because of electric breakdown, modern conventional RF particle accelerators provide acceleration gradient up to $\sim 100\,\mathrm{MV/m}$. In the past decades, superconducting radio-frequency (SRF) cavities has been investigated for their lower power dissipation compared to normal RF technologies. Niobium cavities in a liquid helium bath allow for a quality factor of two or three orders of magnitude higher than the normal RF. At European XFEL electrons are accelerated up to 17 GeV within ≈1.7 km SRF long accelerator at 10 Hz repetition rate. The pC electron beam is then injected into undulator resulting in the emission of coherent X-rays with pulse lengths below 100 fs. However, to achieve the superconductive status and prevent the cavity quenches a well-designed cryogenic system needs to be developed increasing the costs and the facilities scale.

In order to counteract this trade-off between energy and costs, new advanced acceleration technologies have been addressed. Thus, international projects such as ACHIP, LUX, ARIES and ATHENE are being set up to demonstrate the possibility of considerably reducing the size and cost of accelerators by adopting technologies such as laser-driven dielectric grating structures and plasma. Plasma-based accelerators e.g. plasma wakefield acceleration (PWFA) and laser-plasma wakefield acceleration (LWFA) are able to provide an accelerating gradient up to three orders of magnitude higher than RF cavities. In 2014, Leemans and coworkers [12] demonstrated that in a 9-cm plasma cell 6 pC charged beam achieves 4.2 GeV when driven by 16 Joule laser

at 1 Hz. Thus, PeraWatt laser system are needed to power a plasma cell to produce GeV high charged beam. KALDERA is one of the new projects at DESY which aims to provide a new class of laser system delivering 3 J pulse energy at 1 kHz repetition rate.

In the other hand, at UCLA dielectric laser accelerators (DLAs) have been demonstrated to support an accelerating gradient of 300 MV/m [13, 14, 15]. A dielectric grating structure driven by µJ pulsed laser are able to provide hundreds MV/m as accelerating gradient when fC charged sub-fs electron bunches at high repetition rates $\mathcal{O}$(MHz) is injected. ACHIP experiment at SINBAD/ARES aims to demonstrate energy modulation and net energy gain of sub-femtosecond relativistic fC charged beam delivered by ARES linac [16] injected into dielectric grating structure powered by µJ laser system at kHz repetition rate.

In the DLAs however, the side-coupled structures rely on spatial harmonics which lead to evanescent modes in the accelerating channel, thereby limiting the structure apertures to approximately the laser wavelength. This restriction makes the widespread use of dielectric structures in conventional radiofrequency accelerators challenging; mainly due to typical electron beam emittances being $\mathcal{O}$(100 nm).

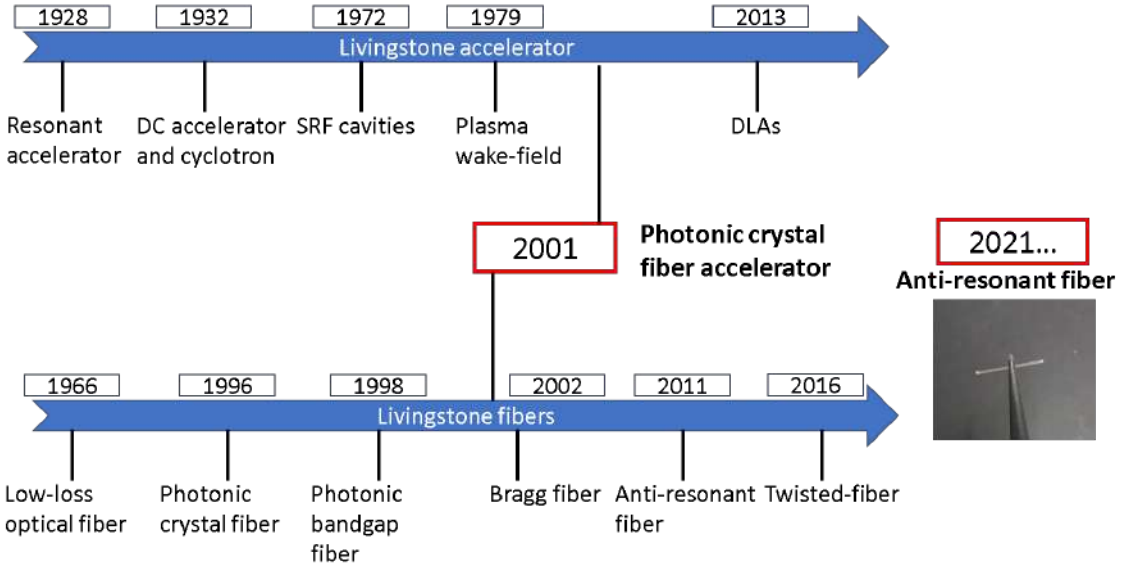

Figure 1.1: Accelerators and optical fibers milestone: accelerators and fibers followed two different evolutionary paths until Lin proposed the first photonic band-gap fiber accelerator in 2001.

Since 1970, when the possibility of transmitting data through an optical fiber with reduced attenuation was first demonstrated, different types of fibers have followed (see Figure 1.1). While initially their purpose was mainly for telecommunications, new generations of fibers are capable of confining light in a hollow core by means of photonic band-gap and anti-resonat effect, attracting the scientific community. Since the intensity of electromagnetic fields is concentrated in an air-filling core, photonic crystal fibers have been and are still being studied for numerous applications such as high-power pulse delivery and gas-based nonlinear optics.

The first encounter between accelerators and photonic crystal fibers took place in 2001, when E. Lin [17] theoretically demonstrated that a properly designed photonic bandgap fiber supports TM_{01}-like modes which propagate with the electron beam. However, like grating structures, the central core diameter is also comparable to the wavelength, making both the technical im-

plementation of the fiber and its use with conventional charged beams challenging. At author knowledge, proof of principle was never realized and thus building on E. Lin first effort, carried out at SLAC, this thesis aims to revive that project and to reintroduce the fiber to the world of accelerators with greater vehemence.

More recently, anti-resonant fibers (ARFs) were invented, supporting low-loss transmission of enormously broadband spectra [18, 19]. Unlike Lin-fibers, ARFs have relatively large apertures which relax the required electron-beam parameters for efficient transmission through the fibers. Furthermore, compared to other types of hollow-core fibers, the larger core sizes ($D \gg \lambda$) facilitates the propagation of mJ-level pulses due to reduced losses. Loss factors have significantly improved in recent years due to novel designs and improved fabrication techniques, achieving $\approx$1 db/km [20, 21].

In this thesis, we investigate the application of laser-driven photonic crystal fiber with electron beams. We especially find that energy gain and high-quality energy modulations can be imparted with the monopole (TM_{01}) mode inside an ARF using μJ-level laser pulses. In addition, by utilizing larger laser energies, we discover that a microbunch train can be produced at the periodicity of the laser wavelength by filtering the strongly focused or defocused electrons with a collimator. We also report on the use of the dipole (HE_{11}) mode to generate microbunch trains and to find it suitable to support sub-attosecond temporal measurement resolutions of charged beams. A collaboration with Philip Russell's division at Max Planck Institute in Erlangen has been established. In behalf of this collaboration, field maps of the ARF supported modes and ARF sample have been investigated and first coupling-damage test at SINBAD/ARES laser laboratory has been performed.

In chapter 2 of this dissertation, the ARES/SINBAD linac as well as the undergoing experiments will be briefly introduced. In addition, some of the simulation codes used in this thesis will be presented.

Chapter 3 provides an overview of the theory of accelerator physics. Here the most important electron beam parameters will be presented.

In Chapter 4 photonic crystal fibers will be introduced. A description of the modes supported by a cylindrically-symmetric waveguide commonly used to approximate the mode propagating into a fiber are reviewed. Finally, the most important guidance mechanism as well as the fabrication technique are shown in this chapter.

First results on photonic band gap fiber driven by a 2 µm laser are discussed in chapter 5. A tolerance study of the accelerating mode properties into such a fiber have been carried out. A trade-off between the mode quality factor and the attenuation loss along with a preliminary coupling study is shown.

Based on these findings, anti-resonant fiber suitable for SINBAD/ARES laser system is presented in chapter 6. The interaction between electron beam and both accelerating and fundamental hybrid mode will be investigated. A novel scheme to produce energy gain, energy modulation and microbunch train is discussed for the TM_{01} mode. Furthermore, femtosecond bunch trains and sub-attosecond temporal resolutions with laser-driven anti-resonant fibers is reported.

Finally, in chapter 7 the description of the preliminary anti-resonant fiber coupling experiment at SINBAD/ARES laser laboratory is reported. The purpose of this chapter is to provide a documentation for future experiments. Fiber cleaving and experimental setup are featured. The maximum supported laser input power limits the achievable field strength inside the fiber. To investigate this limitation a laser induced damage threshold test has been implemented.

2

Overview of the SINBAD/ARES linac

2.1 SINBAD facility

Located at the heart of DESY in the former DORIS tunnel, a long-term dedicated accelerator research and development facility SINBAD has been established and is being under development [22, 23]. SINBAD (Short Innovative Bunches and Accelerator at DESY) will host several experiments independently such as cutting edge conventional S-Band accelerator, laser driven plasma wake field accelerators and dielectric laser accelerators. In addition, research on advanced bunch compression techniques and novel diagnostic ideas is carried out. An overview of the SINBAD facility is given in Figure 2.1. At the time of writing the first two experiments, ARES and AXSIS are already operational.

ARES is a normal conducting S-Band linac aiming to provide 155 MeV sub-fs (sub-femtosecond to dozens of femtoseconds) low-charge (0.5 to 30 pC) electron bunches with a timing stability of ≈10 fs rms and repetition rate of 50 Hz [24, 25]. The high-energy low-charge bunches may be then injected into experimental areas for testing novel acceleration techniques (dielectric structures or novel diagnostic concepts). An overview of the linac will be presented in the following section.

AXSIS (Frontiers in Atto-second X-ray Science: Imaging and Spectroscopy) [26, 27] aims to develop a compact X-ray light source based on a THz-driven dielectric loaded waveguide for electron acceleration and subsequent inverse Compton scattering (ICS). A laser system operating at 1 kHz as repetition rate will be used to drive the photocathode gun producing the electrons and to generate the single-cycle THz pulses accelerating the electrons up to 1 MeV. It is also used to produce the multi-cycle THz pulse which is injected into a dielectric loaded waveguide (DLW) linac to boost the electron energy up to 20 MeV. Finally, both the laser and electron beam are used to generate X-rays in the range of 4-14 keV by ICS. This energy range is especially useful for research on biological samples and processes. The facility is currently under commissioning.

KALDERA (Kilowatt Laser at DESY for Revolutionary Accelerator) plans to build up a new class of laser system aiming to deliver 3 J in 30 fs at 1 kHz for plasma acceleration. LUX was the first plasma accelerator to produce soft X-ray at DESY using a TW laser injected into a hydrogen gas target. The electron bunches accelerated by the plasma wake are then injected into an undulator resulting in the aforementioned X-rays which last few fs enabling the investigation of processes on ultra-fast timescale. LUX II has the purpose to build upon the milestone achieved by LUX [28].

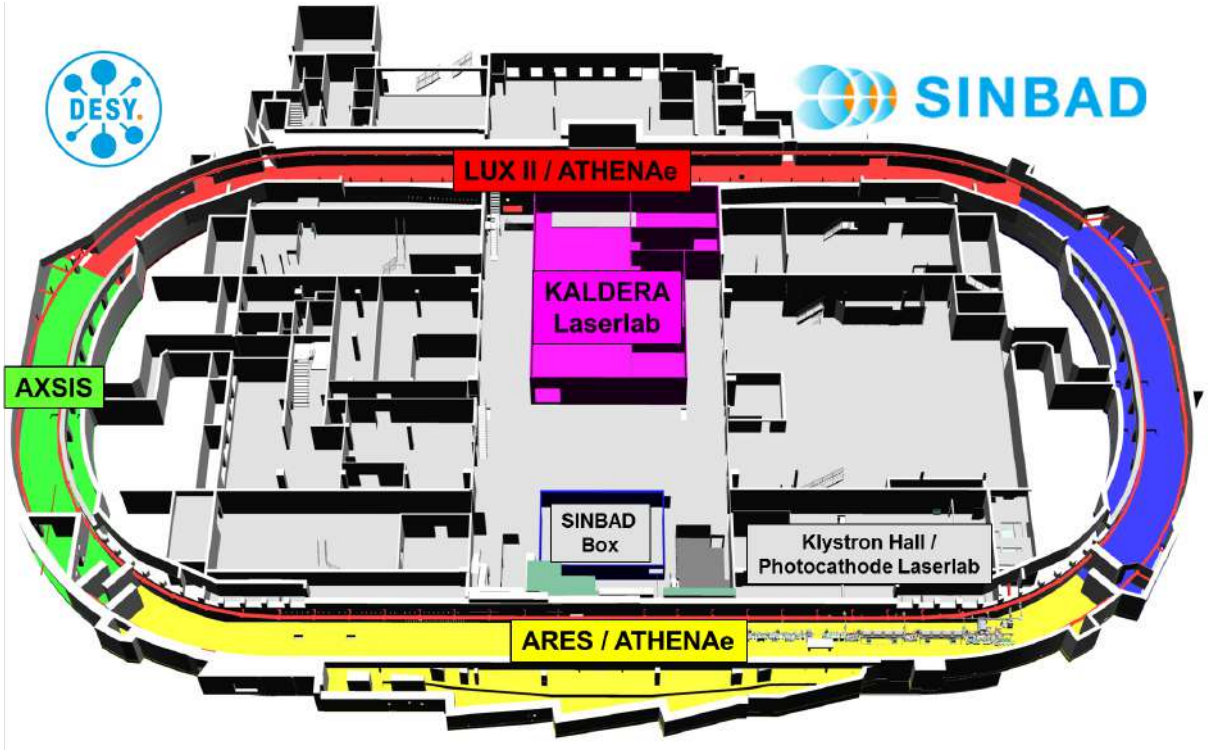

Figure 2.1: Overview of the SINBAD facility at DESY. The foreseen experiments ARES, AXSIS, KALDERA and LUX II will occupy different sections of the SINBAD tunnel.

2.2 ARES linac

ARES (Accelerator Research Experiment at SINBAD) is a conventional normal conducting linear accelerator. After final commissioning ARES will support the production of up to ≈155 MeV sub-femtosecond electron bunches via two S-band (≈3 GHz) travelling wave structures with a timing jitter $\mathcal{O}$(10 fs) and repetition rate of 50 Hz [29]. As shown in the layout in Figure 2.2, the accelerating structures are followed by an experimental area which hosts the ACHIP project (see later for details) but could be adapted for DLWs and first proof of principle experiments involving photonic crystal fiber for beam manipulation. Downstream of the experimental chamber, a bunch compressor is installed enabling sub-fs bunch compression [30, 24]. Beyond the bunch compressor, a Polarix X-Band transverse deflecting structure (TDS) is located and will measure the longitudinal beam profile with sub-fs resolution [31]. Its variable streaking direction will allow the characterization of the 6D phase-space [32].

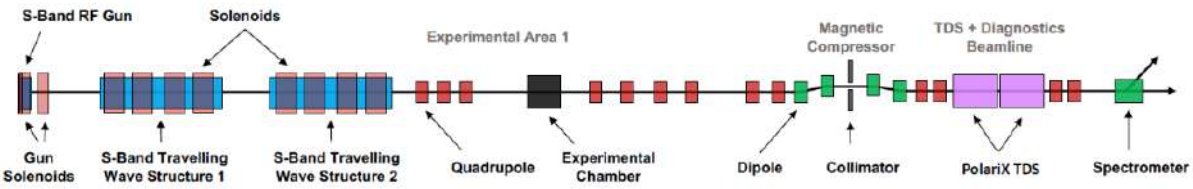

Figure 2.2: Layout of the ARES linac. Taken from [1]

2.2.1 Photoinjector

Electron bunches are provided by the RF photoinjector. The used 1 mJ Yb-doped photocathode laser is a commercial PHAROS-SP-200 operating at the fundamental wavelength of 1030 nm. It provides pulses with FWHM duration in the range of 180 fs to 10 ps and illuminates either Cs_2Te or Mo cathode with the fourth harmonic. The gun has an in-vacuum cathode exchange system which guarantees the possibility to change target between metallic and semiconductor material. Electrons are emitted based on the photoelectric effect [33]. The photo-emitted electrons (charge ranges between 0.3 pC and 30 pC) are then accelerated in a 1.6 cell S-band gun by a maximum accelerating gradient of 80 MV/m achieving a bunch mean energy of ≈4 MeV. In the gun region a solenoid can be used for transverse focusing and emittance compensation into the linac [34].

2.2.2 Linac section

Downstream the RF gun, several screens are installed allowing for the characterization of the beam in the transverse plane. A low energy dipole can be used for energy measurements. Furthermore, a Faraday Cup and DaMon (Dark current Monitor [35]) enable destructive and non-destructive bunch charge measurements, respectively. The diagnostic section is followed by two accelerating structures operating at a frequency of ∼3 GHz. Each travelling wave structure is 4.2 m long and powered by a 45 MW RF station providing a maximum energy gain per cavity of 75 MeV operating on crest [22]. However, to reach the ultra-short bunches, the first cavity needs to be operated off crest allowing for velocity bunching. Operating off crest the electron bunch will be longitudinally chirped and since it is not yet at relativistic energy the head and the tail will have different velocity leading to a longitudinal focusing. Since the beam is slightly slower than the phase velocity of the travelling wave it experiences phase slippage from zero-crossing back to the accelerating phase. In such a way it is both chirped and accelerated, simultaneously [36]. As it is injected into the second cavity operating on crest, the already relativistic electron bunch will be further accelerated up to ∼100 MeV. Another approach to produce microbunch trains consists into operating both TWSs at relative phase of 55° and then injecting the beam into bunch compressor. It should be mentioned that each TWS is surrounded by four independently adjustable solenoids which will be used to focus the beam and to compensate the space-charge defocusing forces.

2.2.3 Experimental Area

Following the linac section, a 4 m long Experimental Area (EA) has been installed and will host ACHIP-related experiments as well as other experiments involving acceleration and phase space manipulation in dielectric structures. Concepts, simulations and design of the ACHIP-related experiments are explained in detail in ref. [16, 37]. The layout of the experimental area section includes a quadrupole triplet for final focusing, an undulator and a compact permanent magnetic chicane for producing microbunch trains. Furthermore, EA also includes an ultra-high vacuum experimental chamber and an optical table over which the 2 µm drive laser side-illuminates the dielecric grating structure inside the chamber. The laser system is installed in the ARES cathode laser laboratory. The beam is transported through an almost 30 m long beam line to the experimental chamber.

2.2.4 Bunch compressor and diagnostic section

Downstream EA, several beam diagnostics measure the final beam quality; screens, magnets and spectrometer enable for high energy beam characterization.

The bunch compressor installed at ARES consists of 4 magnets with a maximum magnetic field of 0.5 T. The central magnets are located on a translation stage allowing for a wide range of momentum compaction R_{56}. For a relativistic energy beam (100 MeV) is anticipated an R_{56} between 0 cm and 8.8 cm. As the maximum travel range is around 20 cm, a dedicated vacuum system has been implemented. The design specifications are detailed in [30, 24].

A transverse deflection structure (TDS) provides bunch length properties by streaking the beam and the longitudinal phase space after the spectrometer. Undergoing a longitudinal intra-bunch coordinate-dependent transverse force, the bunch is streaked and then imaged onto a scintillating screen allowing for measurement of bunch length and longitudinal properties. A conventional TDS can provide beam information only in the streaking direction. For that reason, a novel polarizable X-band TDS (PolariX-TDS) has been installed at ARES. PolariX will provide variable polarization of the TE_{11} mode into the RF cavity allowing for streaking the beam in different directions. The utilization of a spectrometer reconstructs the longitudinal phase space. Structure design and reconstruction considerations are detailed in [38, 39, 31]

2.3 Accelerator on a CHip International Program - ACHIP

As member of the ACHIP collaboration, DESY performs related experiments at ARES. The Accelerator on a CHip International Program is a 5-year project (now extended until 2023) funded by the Gordon and Betty Moore Foundation [40]. Its purpose is to develop and demonstrate a prototype of an all-optical particle accelerator on a microchip for relativistic [13] and non-relativistic [14] electrons reaching MeV energy gain. Among different dielectric structures such as 3D photonic crystals, photonic bandgap fibers and grating structures, the latter is one of the most studied being suitable for acceleration, radiation generation [41] and beam diagnostics [42].

Currently in the EA chamber at ARES, one dielectric grating sample along with a thin film YAG screen are installed. The screen is used to measure the beam profile at the interaction point of the electron bunches from the linac and the 2 µm laser from the optical table, which side-illuminates the sample. In order to optimize the experimental campaign, the ACHIP experiment has been split into two stages. In the first stage, a relativistic electron bunch (100 MeV) from the linac will be further accelerated in the side-illuminated grating structure. Since DLA structure periodicity is 2 µm, a net-acceleration in the grating is anticipated for an rms bunch length <1 fs. ARES will provide sufficient short electron bunches using velocity bunching techniques [23, 43]. Longer electron beam will experience different laser phase producing energy-loss or energy modulation as already observed by other groups [13]. Also, due to the small DLA periodicity, stable drive laser to electron phase is needed. In particular, a sub-fs stability is required which is very challenging.

In order to address this issue, the second stage will add a microbunching setup. It consists of an undulator and a permanent magnetic chicane, which is planned to be installed by the end of 2022 and placed between the triplet of quadrupole after the TWSs and the experimental chamber. In the undulator, the incoming electron bunch interacts with a copropagating laser

beam, which will imprint an energy modulation on the bunch given by [16, 43, 44]:

$$\Delta\gamma = \sqrt{\frac{P_L}{P_0}}\frac{2KL_uJ}{\gamma\omega_0}\cos k_L s \tag{2.1}$$

where P_L, ω_0 and k_L are the power, the waist and the wave number of the laser, P_0 ≈8.7 GW, K and L_u are the undulator parameter and the undulator length, $J = J_0(\zeta) - J_1(\zeta)$ with $\zeta = \frac{K^2}{2(2+K^2)}$ and s is the longitudinal position of the electron in the electron bunch.

The cosine-like energy modulated beam is then injected into the magnetic chicane to form a density modulation. Passing through the chicane, particles that have the negative energy chirp are compressed, while particles with the positive energy chirp are decompressed, resulting a conversion of the energy modulation into a particle density distribution modulation. The utilization of the same laser for driving both the undulator and the DLA will bring intrinsic phase synchronization achieving a negligible phase jitter between the microbunch train and the laser illuminating the grating structure. The microbunches will have a spacing of 2 µm and a <1 fs as rms length.

2.4 Accelerator Research and Innovation for European Science and Society - ARIES

The SINBAD facility will host external researchers by collaborations with other groups and also via the ARIES Transnational Access Activities program [45, 46]. ARIES (Accelerator Research and Innovation for European Science and Society) is an Integrating Activity project co-founded by European Commission for a duration of four years until April 2022. CERN and 41 different partners, as well as DESY, are part of this program. It aims to develop and research of European particle accelerator supporting innovative technologies which can find applications in accelerator and industry. Due to the ever-increasing demand for high-energy accelerators, research in new technologies and materials is of paramount importance.

2.5 Current status of ARES

At the time of this publication, as discussed in the previous section, the main components for ARES and ACHIP experiments are already installed. The first ≈3.5 MeV electron beam from the ARES gun was observed on October 30th 2019. RF conditioning of the ARES gun, as well as the two linac structures was completed at the end of October 2020. The design energy of 155 MeV was achieved operating on crest in both TWSs. Using A Molybdenum cathode, the FWHM energy spread at the end of the beam line measured by the high energy diagnostic was determined to be 0.056% for a bunch with ≈1.5 pC of charge.

Currently ARES linac runs stably over long operation time while TDS and bunch compressor are already installed and will be commissioned soon. The electron bunch parameters provided by the ARES linac are summarized in Table 2.1.

Table 2.1: ARES linac electron beam parameters

	Value
beam energy [MeV/c]	3.5-160
beam charge [pC]	0.2-30
normalized transverse emittance [μm]	$<$0.5
bunch length [fs]	$>$30

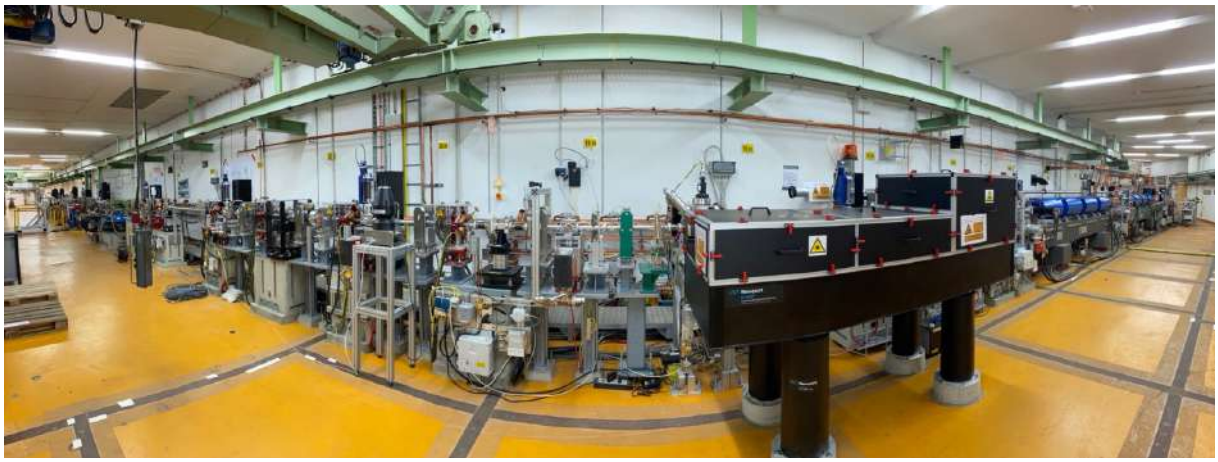

Figure 2.3: Picture of the current status of the ARES/SINBAD linac. Courtesy of F. Mayet

2.6 Simulation codes

In recent decades, high performance computing (HCP) has greatly increased, enabling excellent results to be achieved in simulations that are increasingly faithful to the real experiment. Since the experiment can be simulated more realistically than in the past, the technologies and structures of future accelerators can be studied in advance and adapted to optimize the desired results. Naturally, a trade-off has to be considered between time consumption and accuracy of the simulations. In addition to Python scripts written to run simulations automatically and allow fast data analysis, four codes are used in this thesis, some to provide field maps, others to visualize mode propagation in the fibers, and still others to track particles. In this thesis, ASTRA is used for particle tracking simulation and to achieve the working points needed for different fiber-electron beam applications CUDOS, VSIM are mainly used to test the mode propagation and confinement inside the fiber. COMSOL has been used for carrying out a designed fiber matching the purpose of acceleration and energy manipulation of an electron beam.

2.6.1 VSim

VSim [47] is a multiphysics simulation tool which allow for computing electrodynamics in the presence of metallic and dielectric structures along with charged particles. Using the Vorpal computational engine, Vsim can be run in electromagnetic mode using a finite-difference time domain (FDTD) algorithm while charged particles can be simulated by particle-in-cell (PIC) code. The simulation can be set up using VSimComposer, which enables to add different shapes and materials as well as fields and particles. VSimComposer writes the input file which will be used by the Vorpal computational engine. However, it is also possible to write the input file

directly in order that the user has the full control over the physics, shapes and materials in the simulation. This method and mainly the FDTD algorithm has been used in this work.

2.6.2 ASTRA

ASTRA (A Space charge TRacking Algorithm) [48] is a free of charge program package, written in Fortran 90. ASTRA tracks particles interacting with external electromagnetic fields which can be included by importing external field maps allowing the simulation of RF cavities and dielectric structures. A non-adaptive Runge-Kutta integration method of fourth order is used for tracking where the time step range is defined by user depending on the electromagnetic field's wavelength and space charge. In this thesis the maximum time step has been evaluated by converging studies and also external field maps have been used to simulate the propagating mode inside the fiber by superposition of two standing waves resulting in a travelling wave.

2.6.3 CUDOS

The CUDOS MOF Utilities [49] is a publicly available software, first released in 2004 by the University of Sydney [50]. The code is based on the results of ref. [51, 52] which treats both solid- and air-core microstructure optical fibers (MOFs) by the multipole method. The electric and magnetic field are expressed in Fourier-Bessel series centered on each hole applying boundary conditions. The solutions for each hole (fiber's capillary) are then matched together. As the input frequency is set, the code searches for modes with different effective refractive index in a range fixed by the user. Furthermore, it calculates the real and the imaginary part of the propagation constant providing information on the phase velocity of the modes and the confinement losses, respectively.

2.6.4 COMSOL

COMSOL Multiphysics [53] is a platform used for simulation in scientific research as well as in manufacturing. The user can define geometry, material properties and the physics describing the studied phenomena. For modelling the phenomena COMSOL has default physics interfaces suggesting the recommended solver to discretize the system of partial different equations by finite element method (FEM) or boundary element method (BEM).

The fiber geometry, as well as propagating modes, have been simulated and optimized using COMSOL. Thanks to the fruitful collaboration established with Max-Planck-Institute in Erlangen [54], these simulations have been carried out by Gordon Wong and then adapted to ASTRA format by the author.

3

Introduction to accelerators physics

In this chapter an overview of the fundamental physics behind accelerators will be presented. The most important electron beam parameters and their dependencies will be introduced summarizing concepts which can be found in various accelerator books as well as in CERN and USPAS (U.S. Particle Accelerator School) lessons, cited step by step where used in the chapter.

3.1 The equations of motion for a single charged particle

The dynamics of a single charged particle e under the effect of electromagnetic fields $(\vec{E}, \vec{B})$ are described by the Lorentz force

$$\vec{F_L} = e\Big(\vec{E} + \vec{v} \times \vec{B}\Big). \tag{3.1}$$

From classical mechanics, the change of momentum and kinetic energy for a particle is given by:

$$\Delta\vec{p} \quad = \int \vec{F_L}\ dt \tag{3.2}$$

$$\Delta E_{\text{kin}} \quad = \int \vec{F_L} \cdot d\vec{s}. \tag{3.3}$$

Substituting the Lorentz force in the kinetic energy and transforming $d\vec{s} \rightarrow \vec{v}dt$, yields

$$\Delta E_{\text{kin}} = e \int \vec{E} \cdot d\vec{s} + e \int (\vec{v} \times \vec{B}) \cdot \vec{v}dt \tag{3.4}$$

The equation above shows that the electric field changes the kinetic energy of the charge while the magnetic field deflects particle's trajectory by changing its momentum vector. In fact the first term of eq. 3.4 produces the acceleration of a particle copropagating with the field; the vector product of the second term is always zero indicating the deflection of the particle trajectory due to the presence of the magnetic field and ruling out any acceleration contribution. Knowing the interaction length between charge and electric field and its amplitude, the variation of the kinetic energy is calculated by the integration of eq. 3.4.

To determine the path of an electron in a magnetic field, it is required to know the change in particle momentum. For a particle travelling with a relativistic velocity $\vec{\beta} = \frac{\vec{v}}{c}$, rest mass m and Lorentz-factor $\gamma = \frac{1}{\sqrt{1-\beta^2}}$, its momentum $\vec{p} = \gamma m\vec{v}$ can be derived with respect to the time,

yielding the equation of motion

$$\frac{d\vec{p}}{dt} = m\Big(\gamma\frac{d\vec{v}}{dt} + \gamma^3\frac{\beta}{c}\frac{dv}{dt}\vec{v}\Big), \tag{3.5}$$

where the second term originate from the derivative of the Lorentz-factor $\frac{d\gamma}{dt} = \frac{d\gamma}{d\beta}\frac{d\beta}{dt} = \gamma^3\frac{\beta}{c}\frac{dv}{dt}$. Eq.3.5 can be split into parallel and transverse forces which propagate parallel to the propagation of electron and perpendicular to it, respectively:

$$\vec{F}_{\parallel} = \frac{d\vec{p}_{\parallel}}{dt} = m\gamma^3\frac{d\vec{v}_{\parallel}}{dt}, \tag{3.6}$$

$$\vec{F}_{\perp} = \frac{d\vec{p}_{\perp}}{dt} = m\gamma\frac{d\vec{v}_{\perp}}{dt}. \tag{3.7}$$

The above equations are achieved by considering that for a force parallel to the particle propagation the time derivative of the unity vector $\hat{v}$ is zero, $\frac{d\vec{v}}{dt} = \frac{dv}{dt}\hat{v}$ and $1 + \beta^2\gamma^2 = \gamma^2$; on the other hand for the perpendicular forces $\frac{dv}{dt} = 0$.

Eq. 3.6 and 3.7 show that passing through an electromagnetic field the trajectory of a relativistic particle depends on the direction of the force w.r.t. the direction of particle. This difference between parallel and perpendicular acceleration will be crucial in this thesis due to the heavy impact on the dynamics of the electrons propagating through the fiber.

In a linear accelerator or in a synchrotron, the general task is to transport charged particles along a desired path in the beam transport system while accelerating. The magnetic field is used for bending the particle along a predefined ideal path, the so called *orbit*, over which all the particles of an electron beam should move. To describe deviation of a particle from this ideal orbit it is common to introduce the Frenet-Serret coordinate system $K = (x, y, s)$ which follows the trajectory of a particle along the accelerator moving with no deviation from the designed speed, position, or direction. Here the x-s and y-s are the horizontal and vertical plane, respectively.

As shown in detail in references [55, 2, 56], transforming the Lorentz force from Cartesian to Frenet-Serret coordinates and assuming several common simplifications such as magnetic field perpendicular to the particle trajectory, no coupling of the motion between the vertical and the horizontal direction and constant particle velocity, it leads to the well-known equations of motion [2, 56]

$$x''(s) + \Big(\tfrac{1}{R^2(s)} - k(s)\Big)x(s) = \frac{1}{R(s)}\delta, \tag{3.8}$$

$$y''(s) + k(s)y(s) = 0, \tag{3.9}$$

where x is the displacement w.r.t. the orbit s, $x' = \frac{dx}{ds}$ is the divergence angle, $\delta = \frac{p-p_0}{p_0}$ is the relative momentum spread w.r.t. the reference momentum p_0, $1/R$ and k are the dipole and quadrupole strength, respectively. The equations 3.8 form the basis of calculations for the particles travelling through linear beam optics.

3.1.1 Transfer matrix

Assuming the hard-edge model for a magnetic field of the magnet structure, which means an abrupt interruption of the field at the edge of the magnet and considering a constant field along

the beam axis will simplify the eq. 3.8. Using the further assumption that all the particles have the same reference momentum p_0 and thus $\delta = 0$, eq. 3.8 may be written as [56]:

$$u'' + K(s)u = 0, \tag{3.10}$$

where u indicates the x or y coordinates and $K(s) = \frac{1}{R^2(s)} - k(s)$ or $K(s) = k(s)$. Eq. 3.10, also called Hill's equation, is a linear second order differential equation and thus it is possible use the matrix formalism for its solution:

$$\mathbf{x} = \mathbf{M} \cdot \mathbf{x_0}, \tag{3.11}$$

with $\mathbf{x} = (x, x')$ and $\mathbf{x_0} = (x_0, x_0')$ the final and initial 1D transverse phase space coordinate.

The 2×2 transfer matrix $\mathbf{M}$ will have different elements for each optics used in the beam line; in the drift space where magnet sections are absent, i.e. $\frac{1}{R} = k = 0$, it is given by

$$\mathbf{M}_{\text{drift}} = \begin{pmatrix} 1 & s \\ 0 & 1 \end{pmatrix}, \tag{3.12}$$

where s is the trajectory distance in a drift section. It is clear that particle divergence is constant while the displacement will change $x = x_0 + x_0' s$. The transfer matrix for a focusing ($\frac{1}{R} = 0, k < 0$) and defocusing quadrupole ($\frac{1}{R} = 0, k > 0$) are

$$\begin{aligned} \mathbf{M}_{\text{Q}}^{(\text{foc})} &= \begin{pmatrix} \cos(\sqrt{|k|}s) & \frac{1}{\sqrt{|k|}} \sin(\sqrt{|k|}s) \\ -\sqrt{|k|} \sin(\sqrt{|k|}s) & \cos(\sqrt{|k|}s) \end{pmatrix}, \\ \mathbf{M}_{\text{Q}}^{(\text{def})} &= \begin{pmatrix} \cosh(\sqrt{k}s) & \frac{1}{\sqrt{k}} \sinh(\sqrt{k}s) \\ \sqrt{k} \sinh(\sqrt{k}s) & \cosh(\sqrt{k}s) \end{pmatrix}. \end{aligned} \tag{3.13}$$

From eq.3.8, a quadrupole will focus in one direction and defocus in the direction perpendicular to the focusing plane. Finally, in the deflective plane the particle trajectory in a dipole magnet ($k = 0$) is given by

$$\mathbf{M}_{\text{D}} = \begin{pmatrix} \cos(\frac{s}{R}) & R \sin(\frac{s}{R}) \\ -\frac{1}{R} \sin(\frac{s}{R}) & \cos(\frac{s}{R}) \end{pmatrix}. \tag{3.14}$$

In this case the dipole is focusing the particle toward the orbit but with a relatively weak effect compared to the quadrupole, because $\frac{1}{R^2} \ll k$ [2].

So far, we considered only particle with reference momentum, i.e. $\delta = 0$ but it is worth to note that the momentum of the particle w.r.t. the reference momentum plays an important role in the dynamics because the effect of the magnetic field on the particle depends on it. Furthermore, using the matrix formalism it is possible to describe the particle trajectory along the entire beam transport system. Thus considering the chromaticity, the evolution of the particle in the five-dimensional phase space $\mathbf{x} = (x, x', y, y', \delta)^T$, along the beam line under the effect of n magnetic

elements, including drift space, is given by matrix multiplication:

$$\begin{pmatrix} x \\ x' \\ y \\ y' \\ \delta \end{pmatrix} = \mathbf{M}_n \cdot \mathbf{M}_{n-1} \cdot \mathbf{M}_{n-2} \cdots \mathbf{M}_1 = \begin{pmatrix} x_0 \\ x'_0 \\ y_0 \\ y'_0 \\ \delta \end{pmatrix}. \tag{3.15}$$

3.1.2 Courant-Snyder parameters

For a periodic focusing system, i.e. $\frac{1}{R} = 0$, $\delta = 0$ and $k(s) < 0$, the equations of motion 3.8 simplify to

$$x''(s) - k(s)x(s) = 0. \tag{3.16}$$

The so-called phase-amplitude form of the solution is given by

$$x(s) = A\sqrt{\beta(s)}\cos\big(\phi(s) + \phi_0\big), \tag{3.17}$$

where $\beta(s)$ and $\phi(s)$ are the amplitude function (also known as beta function) and phase function both position dependent, while A and ϕ_0 are the initial constants of integration. Eq.3.17 describes the betatron oscillations performed by a particle around the orbit while the phase advanced function $\phi(s)$ between the initial and final longitudinal position s is

$$\phi(s) = \int_0^s \frac{d\sigma}{\beta(\sigma)}. \tag{3.18}$$

It is common to define other two function

$$\alpha(s) = -\tfrac{1}{2}\tfrac{d\beta(s)}{ds}, \quad \gamma(s) = \tfrac{1+\alpha(s)^2}{\beta(s)}. \tag{3.19}$$

The quantities $(\alpha(s), \beta(s), \gamma(s))$ are known as Courant-Snyder parameters or Twiss parameters. Under these definitions, it can be easily shown that eq.3.17 and its derivative with respect to s satisfy the equation of the phase space ellipse

$$\gamma(s)x^2(s) + 2\alpha(s)x(s)x'(s) + \beta(s)x'^2(s) = A^2. \tag{3.20}$$

The above equation describes an ellipse with area πA^2 in the transverse phase-space $x - x'$.

3.1.3 Emittance and Liouville's theorem

To describe the trajectory of a particle beam composed by a large number of particles, it is useful to introduce tools and definitions which allow for description of particle beam as a whole. In this scenario emittance and Liouville's theorem play an important role.

In order to introduce quantities act to describe the entire beam in the phase-space, the definition of mean square values of a function $f(x)$ with a discrete distribution of n particles is given by

$$\big\langle f(x)^2 \big\rangle = \frac{\sum_{i=1}^n f(x)^2}{n} - \Big(\frac{\sum_{i=1}^n f(x)}{n}\Big)^2. \tag{3.21}$$

and for a Gaussian distribution, which will be assumed in this work, the root mean square coincides with the standard deviation

$$f(x)_{rms} = \sqrt{\langle f(x)^2 \rangle} = \sigma_{f(x)}. \tag{3.22}$$

The emittance is an important property for the transverse beam dynamics because it describes the average spread of the electron beam in the phase-space. In the $x-p_x$ phase space the so-called geometric emittance is given by [57]

$$\epsilon_{\text{rms}} = \frac{1}{m_0 c \bar{p_z}} \sqrt{\langle x^2 \rangle \langle p_x^2 \rangle - \langle x p_x \rangle^2}, \tag{3.23}$$

where m_0 and c are the electron rest mass and the speed of light, respectively and $\bar{p_z}$ is the average longitudinal momentum. Now, for particles which obey to the canonical equation of motions, i.e. under the influence of conservative force, the Liouville's theorem states that the density of phase space for a given non-interacting particle distribution is a conserved quantity. In other words, the beam emittance stays constant with respect to time if the particles are under effect of conservative forces and processes like acceleration, particle losses, electromagnetic radiation or damping don't occur; the shape of the ellipse in the phase space will change along the orbit s but the area will be conserved.

In accelerators, where particles are affected by an accelerating gradient, the emittance is not conserved. As the momentum p_z increases, the transverse momentum p_x will stay constant while the emittance decrease as $1/p_z$ (so-called adiabatic damping) [58]. In that case it is useful to define the normalized rms emittance:

$$\epsilon_{n,rms} = \beta\gamma\epsilon_{rms} \tag{3.24}$$

In the $x - x'$ phase space (referred as trace-space), the trace-space emittance $\epsilon_{\text{tr,rms}}$ is defined as [57]:

$$\epsilon_{\text{tr,rms}} = \sqrt{\langle x^2 \rangle \langle x'^2 \rangle - \langle x x' \rangle^2}. \tag{3.25}$$

As for the normalized rms space emittance, it is possible to define the normalized trace-space emittance:

$$\epsilon_{n,tr,rms} = \beta\gamma\epsilon_{tr,rms} \tag{3.26}$$

In case of small energy spread and divergence, the trace emittance and the normalized rms emittance are equal. In this thesis, the emittance values, which comes from the simulation results, are given as normalized rms emittance.

It should be noted that the Louville's theorem applies to the 6D phase space where the conjugate coordinates are $(x, p_x, y, p_y, z, \delta)$. Under the assumptions required above regarding the conservative force, the coordinates system is Hamiltonian and thus Liouville theorem is valid. Fortunately, the trace phase space emittance is also conserved under the conditions that solenoid field and accelerating field are absent and a small energy spread is taken in count [34].

3.1.4 Beam envelope

The emittance is a powerful tool because it can be used to describe the behavior of the whole beam and not only the single particle. Eq.3.20, considering the definition of the emittance given

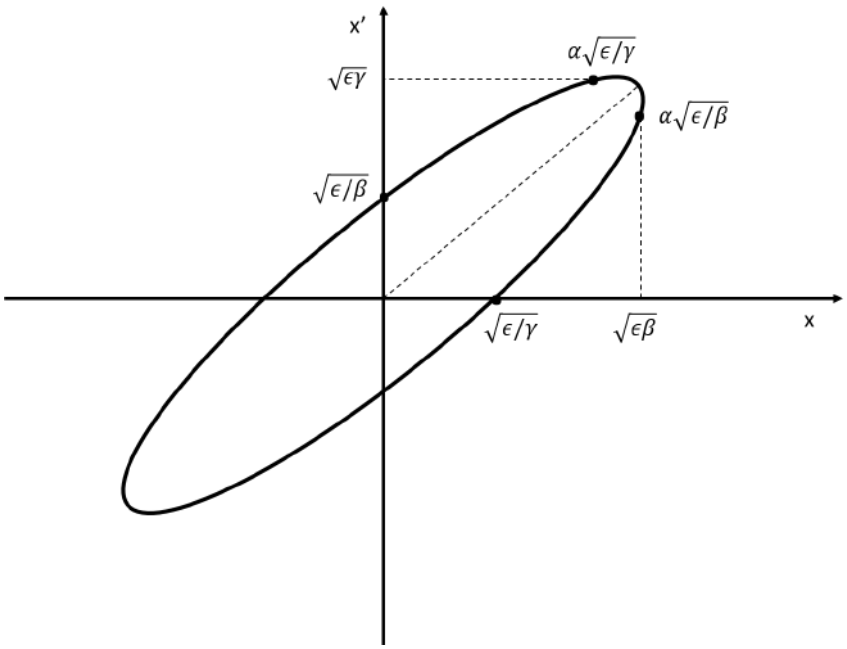

Figure 3.1: Phase space ellipse for a particle in x-x' plane and relevant Twiss parameters.

in 3.25, becomes

$$\gamma(s)x^2(s) + 2\alpha(s)x(s)x'(s) + \beta(s)x'^2(s) = \epsilon_{\mathrm{tr,rms}} \tag{3.27}$$

with the Twiss parameters:

$$\beta(s) = \frac{\langle x^2 \rangle}{\epsilon_{\mathrm{tr,rms}}}, \quad \gamma = (s)\frac{\langle x'^2 \rangle}{\epsilon_{\mathrm{tr,rms}}}, \quad \alpha(s) = -\frac{\langle xx' \rangle}{\epsilon_{\mathrm{tr,rms}}} \tag{3.28}$$

It can be shown that the phase ellipse is uniquely determined and the Twiss parameters are related by

$$\gamma(s) = \frac{1 + \alpha^2(s)}{\beta(s)}. \tag{3.29}$$

In a beam each electron lies on a conserved space ellipse. The tilt of the ellipse in Figure 3.1 is given by $-\alpha/\beta$, usually expressed in mrad, and indicates the correlated transverse momentum spread. If the beam is divergent, the correlated beam divergence will be positive, otherwise it is negative and the beam convergent.

Based on the definition of the rms emittance, it is possible to define the beam envelope as:

$$\sigma(s) = \sqrt{\epsilon_{\mathrm{tr,rms}}\beta(s)} \tag{3.30}$$

The beam envelope allows to calculate the beam size through the beamline (see Fig. 3.2); it is based on the emittance and betatron function: the first is a constant of motion and is related to the beam distribution; the latter contains information on the beam lattice and varies with the position along the beamline. Knowing the optical parameters at initial position in the beam line $(\beta_0, \alpha_0, \gamma_0)^T$, it is possible to calculate them at another point in the lattice using matrix formalism. Let us consider an initial $\mathbf{x_0} = (x_0, x_0')^T$ and final trajectory $\mathbf{x} = (x, x')^T$ vector

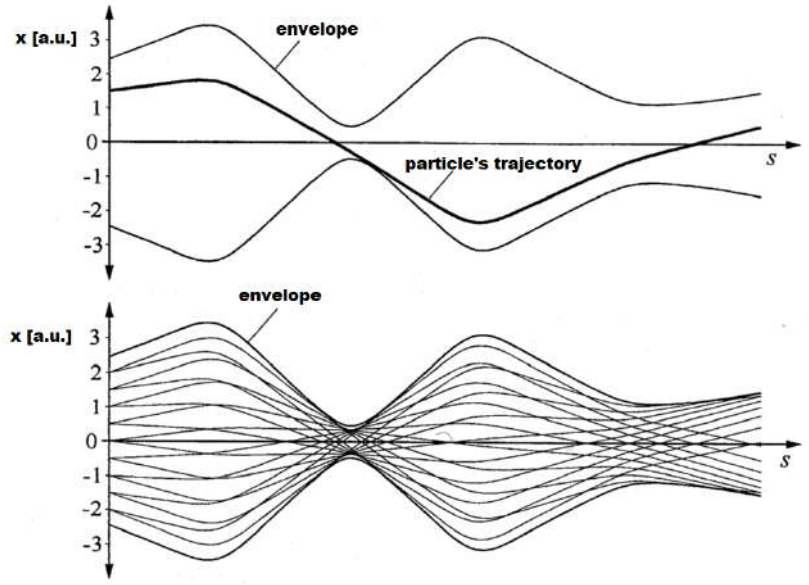

Figure 3.2: In the upper picture the trajectory of a single particle within the envelope $\sigma(s)$ is shown. The botton one presents trajectories for several particle in an electron beam and its envelope. Picture adapted from[2]

related by the transfer matrix in the following way:

$$\begin{pmatrix} x \\ x' \end{pmatrix} = \begin{pmatrix} C(s) & S(s) \\ C'(s) & S'(s) \end{pmatrix} \begin{pmatrix} x_0 \\ x'_0 \end{pmatrix}. \tag{3.31}$$

Since emittance is constant, using eq.3.17 and its derivative along whit eq.3.27 yields

$$\epsilon_{\mathrm{tr}} = \gamma x^2 + 2\alpha x x' + \beta x'^2 = \gamma_0 x_0^2 + 2\alpha_0 x_0 x'_0 + \beta_0 x'^2_0, \tag{3.32}$$

where 'rms' and the position dependency is omitted for brevity. Now, from eq. 3.31 we can get $\mathbf{x_0}$. Combining it with the above equation, we get the transfer matrix which transforms the initial optical parameters into the final one

$$\begin{pmatrix} \beta \\ \alpha \\ \gamma \end{pmatrix} = \begin{pmatrix} C^2 & -2CS & S^2 \\ -CC' & CS' + C'S & -SS' \\ C'^2 & -2C'S' & S'^2 \end{pmatrix} \begin{pmatrix} \beta_0 \\ \alpha_0 \\ \gamma_0 \end{pmatrix}. \tag{3.33}$$

Furthermore, if the initial and final Twiss parameters are known, using eq. 3.11 and 3.17, the particle trajectories can be calculated along the beamline [55, 2, 59]

$$\begin{pmatrix} C(s) & S(s) \\ C'(s) & S'(s) \end{pmatrix} = \begin{pmatrix} \sqrt{\frac{\beta}{\beta_0}}\big(\cos\psi + \alpha_0 \sin\psi\big) & \sqrt{\beta\beta_0}\sin\psi \\ \frac{\big(\alpha_0 - \alpha\big)\cos\psi - \big(1+\alpha_0\alpha\big)\sin\psi}{\sqrt{\beta\beta_0}} & \sqrt{\frac{\beta_0}{\beta}}\big(\cos\psi - \alpha\sin\psi\big) \end{pmatrix}, \tag{3.34}$$

where $\psi = \phi - \phi_0$ is the phase advance between the initial and final position.

3.1.5 Dispersion function

So far we describe an electron without relative momentum deviation, i.e. $\delta = 0$. Now, let consider a particle with $\delta \neq 0$. Hill's equation 3.10 will gain another term according to the eq. 3.8:

$$x''(s) + K(s)x = \frac{\delta}{R(s)}. \tag{3.35}$$

The general solution of this inhomogeneous differential equation is given by the combination of homogeneous $x(s)$ eq. 3.17 and particular $x_D(s)$ solution which is usually expressed as

$$x_D(s) = D(s)\delta, \tag{3.36}$$

where $D(s)$ is called *dispersion function* and satisfied the equation

$$D''(s) + K(s)D(s) = \frac{1}{R(s)} \tag{3.37}$$

with general solution:

$$D(s) = S(s)\int_{s_0}^{s} \frac{C(t)}{R(t)}dt - C(s)\int_{s_0}^{s} \frac{S(t)}{R(t)}dt. \tag{3.38}$$

Thus the general solution of eq. 3.35 in the matrix formalism is given by [59, 56]

$$\begin{pmatrix} x(s) \\ x'(s) \\ \delta \end{pmatrix} = \begin{pmatrix} C(s) & S(s) & D(s) \\ C'(s) & S'(s) & D'(s) \\ 0 & 0 & 1 \end{pmatrix} \begin{pmatrix} x_0 \\ x'_0 \\ \delta \end{pmatrix}. \tag{3.39}$$

As a consequence the beam envelope will be different from eq. 3.40 because now the rms beam size has two components:

$$\sigma(s) = \sqrt{\epsilon_{tr,rms}\beta(s) + D^2(s)\sigma_\delta^2}. \tag{3.40}$$

The first is related to the betatron oscillation as in eq. 3.40, and the second comes from the energy spread in the beam where σ_δ is the uncorrelated energy spread.

3.2 Momentum compaction factor

Due to the chromaticity, in a dispersive section, particles will each follow a different path. To first order, the change in path length can be related to the dispersion function by

$$\Delta s = \int_{s_0}^{s} \frac{D(t)}{R(t)}\delta dt = R_{56}\delta, \tag{3.41}$$

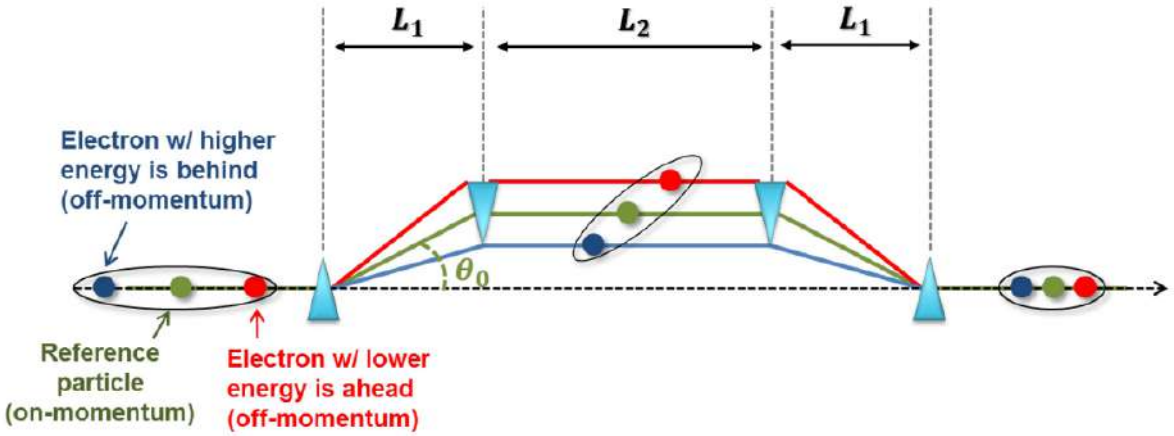

Figure 3.3: Magnetic chicane sketch adapted from [3]. Magnetic chicane consists of four magnets. An injected chirped electron bunch will exit the chicane compressed.

where R_{56} is often referred to as momentum compaction factor and it is related to the typical 6D phase space transfer matrix for only linear elements by [60]

$$\begin{pmatrix} x(s) \\ x'(s) \\ y(s) \\ y'(s) \\ z(s) \\ \delta \end{pmatrix} = \begin{pmatrix} R_{11} & R_{12} & 0 & 0 & 0 & R_{16} \\ R_{21} & R_{22} & 0 & 0 & 0 & R_{26} \\ 0 & 0 & R_{33} & R_{34} & 0 & 0 \\ 0 & 0 & R_{43} & R_{44} & 0 & 0 \\ R_{51} & R_{52} & 0 & 0 & 1 & R_{56} \\ 0 & 0 & 0 & 0 & 0 & 1 \end{pmatrix} \begin{pmatrix} x_0(s) \\ x'_0(s) \\ y_0(s) \\ y'_0(s) \\ z_0(s) \\ \delta \end{pmatrix} . \tag{3.42}$$

3.2.1 Magnetic chicane momentum compaction

In the last decades a growing demand for generation of very short electron bunches has pushed the community to develop new techniques achieving as short and high charge density as possible bunches. They have a wide range of applications which extend from dielectric structure driven by electron beam and plasma wake field accelerators to free-electron lasers.

One of the most used techniques for shortening an electron beam is the magnetic chicane. It is composed of four magnetic dipoles arranged as illustrated in Figure 3.3 to avoid a net deflection of the beam from the beam line axis. In a dipole with uniform vertical magnetic field B_0 a particle with a longitudinal momentum p_z will pass through the magnet bending its trajectory with a radius of curvature $R[m] \propto \frac{p_z[GeV/c]}{B_0[T]}$. Thus, particles with different momentum will follow different trajectories. To compress the bunch, an energy chirped beam, i.e. a linear correlation between the energy and the longitudinal position, needs to be injected into magnetic chicane. Usually the chirp is introduced accelerating the bunch off-crest before injecting the bunch into the chicane. A chirped beam will have higher energy tail with respect to head. In this way the time of flight of the tail will be shorter than the head leading to a bunch compression.

For a symmetric dipole arrangement, the relativistic reference particle passing through a dipole of length L_B is affected by the bending angle $\theta_0 = L_B/R = eB_0L_B/p_0$ and the total deflection angle through the whole chicane is zero. A particle with a momentum p_z will experience a

deflecting angle of

$$\theta = L_B/R = eB_0L_B/(p_0 + (p_z - p_0)) = \frac{\theta_0}{1+\delta}, \tag{3.43}$$

while the total deflecting angle is still zero. For a so-called achromatic chicane [3], particles which lie on a line and without divergence at the entrance of the chicane will stay on a line at the exit and the total bending angle for an off-momentum is zero regardless their energy spread. Under this ansatz the path length of a particle through the chicane can be easily calculated by geometrical considerations; it is four times the arc path inside the dipoles, once the straight distance between the upper dipoles and twice the path distance in the oblique section [61]

$$s = 4L_B\frac{\theta}{\sin\theta} + 2L_1\frac{1}{\cos\theta} + L_2, \tag{3.44}$$

where L_1 and L_2 are the distance between the dipoles as illustrated in Figure 3.3. When $\theta, \theta_0 \ll 1$, the difference of the path between the reference and the off-momentum particle is given by

$$\Delta s \approx -\theta_0^2\Big(L_1 + \frac{2}{3}L_B\Big)\Big(1 - \frac{1}{(1+\delta)^2}\Big) + \mathcal{O}(\theta^4) \approx -2\theta_0^2\Big(L_1 + \frac{2}{3}L_B\Big)\delta + \mathcal{O}(\theta^4, \delta^2), \tag{3.45}$$

where Taylor's expansion and relation eq. 3.43 have been taken into account. By comparison of the above equation and the eq. 3.41, the momentum compaction for a magnetic chicane to first order is

$$R_{56} \approx -2\theta_0^2\Big(L_1 + \frac{2}{3}L_B\Big). \tag{3.46}$$

Finally, keeping the linear approximation, one can derive the longitudinal slippage 3.41 for a particle inside of an electron beam with mean energy E_0 and energy spread $\delta = \delta_{\text{corr}} + \delta_{\text{unc}}$, where δ_{corr} is the correlated energy deviation from E_0 and δ_{unc} is the uncorrelated energy spread

$$ds_f = ds_i + R_{56}d\delta = dz_i(1 + h_iR_{56}) + R_{56}\delta_{unc}, \tag{3.47}$$

with $h_i = \frac{1}{E_0}d\delta_{corr}$ the initial linear energy chirp. Quantity $C = (1 + h_iR_{56})^{-1}$ is defined to be the linear compaction factor. The above equation gives a lower limit for the rms bunch length due to the non-zero uncorrelated energy spread $\sigma_{s,min} = R_{56}\sigma_{\delta_{\text{unc}}}$. Furthermore, assuming the convention that the chicane in Figure 3.3 provides a negative R_{56}, the bunch will be shortened if the chirp is positive, i.e. if the bunch tail has a higher energy than the bunch head.

3.3 Space charge

In the previous section the collective effects such as space charge and self-fields were neglected. A treatment of these effects is outside of the topic of this work. A complete description can be found in reference [62, 63].

As the beam travels in the accelerator, other sources of electromagnetic fields need to be considered. An important impact on the beam quality is played by the so-called self-fields [63], i.e. electromagnetic fields produced by the beam itself due to its beam current and charge distribution. The space charge field is one of these self-fields and it is caused by the interaction of the individual particles inside the beam with the collective charge distribution of the beam itself. These space charge fields are usually divided into a linear term which defocuses the beam,

leading to an increase in the transverse beam size, and the nonlinear term which also reduces the beam quality resulting in emittance growth.

Considering a beam with cylindrically symmetric charge distribution $\rho(r)$, the electromagnetic fields are expressed in cylindrical coordinates as [64, 65]

$$\begin{aligned} E_r(r) &= \tfrac{q}{\epsilon_0 r}\int_0^r \rho(r) r dr, \\ B_\theta(r) &= \tfrac{qv\mu_0}{r}\int_0^r \rho(r) r dr = \tfrac{\beta}{c} E_r, \end{aligned} \tag{3.48}$$

where ϵ_0 and μ_0 are the vacuum permittivity and permeability, respectively, related to each other by $c^2 = \frac{1}{\epsilon_0\mu_0}$ and $\beta = v/c$ is the normalized electron velocity. Using eq. 3.1 one gets the repulsive space charge forces

$$F_r = q(E_r + \beta c B_\theta) = qE_r(1-\beta^2) = \frac{q^2}{\epsilon_0 r \gamma^2}\int_0^r \rho(r) r dr, \tag{3.49}$$

where $\gamma^2 = 1/(1-\beta^2)$ is the Lorentz factor. The electric and magnetic field provides, thus, defocusing and focusing forces, respectively. Furthermore, the space charge (which is usually a repulsive effect due to the bigger intensity of the electric field w.r.t. the magnetic one) scales as $1/\gamma^2$ meaning that a high energy beam is less affected by space charge than a low energy beam. A trivial way to understand this effect is to consider two charges travelling in parallel. As the relativistic energy is achieved, the radial field lines of the charge become perpendicular to the direction of motion because of relativistic contraction. Thus, the electromagnetic forces between the two parallel charges vanish [63]. In other words, for relativistic energy the focusing magnetic field becomes significant and counteracts the defocusing electric field resulting in a mitigation of the space charge effect.

The space charge forces can be expanded around the orbit. The constant term affects the synchronous phase [63] while the linear term introduces a shift on the betatron oscillation and the nonlinear terms increase the emittance. To prove that let consider the paraxial beam envelope [66]

$$\sigma_r''(s) + \sigma_r'(s)\frac{\gamma'}{\beta^2\gamma} + K_r(s)\sigma_r(s) - \frac{k_s}{\sigma(s)\beta^3\gamma^3} - \frac{\epsilon_{n,tr}^2}{\sigma^3(s)\beta^2\gamma^2} = 0, \tag{3.50}$$

where the rms transverse beam size $\sigma_r(s)$ is evaluated for a beam under the effect of external focusing forces of strength K_r. The fourth term in the above equation represents the defocusing effect of the space charge which is proportional to the beam perveance $k_s = \frac{qI}{2\pi\epsilon_0 m_0 c^3}$ while the last one is the defocusing effect due to the emittance changing. In the so-called space charge dominated beam regime the effect of the emittance change is negligible[66, 63, 65]. An important parameter which determines the change from space-charge regime to emittance regime is the ratio between the emittance and space-charge term [67]

$$\rho = \Big(\frac{\beta\gamma\epsilon_{n,tr}^2}{k_s\sigma^2(s)}\Big). \tag{3.51}$$

This parameter changes from $\rho << 1$ to $\rho >> 1$ for a space charge dominated regime and emittance dominate regime, respectively.

3.4 Longitudinal beam dynamics

In this section the fundamental knowledge about the longitudinal dynamics will be presented. So far, in order to guide particles through the beam system, the interaction of a charged particle with the transverse components of electromagnetic field has been introduced. However, considering eq.3.4, a particle in an electromagnetic field will be accelerated if the electric field has one component in particle's propagation direction. It is clear that the free space electromagnetic plane wave doesn't have a longitudinal electric field component thus it is not possible achieve a net acceleration. A way to provide an accelerating field is to work into accelerating structures. Eq.3.4 reads

$$\Delta E_{\text{kin}} = e \int_0^z E_z dz. \tag{3.52}$$

In general, the longitudinal component of the phase-synchronous electric field is given by [16]

$$E_z = E_{0,z} \sin(\phi + \bar{\phi}(z, \gamma)), \tag{3.53}$$

which states that for an initial electric field amplitude $E_{0,z}$ the energy gain is dependent on the relative phase ϕ between the particle and the longitudinal electric field and the so called phase-slippage term $\bar{\phi}(z, \gamma)$. This term plays an important role in case of low energy beam where beam velocity is lower than electric field phase velocity leading to a change of the phase experienced by the particle.

A particle with a so-called synchronous phase ϕ_s in a travelling wave structure will experience the same phase along the accelerating structure. For a synchronous phase on the positive slope of the RF signal, one can consider another particle which arrives later in the cavity. This particle will experience a higher field intensity gaining more energy than the synchronous one. In case the particle arrives before in the cavity, it will gain a lower energy because it sees a smaller field amplitude [68, 69]. Introducing the phase relative to the synchronous particle as $\psi = \phi - \phi_s$, the

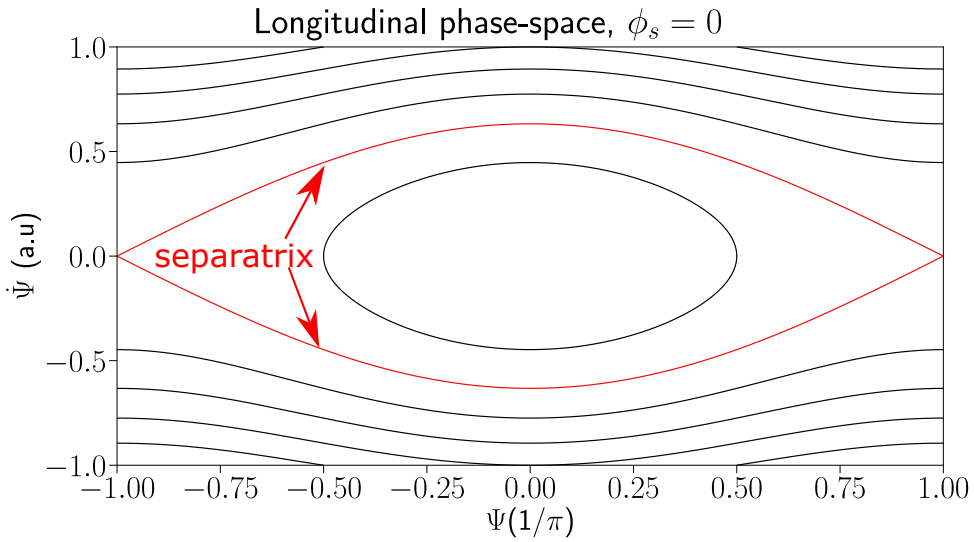

Figure 3.4: Longitudinal phase space for a synchronous phase at crossing section. Particles inside stationary bucket oscillate around the nominal phase.

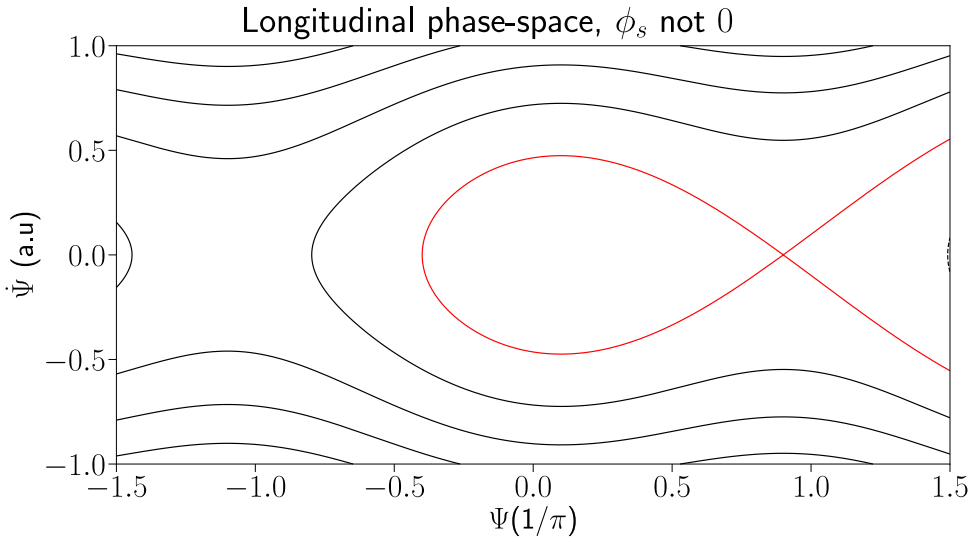

Figure 3.5: RF-backet fish shape for net energy gain. Red line defines the phase stable region around the synchronous phase $\phi_s \neq 0$.

equation of motion in the longitudinal phase space $(\phi, \dot{\phi}) \propto (z, \delta)$ is given by [55, 70, 71]

$$\ddot{\psi} + \frac{\Omega^2}{\cos\phi_s}\big[\sin\left(\phi_s + \psi\right) - \sin\phi_s\big] = 0, \tag{3.54}$$

where $\Omega_s^2 = \frac{eE_{RF}\omega_{RF}\cos\phi_s}{cE_0\beta_s^3\gamma_s^3}$ is the frequency of the longitudinal oscillations and shows that at relativistic energy the synchronous oscillation decreases drastically resulting into a negligible change of the particle distribution. Equation 3.54 is derived from the Hamiltonian

$$\frac{1}{2}\dot{\psi}^2 - \frac{\Omega^2}{\cos\phi_s}\big[\cos\left(\phi_s + \psi\right) - \cos\phi_s + \psi\sin\phi_s\big] = \mathcal{H}. \tag{3.55}$$

For a reference particle at zero-crossing, i.e. $\phi_s = 0$, no acceleration occurs and the particles around this phase may perform two different trajectories, as shown in Figure3.4. In one type they are limited in the closed curves performing oscillations around the nominal phase and ideal momentum; while in the second type, the particles are not limited in a specific area in the longitudinal phase space. The trajectory splitting the two states is called separatrix, just because it divides the stable and instable trajectory. While in the first case, particles oscillate about the synchronous phase, in the latter particles follow an unstable trajectory gaining or losing energy continuously. The area in the stable separatrix is referred to as bucket. In the particular case of $\phi_s = 0$ it is named stationary bucket and it is desired for example in a storage ring where bunched beams don't need to be accelerate.

As discussed for the transverse beam dynamics, also for the longitudinal phase space the Hamiltonian is a constant of motion for canonical variable (ψ, δ) considering the particle momentum instead of $\dot{\psi}$. Thus, the area occupied by the whole bunch in the longitudinal phase space is referred to as longitudinal emittance.

For a synchronous phase $\phi_s \neq 0$, the phase space diagram assumes the fish shape shown in Figure 3.5. Even if the stable phase is now reduced w.r.t. the stationary bucket, particles can

gain energy propagating in the RF cavity following eq 3.52.

4

Introduction to the waveguide mechanisms in hollow-core photonic crystal fibers

In this chapter, photonic crystal fibers will be introduced. The field equations for the modes used in the next sections of this thesis are reported and the fundamental waveguide mechanisms in photonic crystal fibers are also described. Finally, the stack-and-draw method for the fabrication of these fibers is illustrated.

4.1 Modes of a hollow core cylindrical waveguide

A metallic cylindrical waveguide supports two different type of modes: the transverse electric mode, TE modes, with only a magnetic field along the direction of propagation and without longitudinal electric field and the transverse magnetic TM modes without magnetic field in the direction of propagation z. It can be seen that these modes only propagates with a phase velocity above the speed of light making them not suitable for synchronous propagation with respect to the electron beam. Loading the waveguide with metallic irises [64] slows down the phase velocity whereas the reflected waves add an infinite number of spatial harmonic which produces non-linearity in the field. A way to overcome this problem is to load the waveguide with a dielectric layer; the dielectric lined waveguide (DLW) supports also the hybrid electromagnetic mode, HE-HM modes, with both longitudinal electric and magnetic fields and allows for matching between the modes phase velocity and the speed of light. The hybrid modes can be expressed as superimposition of transverse modes TE and TM components as shown in reference [72]. In this thesis the photonic crystal fiber (PCF) will be investigated not only as light guiding structure but mainly as electron beam energy manipulator. For an easier understanding of the modes in the PCFs it is instructive to investigate the fields and the propagation constant for a cylindrical hollow core (HC) waveguide. It should be note that for an optical frequency the metallic waveguide doesn't act as a good conductor anymore but rather as dielectric material with a larger dielectric constant [73]. In the following the basic steps to calculate modes and modal propagation constant are shown. The readers may take [73, 74, 72, 75, 76] as references for a more detailed analysis. Here we take in consideration an HC waveguide with core radius ρ and an

infinite cladding surrounding the core. The infinite cladding allows to neglect the reflected waves at the dielectric boundary. These reflected fields may destructively or constructively interfere with the fields in the core increasing or reducing the attenuation. However, if the free-space wavelength is much bigger than the core radius, the modes is low-loss because fields propagate mainly in the vacuum core. The fields need to satisfy Maxwell's equations (in SI units):

$$\begin{aligned} \nabla \cdot \vec{B} &= 0 \\ \nabla \cdot \vec{D} &= \rho \\ \nabla \times \vec{E} &= -\frac{\partial \vec{B}}{\partial t} \\ \nabla \times \vec{B} &= \frac{\partial \vec{D}}{\partial t} + \vec{J} \end{aligned} \tag{4.1}$$

where $\vec{E}$ and $\vec{H}$ are the electric and magnetic fields while $\vec{D}$ and $\vec{B}$ are the displacement and magnetic induction fields. Since the fiber consists of homogeneous dielectric material and in absence of internal source, the free charge density ρ and the current density$\vec{J}$ will be assumed zero. Furthermore, only linear effect will be take in consideration so that $\vec{E}$ and $\vec{H}$ are linearly related to $\vec{D}$ and $\vec{B}$ by:

$$\begin{aligned} \vec{D} &= \epsilon_0 \epsilon_r \vec{E} \\ \vec{B} &= \mu_0 \vec{H} \end{aligned}$$

where μ_0 is the vacuum magnetic permeability and ϵ_0 and ϵ_r are the vacuum and relative permittivity, respectively.

For symmetry reasons it is useful to introduce a cylindrical-coordinate system (r, θ, z). For the linearity of Maxwell's equations, the fields can be expressed by separation of time and space variables. It is common to assume a field pattern which varies harmonically with time:

$$\vec{\Pi}^{(e,m)} = \vec{\Pi}^{(e,m)}(r, \theta) e^{i(\omega t - \gamma z)} \tag{4.2}$$

where $\vec{\Pi}^{(e,m)}$ indicating the electric and magnetic field, ω being the angular frequency and γ the complex propagation constant which is defined as $\gamma = \alpha + i\ \beta$ where α and β are the attenuation constant and the phase constant, respectivelly. The above assumption is not restrictive because any periodic solution can be expressed as a combination of these sinusoidal modes by Fourier expansion. In order to derive the field components and get the dispersion characteristic, the wave equation has to be solved. For the longitudinal field component Ψ, it reads:

$$\left(\frac{\partial^2}{\partial r^2} + \frac{1}{r^2} \frac{\partial^2}{\partial \theta^2} + k_0^2 \nu^2(r, \theta) - \gamma^2 \right) \Psi = 0 \tag{4.3}$$

where $k_0 = \frac{2\pi}{\lambda}$ is the free-space wavenumber and $\nu = \sqrt{\frac{\epsilon_r}{\epsilon_0}}$ is the complex refractive index of the medium. The solution for the above equation is a combination of Bessel function. Obtained the longitudinal component, then Maxwell's equation will provide the other field components. Reference [75] shows in detail the calculation for the field components of a TM_{01} mode. From eq. 4.3, the longitudinal field component results on a series of Bessel function which is difficult to handle. For that reason, it is useful to introduce the following approximations:

$$\frac{\rho}{\lambda} \gg 1, \quad \left| \frac{k_z}{k_0} - 1 \right| \ll 1 \tag{4.4}$$

where ρ is the core radius of the waveguide and k_z is the axial propagation constant of the chosen mode . The above approximations require a core radius much larger than the free space wavelength λ and to restrict the analysis only to low-loss modes over which the propagation constant approximates the free space wavenumber, $\gamma \approx k_0$. Under these restrictions, an analytical form for the field components of TE_{nm}, TM_{nm} and HE_{nm} into core and into dielectric may be carried out, as detailed in ref.[73]. Here the subscript n and m are the azimuthal number describing the number of times the field changes sign in rotation from 0 to 2π and the radial number which is the number of field maxima in the radial direction from 0 to r. Among the supported modes, in this work we investigate the interaction of the accelerating mode TM_{01} and the hybrid mode HE_{11} with an high energy electron beam; the approximated electro-magnetic fields read [73, 77]:

$$TM_{01} = \begin{cases} E_r = ik_1k_zJ_1(k_1r)e^{i(\omega t-k_zz)} \\ E_z = k_1^2J_0(k_1r)e^{i(\omega t-k_zz)} \\ cB_\theta = ik_0k_1J_1(k_1r)e^{i(\omega t-k_zz)} \end{cases}$$

$$HE_{11} = \begin{cases} E_r = i\big(k_z^2\frac{J_2(k_1r)}{k_1^2} + \frac{1}{r}\frac{J_1(k_1r)}{k_1}\big)\cos(\theta)e^{i(\omega t-k_zz)} \\ E_\theta = i\big(k_0^2\frac{J_2(k_1r)}{k_1^2} - \frac{1}{r}\frac{J_1(k_1r)}{k_1}\big)\sin(\theta)e^{i(\omega t-k_zz)} \\ E_z = k_0\frac{J_1(k_1r)}{k_1}\cos(\theta)e^{i(\omega t-k_zz)} \\ cB_r = -ik_0k_z\frac{J_2(k_1r)}{k_1^2}\sin(\theta)e^{i(\omega t-k_zz)} \\ cB_\theta = ik_0k_z\frac{J_2(k_1r)}{k_1^2}\cos(\theta)e^{i(\omega t-k_zz)} \\ cB_z = -k_0\frac{J_1(k_1r)}{k_1}\sin(\theta)e^{i(\omega t-k_zz)} \end{cases} \tag{4.5}$$

where ω is the angular frequency, $k_0 = 2\pi/\lambda = \omega/c$ is the wavenumber in free space, $k_z = \omega/v_p$ is the wavenumber in the material, J_m is the Bessel function of the first kind, θ is the angular coordinate and $k_1 = \sqrt{k_0^2 - k_z^2}$. ARFs operating in vacuum support phase velocities beyond the speed of light ($v_{ph} > c$).

4.1.1 Complex propagation constant

The complex propagation constant γ can be calculated for each supported mode by solving the characteristic equation, as detailed in ref. [73, 74]. The phase constant (and thus the effective index of refraction n_{eff}) and the attenuation constant are calculated as the real and the imaginary

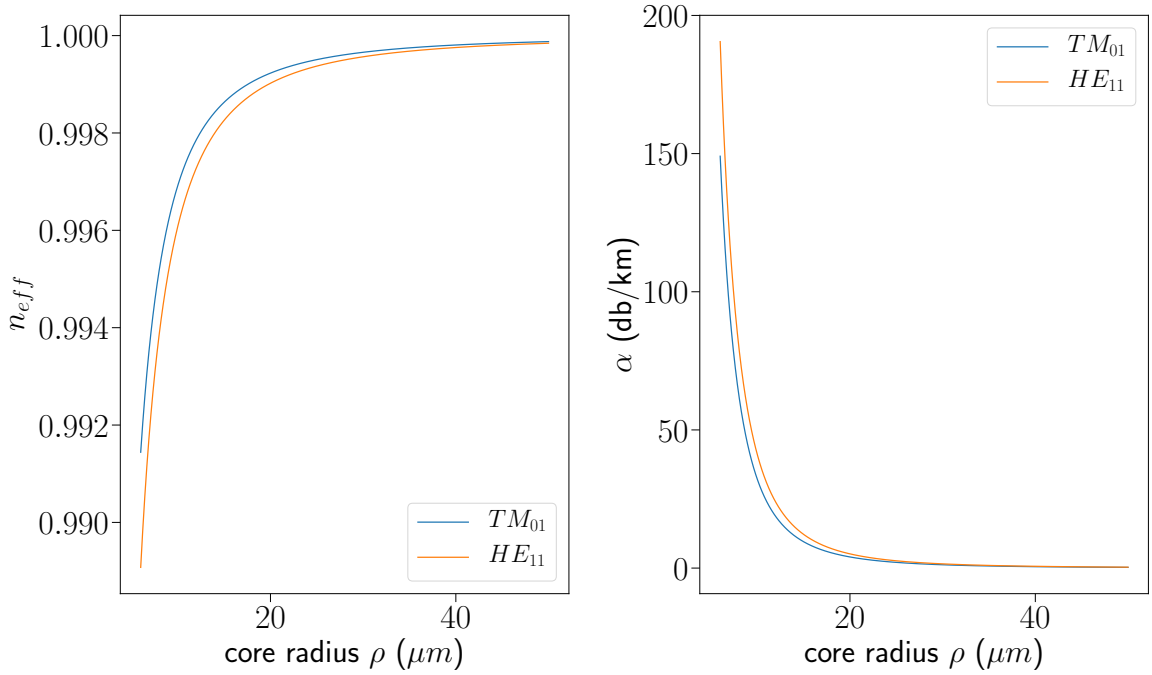

Figure 4.1: a) Effective refraction index and b)attenuation coefficient for the accelerating mode TM_{01} and the fundamental one HE_{11} fixing the wavelength at $\lambda = 2\mu m$

part of the complex propagation constant γ, reading:

$$n_{eff} = \frac{\lambda}{2\pi}\beta_{nm} = \sqrt{1 - \left(\frac{u_{nm}\lambda}{2\pi\rho}\right)^2}$$

$$\alpha_{nm} = \left(\frac{u_{nm}}{2\pi}\right)^2 \frac{\lambda^2}{\rho^3} \begin{cases} \frac{1}{\sqrt{\nu^2-1}} & TE_{0m} \\ \frac{\nu^2}{\sqrt{\nu^2-1}} & TM_{0m} \\ \frac{1/2(\nu^2+1)}{\sqrt{\nu^2-1}} & HE_{nm} \end{cases} \tag{4.6}$$

where u_{nm} are the m-th roots of the Bessel function of order $n-1$,i.e $J_{n-1}(u_{nm}) = 0$. As the core radius gets bigger w.r.t. the wavelength, the effective refraction index increases while the attenuation decreases. In other word, decreasing the ratio of wavelength and radius, the HC waveguides acts as a free space over which the phase velocity of the modes matches the speed of light without any losses. Figure4.1 (a)-(b) shows the n_{eff} and the attenuation α behavior for the TM_{01} and HE_{11} for a $\sim$2 µm wavelength while changing the core radius.

4.2 Photonic crystal fibers

The innovative idea to confine and propagate the light along an hollow-core microstructured fiber has been carried out by Philip Russell in 1991 [78]. The idea lies on concept that the light may be trapped inside the fiber by a 2D bandgap in the cladding. This phenomena is common in nature, for example it happens on the wings of a butterfly. The wings are wavelength-scale periodic structures over which incident light within a range of frequency and angle is reflected generating the color of the butterfly [79]. Based on the same principle, when a photonic crystal fiber (PCF) is properly designed it exhibits a bandgap preventing the escape of the light from the hollow core. However, due to the complexity to fabricate such a fiber, the first concept demonstration was based on a solid core fiber in 1996 [80]. This fiber, composed by a silica cladding hosting small air-holes arranged into a triangular lattice and solid core, allowed for the propagation of the fundamental mode in the core with very low losses. Only in the 1999 P.Russel and coworkers were able to demonstrate the PBG fiber guiding principle experimentally [6]. This generation of fibers are very robust since the waveguide mechanism remains even if the fiber is tightly bent. However, the geometrical parameters play an important role in the confinement of the light in the core and the waveguide mechanism is highly influenced by small fluctuations of these parameters.

4.2.1 Overview of different guiding mechanism in PCF

The PCF can be designed for supporting a wide range of light guiding mechanisms which are related on different fiber geometry. In the following, an overview of the most important mechanisms of light confinement is presented. The reader can take [79, 4, 81, 5] as references for a deeper treatments.

4.2.1.1 Modified total internal reflection

The most of the optical fibers used in telecommunication are related on the total internal reflection (TIR) mechanism. The core needs an higher refractive index n_∞ than the cladding n_c in order that the light confinement occurs. Based on Snell's law, if the light from the core hits the interface between the two regions with an angle bigger than the critical one, i.e. $\Theta > \arcsin(\frac{n_c}{n_\infty})$ then the light is confined in the core region. Larger the difference of refractive index, stronger the confinement. That is the reason because the core is usually doped but in a solid core PCF (also known as index-guiding PCF) the average refractive index of the cladding is smaller than the core. In fact the cladding is now filled by small air holes of diameter d (here the name modified total internal reflection), usually, arranged into a triangular lattice and spaced out by a fixed distance, the pitch Λ. Such a complex geometry prevents the exact solution of Maxwell's equation, thus numerical methods need to be used. Ref.[82] gives an overview of numerical solution methods such as Transfer Matrix method, Step Index Fiber analogy and plane wave method. The results are usually represented in the so called dispersion (or propagation) diagram whose axes are the normalized frequency $\omega\Lambda/c$ and the normalized wave vector along the fiber $\beta\Lambda$. A standard dispersion diagram for an step index fiber with Ge-doped core is showed in ref.[4, 5] and here adapted in Figure 4.2 a).

The dispersion diagram is an useful tools to figure out the range of frequencies and axial wavenumber k_z (also referred as propagation constant β) over which the light is evanescent, that means it does not propagate. As reported by Philipp Russell in his Science paper in 2003 [4], at

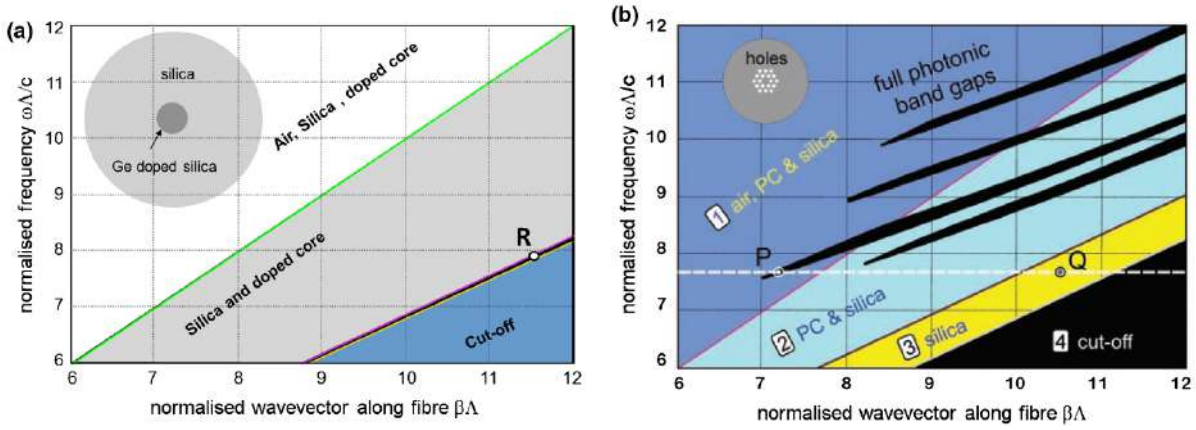

Figure 4.2: Dispersion diagram for a) step index fiber and b) photonic bandgap fiber. Adapted from [4] and [5].

fixed frequency the maximum value of β is set by $kn = \omega n/c$ for the material under consideration with refractive index n. These limits are represented by solid lines between two color regions in the dispersion diagram Figure4.2 a). For an axial wavevector $\beta < nk$ the light is able to propagate into the medium; while for a $\beta > nk$ the light is evanescent. In particular, taking in consideration Figure4.2 a), guided modes into the core appear on the red line (at points such as R). This narrow band set by $kn_c\Lambda < \beta\Lambda < kn_\infty\Lambda$ is representative of the region over which light is free to propagate into the core but evanescent into the cladding. In Figure4.2 b), the so called " finger plot" and the corresponding PCF area of light propagation are presented. In case of PCF, as aforementioned, the cladding is filled by air rods which reduce its effective index of refraction. For a fixed optical frequency, the light will be evanescent for axial wavevector in the region (4) while in region (1) it is free to propagate everywhere in the fiber. For β in region (2), light propagates into the photonic crystal cladding and silica core. Finally, a much bigger strip above the cut-off region is opened into the diagram: this region (3) corresponds to the axial wavelength over which light propagates only into the core and is evanescent in the cladding. The modes form in this area are called guiding mode. This area appears much bigger than the analogue one in the step-index fiber which points out why the PCF are so attractive also in the telecommunication. Furthermore, the dispersion diagram shows finger-shaped region (colored in black in Figure 4.2b)) in the cladding area referred to as bandgap over which for a given pitch and frequency propagating mode can't exist in the photonic cladding. It should be noted that the finger shape propagates into the air region (1) which means that air guidance is still possible. Thus, a mode with a frequency within the bandgap black finger will propagate into the core (whether solid or hollow) without leaking out into the cladding.

For the ratio $d/\Lambda \leq 0.4$, solid core PCF shows the peculiar characteristic to propagate as guided mode only the fundamental one at any wavelength [83, 4]. This endlessly single-mode operation can be easily understood (paraphrasing P.Russell) by viewing the cladding as a "modal sieve". Since light is evanescent in the air, the air-holes acts as a barrier ("the wire mesh of the sieve"). The "grain of rice" is the fundamental mode which has a single lobe of diameter $\lambda_{Rayleigh} \approx 2\Lambda$ [84]. Since the pitch Λ, i.e. the area between the wire mesh thought which the rice can pass, is too narrow the grain of rice can't escape. The size of the grain of rice for higher modes is smaller than the fundamental one, thus they can slip between the gaps and escape the core.

Even if this fiber is very attractive, it is clear that an application in electron beam energy

gain is useless as it can support only the fundamental hybrid mode HE_{11}. More promising for accelerator application are the next two generations of fibers which are going to be introduced in the following sections.

4.2.1.2 Hollow core photonic crystal fiber: band gap guidance

Hollow core photonic bandgap fiber (PBGF) usually consists into honeycomb or triangular cladding structure surrounding an air filled core (referred as defect). Since the central core is now formed by an air hole, the principle of modified TIR is not enable to be applied. In the case of 3D photonic crystal, one of the fundamental properties exhibited by the structure is the well-known Bragg gap. The periodic arrangement of scatters within the structure produces a destructive interference of the waves scattered by the incursions [85]. As a consequence, for some frequencies the structure may completely prohibit the propagation of light in all directions. This is referred to as bandgap. However, under appropriate geometries the propagation is only inhibited along certain directions (stop bands). One of these geometries is of course the fiber, which exhibits a 2D bandgap and allows the light to be confined within the fiber itself. To describe this phenomenon, the Block-Floquet theory is used, which refers to the physics of matter, where the periodic arrangement of atomic potentials generates electronic band gaps (forbidden energy bands for the electrons) [86]. In the case of PBG fibers, the bandgap is due to the periodic arrangement of dielectrics with different refractive indexes such as air and silica. Although Bloch's theory is referred to as the mathematically and quantitatively best model, other methods have been used in order to allow the qualitative analysis of realistic fibers with finite periodic cladding. In this second generation of alternative numerical techniques such as plane-wave expansion, finite element or finite difference methods take place. An exhaustive and mathematical explanation based on Bloch-Floquet theory is not in the purpose of this work but the readers can take [87, 81] as references for deeper treatments. However, for a phenomenological understanding of the light confinement into a PBGF, the coupled-wave approach can be adopted [87, 6]. The approach consists in to approximate the periodic cladding into a periodic dielectric gratings. As shown in Figure 4.3, when a wave is incident on the gratings, some diffracted waves raise up propagating into the cladding. Band gap occurs as result of multiple scattering and interference of the diffracted waves at each interfaces. At the end the incident wave can be seen as getting converted into these coupled waves which propagate into the channel core. Broadly speaking, the light at each air-silica interface will be transmitted and reflected; all these reflected waves, under correct geometrical parameters (ie. pitch and capillaries diameter comparable with the wavelength of the light), may interfere each other distructively raising a bandgap. If the core supports a mode located in the cladding bandgap it can't excape the core but is forced to propagate and stay confined in the core region. In few words, the core modes can't find any photonic states into the claddind for coupling to [82] and excape from the core.

4.2.1.2.1 Bandwidth

In HC-PBGF, the photonic bandgap (PBG) mechanism provides opportunities to obtain ultralow transmission loss and ultralow bending sensitivity [88]. At author knowledge, currently the lowest attenuation measured in a silica hollow core photonic bandgap fiber is of 1.72 dB/km at 1565 nm wavelength [89] with a bandwidth less than 40 nm. In the HC-PBF light is confined in the air core allowing for very low loss and high laser power propagation(it has been experimentally demonstrated the delivery of femtosecond pulse at mJ pulse energy [90]). Due to the attractive

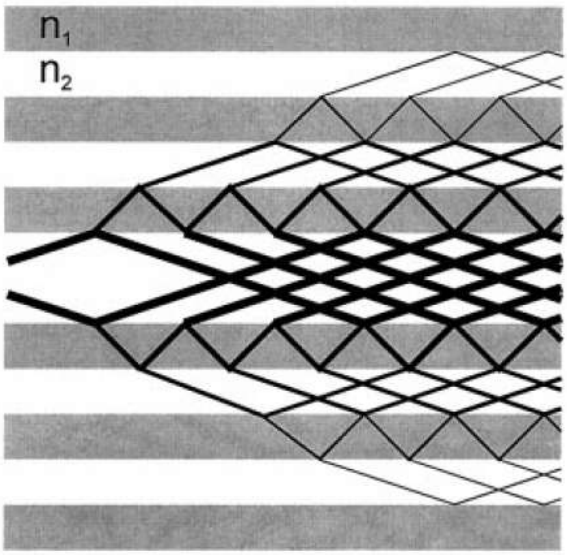

Figure 4.3: Photonic bandgap guidance mechanism. Adapted from [6].

applications for HC-PCF, scientific community has been worked on getting larger the bandwidth. Several simulation has been carried out showing that the triangular rather than the honeycomb lattice provides wider bandwidth.

Considerable effort has been put into understanding how geometric parameters such as core radius R, pitch Λ and capillaries diameter d affect fiber properties. A general finding is that the air-filling factor, defined as:

$$f = \left(\frac{\pi}{2\sqrt{3}}\right)\left(\frac{d}{\Lambda}\right)^2 \tag{4.7}$$

is one of the most important parameter to control the bandgap: increasing the air-filling factor the band gap becomes larger. Increasing the core radius the modal power in the glass will be reduced leading to a reduction in the total loss, while the number of air-guided modes is enhanced (since it scales as R^2) and a greater susceptibility to the mode perturbation due to the intermodal coupling. Furthermore, the intensity of the field and the effective index of refraction for the mode is also predicted to be reduced which corresponds to an higher phase velocity for the modes.

4.2.1.3 Antiresonant mechanism

In 2002 Benabid et.all [18] first demonstrated the possibility to confine and propagate light in a HC-PCF fiber over a broad transmission range. Considering a Kagomè geometry, which means capillaries arranged into a honeycomb web with a core defect, the optical transmission bands covers the visible and near-IR frequencies with relatively low-loss. Only few years later, it was found that the guiding mechanism of these fiber was different from the PBG confinement. In fact, simulations showed that forbidden gap didn't appear in the dispersion diagram [91]. Furthermore, it was noted that the properties of the Kagomè fiber could be qualitatively and quantitative explained taking in consideration easier fiber geometries w.r.t. the Kagomè structure such as concentric hexagons or circle around the core [92]. This was the propulsion for investigating into a new generation of fibers which sees the single-ring HC-PCF as one of the most studied

and promising geometry due to the combination of low loss, broad transmission bandwidth and reduced fabrication complexity.

At the date the guiding mechanism over which the HC-PCF is based on is not yet settle. There are two light guiding methods which are most favorite against the others: the inhibited coupling and the antiresonant mechanism. The first, which is introduced in ref.[93], suggests that the core and cladding modes do not overlap in space even for the same frequency and longitudinal wavevector. This is due to the fast phase oscillations of the cladding modes respect to the core modes. In this way the coupling between the cladding modes and the core modes is inhibited. On the other hand, antiresonant guiding is related to the core wall anti-crossings. Because this mechanism allows to understand and calculate important figure of merit for the modes propagation and confinement, it will be shortly introduced in the following.

The mostly studied geometry for antiresonant fiber is the revolver-type fiber geometry (ARF), also named as single-ring fiber, which consists of a thin glass capillaries (named as antiresonant elements, AREs) arranged in a circle at constant distance each others. The AREs are then fixed to the cladding which acts for mechanical stability and, unlike PBG fiber, it has only a small impact on the waveguiding [92]. The transmission spectrum shows windows of high-loss between two regions of high-transmission over which the antiresonant mechanism happens; these loss regions will be opened in the transmission spectrum for wavelengths described by equation [94, 95, 96, 97]:

$$\lambda_q = \frac{2t}{q}\sqrt{n_2^2 - n_1^2} \tag{4.8}$$

where t is the ARE thickness, q is an integer which defines the order of the resonance, n_2 and n_1 are the refractive indices of the ARE wall and the core, respectively. Unlike the PBG fiber, only the wall-thickness needs to be considered as geometrical parameter for light confinement which does not depend on the periodicity of the cladding; when eq.4.8 is satisfied the light can overcame the ARE wall resulting in a huge loss. The above equation comes from the antiresonant reflection optical waveguide (ARROW) mechanism, first introduced by Duguay [98] for a planar waveguide with cladding composed by an alternating of low and high refractive index materials, and adapted for a PBG fiber by Litchinitster [95]. In this model, each higher refractive index layer is regarded as a Fabry-Pérot (FP) etalon. When the light is launched into the FP resonator constructive interference will occur if the input light and the light circulating in the resonator are in phase resulting in resonant enhancement of the circulating light. On the other hand, if they are out of phase, the input light will be transmitted and only a small portion be stored inside etalon. Based on the same effect but the other way around, in an ARF the light will escape the core if it is in resonance and the cavity is transparent which is met for wavelength given by 4.8. The light will be strongly confined in the off-resonance state where the reflectivity of the FP resonator is higher. However the ARROW model is in good agreement with the experiments only until the launched light wavelength is much smaller than the fiber core diameter; for wavelengths satisfying $\frac{\lambda}{t} > 2\sqrt{n_2^2 - n_1^2}$ the electric field doesn't form a standing wave pattern inside the high-index layer ruled out the ARROW mechanism [95, 5]. In this case the spectrum is again strongly affected by the periodic lattice and by the number of the layer surrounding the core as in the PBG fiber.

Another important characteristic of ARF is the size of the core being several tens of micrometers which is larger w.r.t. the PBF or TIR fiber, enhancing the loss limit especially for the step-index fiber where the limit is set by the material breakdown. An analytic expression for the complex effective mode index in a single-ring ARF has been proposed by Zeisberger and

Schmidt in 2017 [99]. In their paper, approximating the ARF by single planar films the analytic expression for the real and imaginary part of the effective refractive index has been carried out. In this paper a detailed calculation of the complex effective mode index is showed and the fundamental results for the phase index $Re(n_{eff})$ and the loss coefficient α for the transverse and hybrid modes are given by [99]:

$$Re(n_{eff}) = n_a - \frac{j^2}{2k_0^2 n_a R^2} - \frac{j^2}{k_0^3 n_a^2 R^3}\frac{\cot\phi}{\sqrt{\epsilon-1}} \cdot \begin{cases} 1 & TE_{0m} \\ \epsilon & TM_{0m} \\ (\epsilon+1)/2 & HE_{nm} \end{cases} \tag{4.9}$$

$$\alpha = \frac{1+\cot^2\phi}{\epsilon-1}\frac{j^3}{k_0^3 n_a^3 R^4} \cdot \begin{cases} 1 & TE_{0m} \\ \epsilon^2 & TM_{0m} \\ (\epsilon^2+1)/2 & HE_{nm} \end{cases}$$

where n_a is the refractive index of the core, k_0 is the usual vacuum wave number, $(n.m)$ are the azimuthal and radial mode index, $\phi = t\sqrt{k_0^2(n_g^2 - n_a^2) + k^2}$ is the relative phase corrisponding to the phase acquired between two reflections inside the thin film of thickness t with k_g being the transverse wave number in the glass whereas k in the air, R is the core radius, $\epsilon = \frac{n_g^2}{n_a^2}$ and

$$j = \begin{cases} u_{1,m} & TE_{0m}/TM_{0m} \\ u_{n-1,m} & HE_{nm} \\ u_{n+1,m} & EH_{nm} \end{cases} \tag{4.10}$$

with u_{nm} the m-th root of the Bessel function $J_n()$.

It can be noted that while for a capillary (or dielectric lined waveguide) the loss of the fundamental mode is proportional to $1/R^3$, as shown in eq. 4.6, for ARFs operating at antiresonant frequency the loss scales as $1/R^4$. It has to be noted that the model proposed by Zeisberger provides a qualitative behavior of the transmitted spectrum but it doesn't reproduce the experimental results. Figure 4.4 shows the behavior of the transmitted spectrum of a TM_{01} mode inside an ARF employing eq.4.9. Recently L.Vincetti [100] proposed an analytical description of the confinement loss based on single tube mode. However, due to the complexity of the electromagnetic waves scattering inside the fiber, an analytical model is not able to reproduce the whole experimental results.

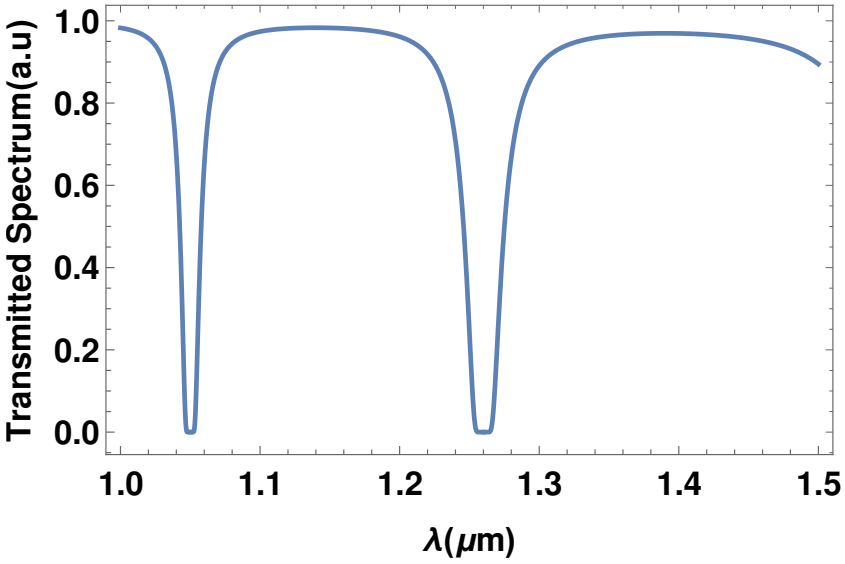

Figure 4.4: Example of transmitted spectrum for an ARF. At the resonance wavelengths, attenuation is enhanced and the calculated TM_{01} mode leaks through the surrounding layers. For antiresonance wavelengths, the mode is reflected by the high index layers and the attenuation is reduced.

4.3 Fabrication of photonic crystal fiber

A number of distinct methods of fabrication can be used to produce photonic crystal fibers which usually assume the preparation of a meter long preform with the desired crystal lattice pattern and then draw it into the required macroscopic scale while preserving the initial pattern. One of the most common techniques is the stack-and-draw method, first used by Knight et al.[80] in 1996 producing PBG fiber. This method, used at MPL in Erlangen, is rather fast, clean and low-cost allowing the fabrication of PCFs with very complex lattice pattern.

Figure4.5 shows the stack-and-draw procedure which can be divided in three fundamental steps and described as follow[7, 101]:

A) *Capillaries fabrication.* A greater effort needs to be given to the fabrication of the capillaries which are the basic building elements of a PCF. Their quality will affect the light propagation and attenuation in the final fiber. Generally, commercial silica tube is mounted on a drawing tower. By hot furnace at temperature between the softening and melting point ($\approx 2000C$ for the silica) and a tractor with controlled speed, the tube is drawn to outer diameter of few mm and 1 meter long. To control the size of the capillaries, an accurate chosen of pressurization, feed rate, tractor speed and furnace temperature needs to be observed.

B) *Stacking the preform.* The periodic cladding pattern is achieved by stacking the capillaries and rods properly. Dust residue and fiber bent may increase loss and reduce mechanical strength; this is why in a clean environment, the capillaries are first cut into shorter pieces and then arranged and stacked layer by layer in order to form the desired macroscopic structure named as preform stack.

D) *Drawing the cane.* Then the stacked capillaries are carefully inserted into a jacketing tube while a side of one end is closed air-tight by sealing. The cane is now ready to be drawn

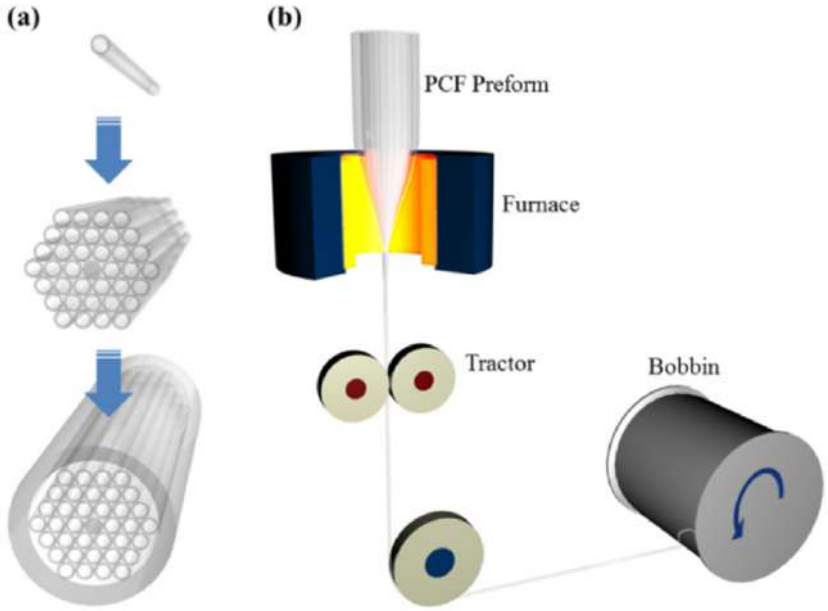

Figure 4.5: Stack-and-draw method [7]

to 1-2 mm diameter size by furnace and tractor. Applying vacuum between the capillaries and the jacket the interstitial holes can be closed.

D) *Drawing the PCF.* The final step is to draw the cane into fiber with the desired dimensions. The cane is mounted on the drawing tower, inserted into a glass tube and drawn down to the final fiber, always by tuning process parameters as well as the pressure applied inside the preform which can adjust the air-filling fraction. A final polymer coating is applied to the PCF for improving the mechanical strength.

4.3.1 Effects of bending on a fiber

Manufacturing is never a perfect process even if accurate diagnostic tools are applied during the fabrication process in order to control the geometrical parameters of the fiber by tuning the process parameters. Furthermore, into an experimental campaign the possibility of an unwanted fiber bending needs to be taken in consideration. Due to the bending the longitudinal symmetry is broken increasing the dimension of the problem. This is overcome introducing coordinate transformation which reduces computational time and bringing back the problem to 2-D simulations [102]. The basic idea is to introduce coordinates which allows to describe the bent fiber by a straight fiber but with a modified refractive index distribution $n'(x, y)$ which at first order is given by [103, 104]:

$$n'(x, y) = (1 + \frac{y}{R_{eff}})n(x, y) \tag{4.11}$$

where x and y are the transverse directions, while the fiber axis lies at y=0 and the y axis pointing out of the bend; $R_{eff} = 1.28R$ for silica fiber [103] is the effective curvature radius and R is the bent curvature and $n(x, y)$ is the refractive index of the straight fiber given by 4.6. Eq.4.11 shows that the bend introduces losses and can also reduce the effective mode area due to the shift of the center of the mode toward the outside of the bent [103]. Furthermore, for a bent radius

$R > R_{cr}$ ($\approx D^3/\lambda^2$ [104]) the core modes will match the capillary modes reducing drastically the light confinement which leaks away toward the capillaries. Nevertheless, the bending may decrease the real component of the effective refractive index slowing down the phase velocity of the modes. This could bring the electron beam to match to the phase velocity enhancing the interaction length.

4.3.1.1 Birefringence

Due to manufacturing imperfections PCFs can show birefringence property. The birefringence can be defined as the difference of the propagation constant between the x- and y-polarization of the field, $B = |n^x_{eff} - n^y_{eff}|$. In other words the refractive index of the optical material depends on the polarization of the electric field. Usually, ideal HC-PCFs are unaffected by birefringence due to the little interaction between the light and the silica cladding but under mechanical stress, i.e. bending the fiber [105], or introducing asymmetry in the periodic structure of the fiber, i.e deforming the circular core to elliptical shape[106] or changing the thickness of few AREs in the ARF, the refractive index can be field polarization-dependent. A lot of efforts have been pursued by scientific community to control the birefringence in HC fibers because of their application in high sensitivity sensor[107] and polarization-maintaining fiber [108]. Birefringence in PCF as accelerator can be deleterious for the electron beam quality because it may add more instability in the fields experienced by the bunch increasing i.e. its energy spread.

5

Tolerance studies and limitation for photonic bandgap fiber accelerators

Laser-driven hollow core photonic bandgap (PBG) fibers were proposed by Lin in 2001 as high-gradient accelerators [17]. The central defect in the transversely periodic lattice supports an accelerating mode for synchronous acceleration in the ultra-relativistic regime. The optical frequencies in such dielectric laser accelerators motivate a sensitivity and tolerance study to overcome manufacturing imperfections. Finally we discuss the propagation characteristics of Lin-fibers and find that small-bandwidth ($\sim$ ns) pulses would be needed for efficient acceleration over longer distances. These findings have been reported into IPAC manuscript [109].

5.1 Photonic bandgap fiber accelerators

Modern conventional particle accelerators operate with radiofrequency and use metallic resonant cavities providing acceleration gradient of up to $\sim 100\,\mathrm{MV/m}$.
Metallic breakdowns and power requirements, as well as the complicated infrastructures of modern accelerators has motivated the scientific community to look for new advanced concepts which could improve accelerating gradients on more compact footprints, i.e. with smaller wavelengths. By comparison, dielectric materials have a laser damage threshold one or two order of magnitude bigger than their metallic counterparts. For example, in the optical regime, fused silica has a breakdown threshold of $\sim$ GV/m, the small optical energies required to reach these gradients $\sim$ µJ are available at high repetition rates (MHz) from modern conventional laser manufacturers.
Structure-based laser driven accelerators (DLA) have been largely investigated and the first experimental demonstration of acceleration using a dielectric grating-structure was achieved [13, 14, 110]. Recently D.Cesar [15] demonstrated a 315 keV energy modulation on a 6.5 MeV beam using an optimized approach. However grating structures are side-coupled and therefore inherently have a very limited interaction time with the accelerating laser pulse. This has motivated alternative research into copropagating accelerating methods.

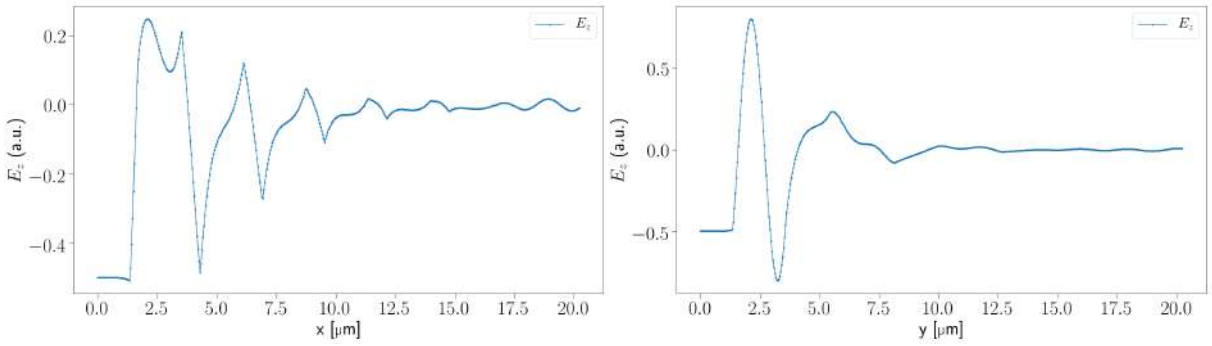

Figure 5.1: Longitudinal electric field propagation along transverse direction: in the fiber core section the field is uniform in both a)x- and b) y-direction of propagation.

5.1.1 Speed of light accelerating mode supported by PBGF driven by 2μm laser

Philip Russell demonstrated the first silica-air photonic crystal fiber (PCF) in 1995 [80, 4]. The PCF consists of a hollow core surrounded by air capillaries which support a photonic bandgap (PBG) preventing the escape of light from the hollow core (defect) via a Bragg-like confinement, as discussed in the previous chapter. The innovative idea to use the PCF as an accelerator was carried out by X. E. Lin [17] who proposed to use the defect for both mode confinement and acceleration channel. In his paper he showed that a PBG fiber (Figure 5.2) driven by a 1 µm laser and with specific geometrical parameters can support a radially uniform speed of light TM_{01}-like mode achieving an accelerating gradient up to $E_0 = 0.38\,\mathrm{GV/m}$. In his theoretical study, E.Lin proposed a fiber supporting a speed of light (SOL) surface TM-like mode properly confined into the defect by imposing the ratio of core size R and the pitch d (lattice spacing) to be 0.52. Under this imposition the accelerating mode is located into the bandgap and crosses the speed of light line about $k_0 d/2\pi \approx 1.3$ as shown in Figure 5.2 c). In this thesis, Lin-fiber geometrical parameters has been adapted to support a SOL accelerating mode when it is driven by a 2 µm laser. The air capillaries surrounding the defect are still placed into triangular periodicity while the geometrical parameters sizes have been re-adapted confining the TM_{01}-like mode. Table 5.1 summarizes the simulated parameters. Figure5.1 shows the longitudinal electric field along the x- and y- direction. It is important to note that in the fiber core region E_z is radially uniform. This effect comes from the speed of light condition. Being $v_{ph} = c \iff k_z = k_0$, Maxwell's equation for the longitudinal electric field component reduces to

$$\nabla_\perp^2 E_z(r) = (k_0^2 - k_z^2) E_z(r) = 0 \tag{5.1}$$

which leads to the radially uniform behavior for the longitudinal electric field component. This mode is usually referred as surface mode since the Poynting flux is localize at the boundary surface between the air core and the dielectric cladding. It should be noted that PBG fiber used in telecommunication are manufactured to support the so-called core mode where the Poynting flux is contained entirely into the defect. While the surface mode can cross the SOL line, the phase velocity supported by the core modes always exceeds the speed of light. In conclusion, for synchronous acceleration we need to consider only surface mode. Noble in [111] uses the formula

derived by Digonnet to calculate the number of core modes supported by the fiber

$$N_c \approx (k_0 d)^2 \Big(\frac{R}{a}\Big)^2 \frac{\Delta k}{k_0} \tag{5.2}$$

where Δk is the bandgap width above the SOL line. For Lin-fiber eq.5.2 gives that such a fiber can't support core mode. Last but not least, the reader should have noted that the accelerating mode has been called TM-like mode. This nomenclature is due to the fact that all the field components show the sixfold symmetry of the lattice ((see Figure 5.2 b) for example) while a standard TM mode doesn't exhibit a such azimuthal coordinate dependency. Furthermore, the region of higher longitudinal electric field is outside the defect. In order to estimate the maximum accelerating gradient G_0 for a such structure, we can introduce the ratio DF between the peak field outside the core and the longitudinal electric field. From Figure 5.1 DF is about 1.5. Defining G_0 as the ratio between the damage threshold of the dielectric E_{th} and DF, the maximum accelerating gradient is defined by [112]

$$G_0 = \frac{E_{th}}{DF}. \tag{5.3}$$

For the simulated fiber, the supported gradient is about 3 GV/m. The damage threshold of 5 GV/m has been used for the calculation since for a driven laser with 1 ps pulse duration at 2 µm wavelength the damage fluence is approximately $2\,\mathrm{J/cm^2}$.

Synchronous acceleration between the phase velocity of an accelerating mode and velocity of an electron bunch is critical to efficient acceleration – especially in the optical regime. In the following, we investigate the geometrical properties of a PBG fiber. We investigate how the various fiber parameters affect the phase velocity of the accelerating mode. Our simulations are performed using CUDOS MOF, MPB and MEEP. The former is a free code based on the multipole method which uses Fourier-Bessel expansion [49, 51, 52]; the second one is a frequency-domain eigensolver which computes definite-frequency eigenstates in periodic dielectric structures for arbitrary wavevectors [113]; while the latter one is a finite-difference time-domain (FDTD) method for computational electrodynamics [114]. The high-frequency driving fields and scale of the accelerating structures suggests challenging tolerance requirements and motivates a rigorous investigation.

5.2 Tolerance studies

A 2D PBG has a periodic structure in the two transverse directions acting as mode confinement and is uniform in the longitudinal direction. Due to the multiple scattering of the electromagnetic waves which occur at each vacuum-dielectric interface, a forbidden energy gap (bandgap) can appear in the dispersion diagram. Figure 5.2 shows the band diagram of a Lin-fiber obtained from MPB simulations for the geometrical parameters detailed in Table 5.1. The simulated geometrical parameters have been re-adapted for a 2 µm laser-driven PBG taking in consideration the ratio R/d=0.52 and $k_0 d/2\pi \approx 1.3$. Under these impositions which has been proposed by E. Lin, the fiber can support SOL accelerating mode.

A deeper understanding of a PBG is based on the Floquet-Bloch's theorem and the variational principle [81, 115, 116]. The bandgap width is primarily due to the contrast between the permittivities of the dielectric and vacuum-capillaries in 1D. However, in 2D, the bandgap width is

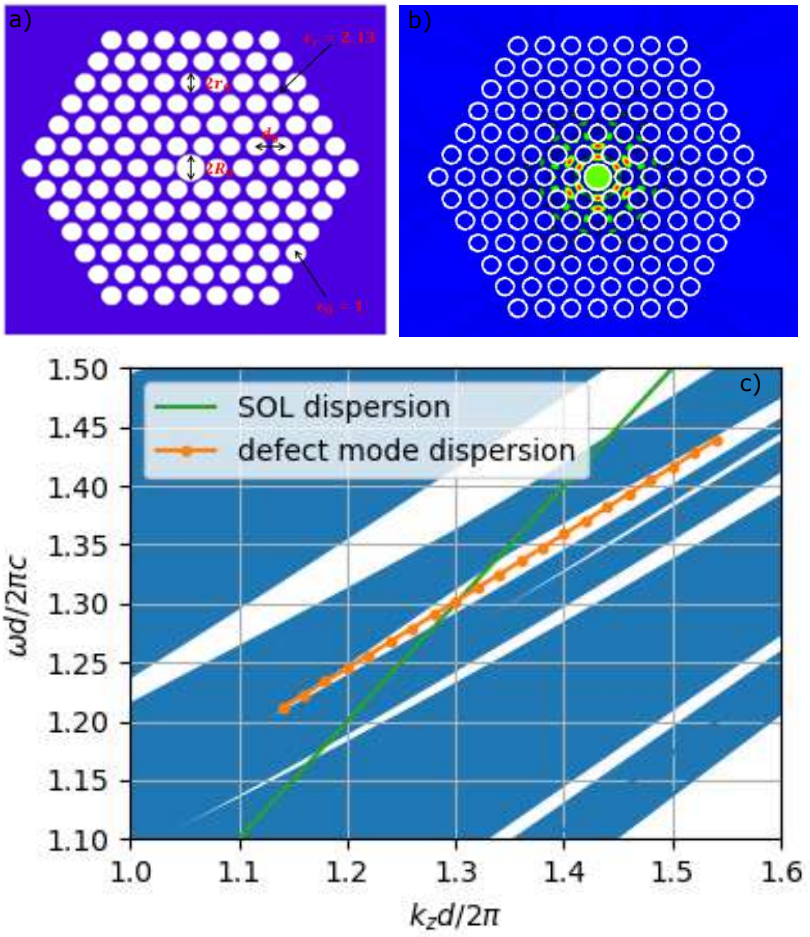

Figure 5.2: a) Lin photonic bandgap fiber: The accelerating mode, confined by the periodic lattice, propagates in the defect channel. b) CUDOS longitudinal field intensity of the defect mode (color scheme from blue (min) to red (max)). c) Dispersion diagram: the white regions are the bandgap structure of a Lin fiber in a frequency-wavenumber plane. The correct geometrical parameters introduce a defect mode (orange line) that cross the light line (green) in the bandgap.

Table 5.1: Geometrical parameters of the Lin fiber using a 2 µm laser

Lin's fiber Parameter	
Defect radius (R_0) [μm]	1.3572
Capillaries radius (r_0) [μm]	0.9135
Pitch (d_0) [μm]	2.61
Dielectric permittivity (ϵ_r)	2.13
Effective refractive index (n_R^0)	1.00369

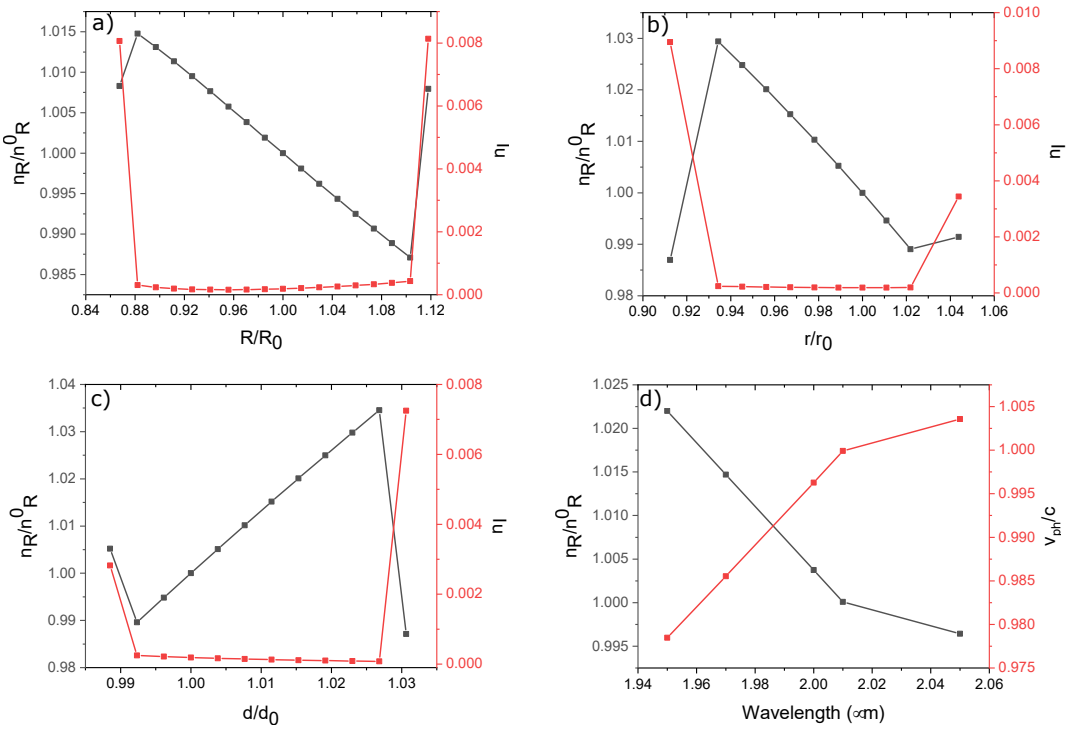

Figure 5.3: a)-c) Real and imaginary components of the effective refractive index as function of the geometrical parameters: the linear correlation results in a tolerance range of 10% in which the fiber supports an accelerating mode. The behavior outside the linear trend indicates that the higher modes have been excited in the core leading to an increase of the imaginary part of the effective refractive index and therefore to the loss (red). d) Real part of the defect mode's effective refractive index and phase velocity as function of wavelength.

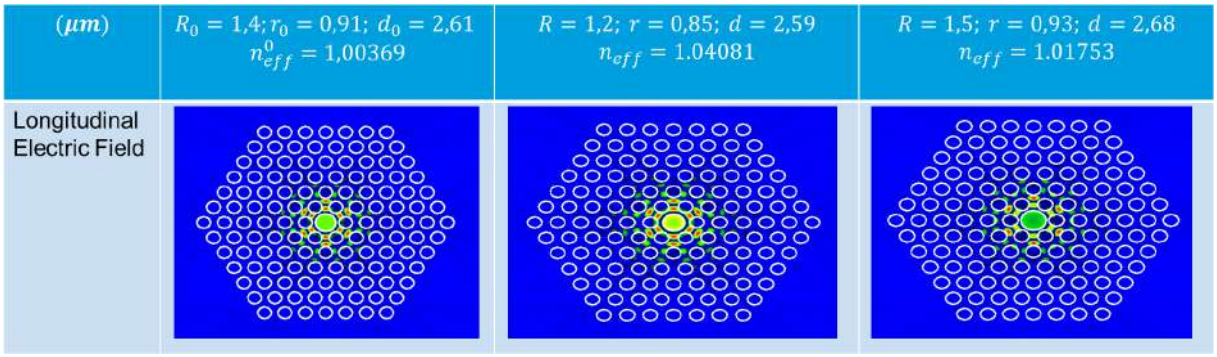

Figure 5.4: Effect of manufacturing imperfection on the longitudinal electric field distribution and on the effective index of refraction. On the left, the longitudinal electic field employing the parameters of 5.1. In the other figures, a casual change of the parameters leads to a curvature of longitudinal electric field into the core and to a change of the effective index of refration.

determined by a combination of the permittivity contrast and geometrical parameters which can tune the effective refractive index for the mode $n_{\text{eff}} = n_R + i\ n_I$ where i is the imaginary unit. The real component describes the phase velocity v_{ph} of the mode

$$n_R = c/v_{\text{ph}} \tag{5.4}$$

where c is the speed of light, while the imaginary part represents the diffractive loss due to Poynting flux escaping in the transverse direction:

$$n_I = \alpha/2k_z \tag{5.5}$$

where α is the loss coefficient and k_z is the propagation constant in the material [111].

Another important figure of merit is the Q-factor for the mode which is linked to its bandwidth:

$$Q = f_r/\Delta f \tag{5.6}$$

where f_r is the resonant frequency and Δf is the mode's bandwidth.

To accelerate particles efficiently, the phase velocity v_{ph} of the confined TM-like mode must match the electron velocity v_e. In the ultra-relativistic regime $v_e \sim c$ and for synchronous mode, where $v_{\text{ph}} \sim c$, the longitudinal accelerating fields in core become transversely uniform. If the geometric parameters (e.g. defect radius, capillary radii and pitch) change then the mode will shift in the dispersion diagram, yielding a new v_{ph}, (Eq. 5.4).

Figure5.3 (a-c) show the n_{eff} behavior scanning each parameter independently. To study the change in n_{eff} we have used CUDOS and within the range where it shows a linear relation to the defect radius we find that $d(n_R/n_R^0)/d(R/R_0) = -0.13$ in agreement with the literature [111]. The linear trend is also present as we modify the underlying crystal. By scanning the capillaries radius and pitch we find $d(n_R/n_R^0)/d(r/r_0) = -0.47$ and $d(n_R/n_R^0)/d(d/d_0) = 1.3$, respectively. Figure 5.4 shows how the manufacturing imperfections act on the n_{eff} and thus on the longitudinal electric field distribution. We note that the mode dispersion line is strongly dependent on the capillary radii and the pitch rather than the defect radius. Finally, a rough trend of n_{eff} as function of the input laser wavelength has been presented in Figure 5.3(d). The

possibility to shift the phase velocity of the mode tuning the wavelength may be an useful tool to select the right n_{eff} to accommodate manufacturing imperfections.

5.3 Quality factor

In the n_R linear range of Figure 5.3, the fiber supports an accelerating mode of which n_I is about $2\text{x}10^{-4}$ which corresponds to a very large loss coefficient α (see Eq. 5.5).

Figure 5.5 shows that the confinement could be improved as we increase the number of surrounding layers. The exponential decay behavior of the loss coefficient leads to an improvement of the Poynting flux confinement and thus could increase the length of the fiber (neglecting the phase slippage):

$$S_z \approx e^{-\alpha z}. \tag{5.7}$$

There is a tradeoff between the loss coefficient and quality factor. It is crucial to note that as the number of layers increases, the loss factor becomes exponentially better (Figure 5.5); however, with additional layers, the mode bandwidth also decreases exponentially. This implies that a efficient acceleration in a Lin fiber is incompatible with short, high bandwidth laser pulses.

From Figure 5.5, for a loss factor of α=1/m, we would require ~12 layers, suggesting an associated quality factor of 300,000. This corresponds in turn to a transform limited pulse duration of 880 ps for a Gaussian pulse. From [8], we estimate a fluence threshold of ~40 J/cm^2. We are assuming negligible variation of the damage fluence F from 1 µm to 2 µm. On a bulk fused silica, the damage fluence threshold of 1 µm is 17 J/cm^2. The peak electric field is given by [17]

$$E_{\text{th}} = \sqrt{\frac{2F}{\sqrt{\epsilon_r}\tau} Z_0}, \tag{5.8}$$

where ϵ_r is the fused silica permittivity, τ is the pulse length and $Z_0 = 377\Omega$ is the vacuum impedance. From the above equation a peak electric field of about 1.5 GV/m can be calculated. As discussed in the first section of this chapter, the ratio between the peak field outside the core and the longitudinal electric field is 1.5, leading to a maximum acceleration gradient in the core of ~1 GV/m. For a pulse length of 880 ps, due to the pulse phase slippage between the relativistic electron beam and the laser pulse, the maximum fiber length is 0.5 m calculated by

$$l = \frac{\tau c}{(1 - v_g/c)}, \tag{5.9}$$

where v_g is the group velocity evaluated as $\frac{v_g}{c} = 1/\epsilon_r$ for synchronous propagation [17].

The SINBAD facility at DESY [22] will begin research on DLA after commissioning is complete. The 2 µm laser system employed for these experiments has a transform limited pulse duration of 1.25 ps, which corresponds to 350 GHz of bandwidth. To gain some insights with the compatibility of a Lin fiber, eq. 5.6 yields a Q-factor of ~450 which corresponds to an $\alpha \sim 1100\,\text{m}^{-}1$ for 6 layers. Taking into consideration Eq. 5.7, 70% of the incoupled power will be lost into the matrix along a 1 mm long structure.

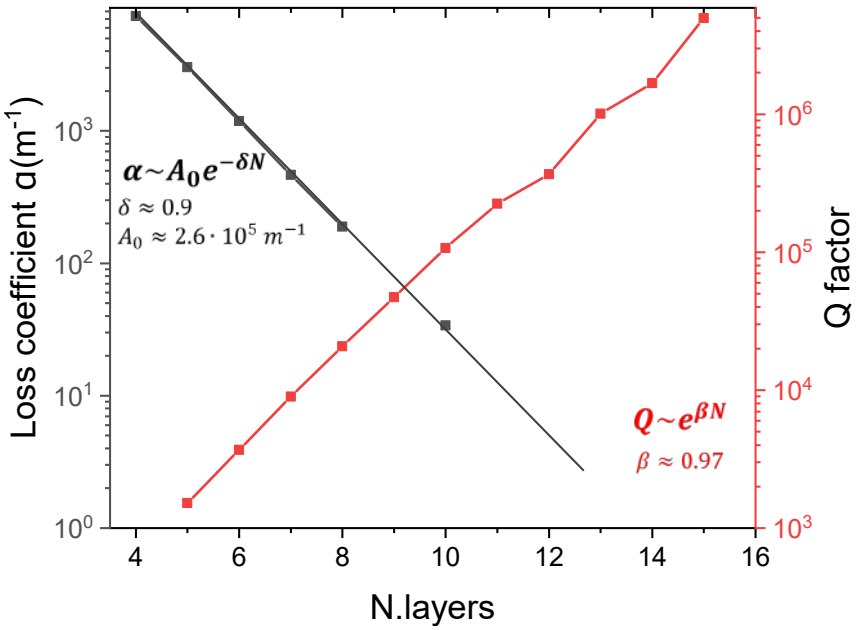

Figure 5.5: Loss coefficient and Q-factor as function of number of layers in a log scale plot.

5.4 Propagation of the accelerating mode

Finally, we present results for an in-coupling simulation using FDTD software, VSIM [117].

An effort for the coupling study was pursued by SLAC [112, 118]. In their theoretical papers, they show that from the far-field pattern is possible to obtaine the free-space mode profile which can be used to produce optimal coupling to the accelerating mode if propagated in reverse into the fiber. Their simulations show that a "6 petals" radially polarized gaussian beam resembes the required far-field pattern. It can be shown that a TEM_{03} Laguerre-Gaussian laser mode resembles the "6 petals" far-field pattern. Figure5.6 a) shows TEM_{03} (LG) given by [119]

$$LG_{pl}(r,\phi,z) = \frac{C}{\sqrt{1+(z/z_R)^2}}\left[\frac{r\sqrt{2}}{\omega(z)}\right]^{|l|} L_p^{|l|}\left[\frac{2r^2}{\omega(z)^2}\right] e^{-\frac{r^2}{\omega(z)^2}} \cdot \\ \cdot e^{\frac{-ikr^2 z}{2(z^2+z_R^2)}} e^{-il\phi} e^{-i(2p+|l|+1)\arctan(\frac{z}{z_R})} \tag{5.10}$$

where (r,ϕ,z) are the cylindrical coordinates system, $p \geq 0$ and l are the radial and azimuthal index, z_R is the Rayleigh length, $\omega(z)$ is the beam size, L_p^l is the associated Laguerre polynomial and C is a constant. Naidoo [120] demonstrated experimentally that 6 petals modes are a coherent superposition of $\mathrm{LG}_{0\pm3}$ modes generated by SLM (spatial light modulator). Coupling efficicency is predicted to be about 20% [118].

Here, we launch a radially polarized gaussian mode and focus it at the entrance of the fiber. The input field has a central wavelength of 2 µm and it has been simulated as the superimposition of the Hemite-Gaussian HG_{01} and HG_{10} modes. Figure 5.6 b) shows the calculated modes by

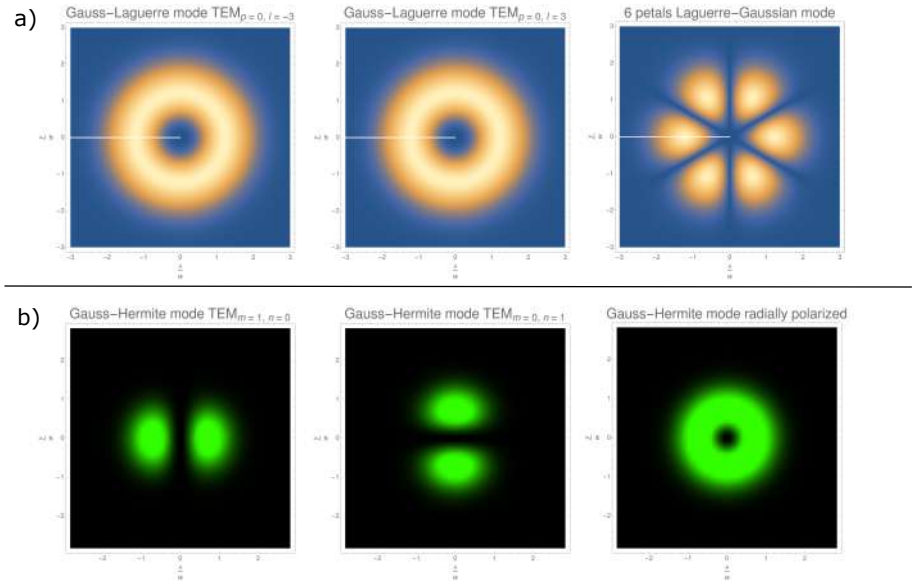

Figure 5.6: a) 6 petals radially polarized gaussian beam and b) Hermite-Gaussian radially polarized beam. The first is given by the superimposition of $LG_{0\pm3}$; the latter is a combination of the modes HG_{10} and HG_{01}.

the formula [121]

$$HG_{nm}(x,y,z) = \sqrt{\frac{1}{2^{n+m-1}\pi n!m!}}\frac{1}{\omega(z)}H_n\big(\sqrt{2}\frac{x}{\omega(z)}\big)e^{-\frac{x^2}{\omega(z)^2}}H_m\big(\sqrt{2}\frac{y}{\omega(z)}\big)e^{-\frac{y^2}{\omega(z)^2}}\cdot \\ \cdot exp\Big(-i\Big[kz-(1+n+m)\arctan(\frac{z}{z_R})+\frac{k(x^2+y^2)}{2R(z)}\Big]\Big), \tag{5.11}$$

with HG_{10} and HG_{01} are x- and y- polarized, respectively. In eq. 5.11, n and m are the nodes in the horizontal and vertical direction, respectively, $H_{n,m}$ is the Hermite polynomial and $R(z) = z\big(1+(z_R/z)^2\big)$ is the radius of curvature of the wavefront.

The results, shown in Figure 5.7, show the mode pattern along 50 μm of propagation. It is interesting to see that at 5 μm far from the end side of the fiber, the field profile resemble quite close the projection of Poynting flux obtained in [112] for 5λ distance from the PBF/vacuum surface.

Due to the time-consuming need for the calculation of the field pattern over longer distances, our simulations are based on 40 μm as fiber length. The incoupled mode is very lossy due to the small number of layers around the core which leads to big loss coefficient as demonstrated previously. The initially longitudinally polarized excitation pulse adapts into the PBG accelerating mode but due to the topological differences of the modes, a significant amount of energy is lost, see Figure 5.8.

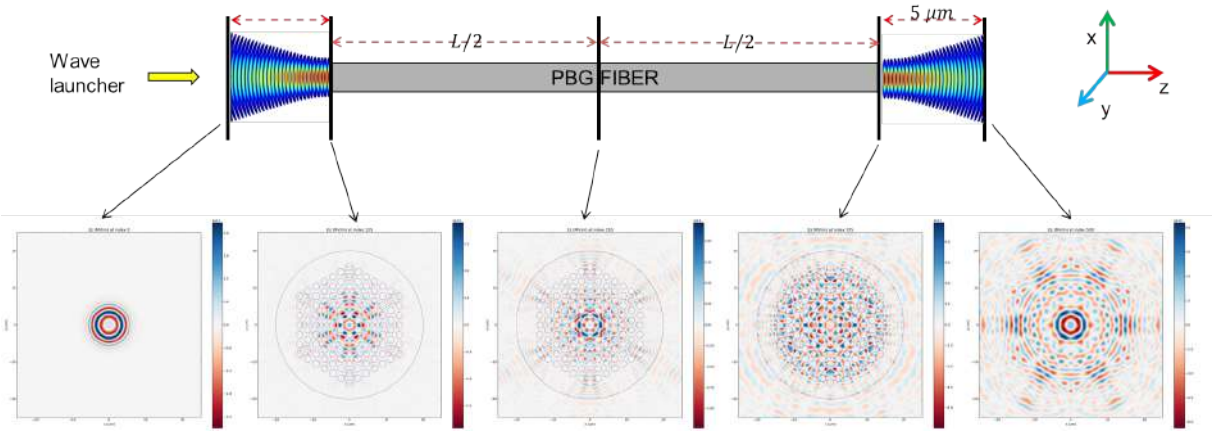

Figure 5.7: Sketch of the PBGF with incoupled mode at different position in the fiber.

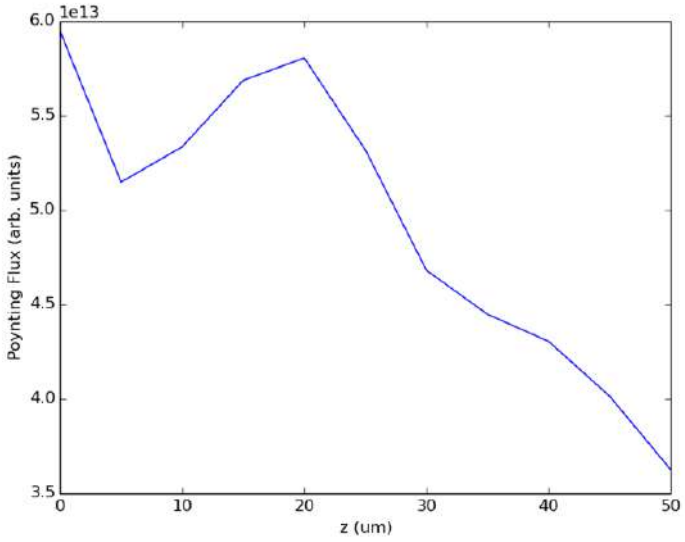

Figure 5.8: Poynting flux along the structure.

5.5 Conclusions

In this chapter, we have presented a tolerance study assuming realistic manufacturing imperfections and showing that the geometrical PBG fiber properties play a crucial role for getting and confining the optimal accelerating mode into the defect. Moreover, the defining a tolerance range in which the mode properties in the fiber can be recovered tuning the laser wavelength seems to be very useful for the manufacturing, where a tolerance range of 10% is generally required. Finally, we have pointed out that a strong limitation of a Lin fiber is the tradeoff between the loss coefficient and allowed bandwidth of the accelerating mode. An investigation into the compatibility of Lin fibers with narrowband $\sim$ ns pulses could be very interesting; however, we have shown that efficient acceleration using short, high bandwidth pulses in Lin-fibers is incompatible.

6

Electron beam manipulation with laser-driven anti-resonant fiber

The small aperture of the photonic bandgap fiber comparable with the driven wavelength makes both fiber fabrication and electron beam parameters challenging. Due to its bigger aperture, the anti-resonant fiber (ARF) could be an interesting candidate for beam acceleration and beam manipulation. Furthermore, under anti-resonant conditions, ARF allows for guiding light in broad range of frequency. In this chapter, we present the numerical ASTRA simulation results about the interaction of an electron beam with both accelerating mode TM_{01} and dipole mode HE_{11} inside the ARF. We propose a novel scheme using laser-driven anti-resonant optical fibers and show several appealing cases consisting of single-bunch acceleration, energy modulation, the production of microbunches and beam streaking. The findings of this chapter will be reported in "Attosecond bunch trains and sub-attosecond temporal resolutions with laser-driven anti-resonant fibers" manuscript. Submission of the paper on PRX is ongoing [122].

6.1 ARF design

The large core sizes of ARFs compared to grating DLAs potentially enable their application with conventional charged particle beams with micron-level emittances. Here we investigate the application of the two most elementary modes, the HE_{11}, which is primarily used in deflecting/streaking cavities and the TM_{01}, which is used for beam acceleration.

In order to meet the needed conditions for the use of an ARF in the field of accelerators and at the same time to respect the anti-resonance conditions an intensive collaboration was undertaken with the Max Planck Institute in Erlangen, in particular with P. Russell's division. Intense discussions were held in order to simultaneously satisfy the demands of a large hollow core, intense accelerating electric field, phase velocity of the interested mode as close as possible to the speed of light, and anti-resonance conditions for a wavelength of 2 µm, resulting in the fiber design shown in Figure 6.1. Here, ten capillaries are attached to the fiber cladding allowing for the propagation of a largely broadband spectrum in the central core about the reference wavelength of 2.051 μm. The theoretical transmission band is about [1550-2650] nm. Table 6.1 reports the most important geometrical parameters.

Since the ratio $\frac{d}{D} \approx 0.127$ the fiber can support and confine several modes being an multi-modes fiber. It was demonstrated that a ratio of 0.682 [123] is sign of hollow core endlessly

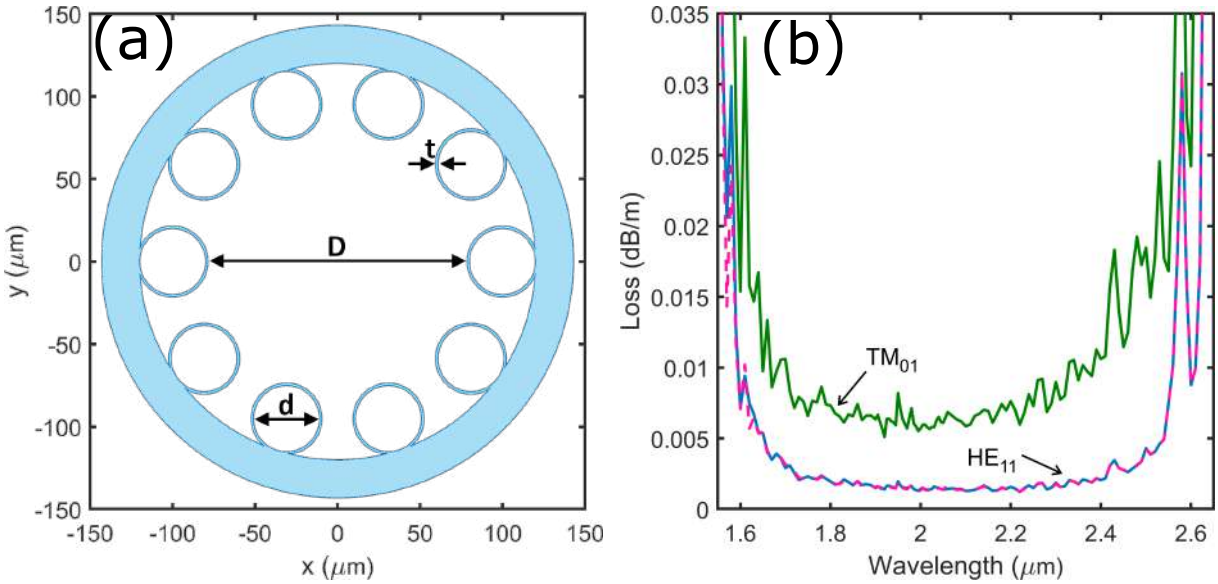

Figure 6.1: Schematic of an anti-resonant fiber (ARF) with an inner diameter D, supported by 10 anti-resonant elements (AREs) with wall thickness t and inner diameter d (a). The numerically calculated loss diagram is shown in (b), illustrating the anti-resonant low-loss bands.

Table 6.1: Hollow core anti-resonant fiber parameters

description	symbol	value
hollow core inner diameter	D	157 μm
number of capillaries	-	10
capillary inner diameter	d	40 μm
capillaries wall thickness	t	1.5 μm
fused silica refractive index	n	1.4373
$\frac{v_{ph}^{TM}}{c} - 1$	-	$1.15 \cdot 10^{-4}$
$\frac{v_{ph}^{HE}}{c} - 1$	-	$4.54 \cdot 10^{-5}$

single-mode which means that the fiber is anti-resonant for the fundamental core modes and resonant for higher order modes allowing for their propagation toward the cladding.

As mentioned in chapter 4, field descriptions were first discussed by Marcatili and Schmeltzer [73] in a simple case of hollow core dielectric waveguides with infinite cladding based on a derivation from Stratton [74]. Modern analytical approaches describing fields in more complex e.g. ring-type ARFs rely on these general field formulations albeit with modified propagation constants [94]. We note that this derivation assumes non-resonant conditions and a large core diameter compared to the wavelength ($D >> \lambda$); this leads to propagation constants near free space ($k_z \approx k_0$). We are particularly interested in the accelerating TM_{01} and fundamental

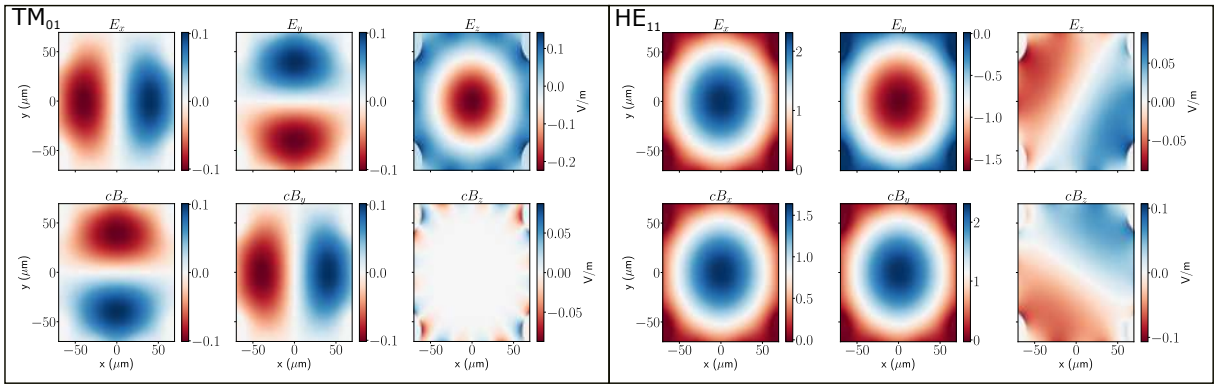

Figure 6.2: Field maps for the TM_{01} (left) and HE_{11} (right) modes. The fields maps were generated with COMSOL and imported to ASTRA. The anti-resonant elements are especially noticeable in the outer portions of the longitudinal fields.

deflecting HE_{11} modes which take the form [73],

$$TM_{01} = \begin{cases} E_r = ik_1k_zJ_1(k_1r) \\ E_z = k_1^2J_0(k_1r) \\ cB_\theta = ik_0k_1J_1(k_1r) \end{cases}$$

$$HE_{11} = \begin{cases} E_r = i\big(k_z^2\frac{J_2(k_1r)}{k_1^2} + \frac{1}{r}\frac{J_1(k_1r)}{k_1}\big)\cos(\theta) \\ E_\theta = i\big(k_0^2\frac{J_2(k_1r)}{k_1^2} - \frac{1}{r}\frac{J_1(k_1r)}{k_1}\big)\sin(\theta) \\ E_z = k_0\frac{J_1(k_1r)}{k_1}\cos(\theta) \\ cB_r = -ik_0k_z\frac{J_2(k_1r)}{k_1^2}\sin(\theta) \\ cB_\theta = ik_0k_z\frac{J_2(k_1r)}{k_1^2}\cos(\theta) \\ cB_z = -k_0\frac{J_1(k_1r)}{k_1}\sin(\theta) \end{cases} \tag{6.1}$$

where ω is the angular frequency, $k_0 = 2\pi/\lambda = \omega/c$ is the wavenumber in free space, $k_z = \omega/v_p$ is the propagation constant, J_m is the Bessel function of the first kind, θ is the angular coordinate and $k_1 = \sqrt{k_0^2 - k_z^2}$; for brevity, the complex propagation phase $e^{i(\omega t - k_z z)}$ has been omitted from the equations. ARFs operating in vacuum support phase velocities beyond the speed of light ($v_{ph} > c$).

The fields were also calculated with the wave optics module in COMSOL [53] using the finite element method to solve Maxwell's equations in the frequency domain. The field maps for both the TM_{01} and HE_{11} modes are shown in Figure 6.2. Both fieldmaps are normalized to 1 W of input power. Figure6.3 shows that the calculated fields are in good agreement with the analytical descriptions but toward the AREs, significant discrepancies appear. The difference between the integrals of the field normalized calculated ($E_z^{(c)}$) and analytical ($E_z^{(a)}$) fields within the core is $\int_{-r}^{r} dr \frac{(E_z^{(a)} - E_z^{(c)})}{E_z^{(c)}} \sim 11\%$.

Finally, in Figure 6.4 we show the calculated n_{eff} and dispersion as a function of wavelength for both the TM_{01} and HE_{11} modes for a fiber with dimensions described in Table 6.1.

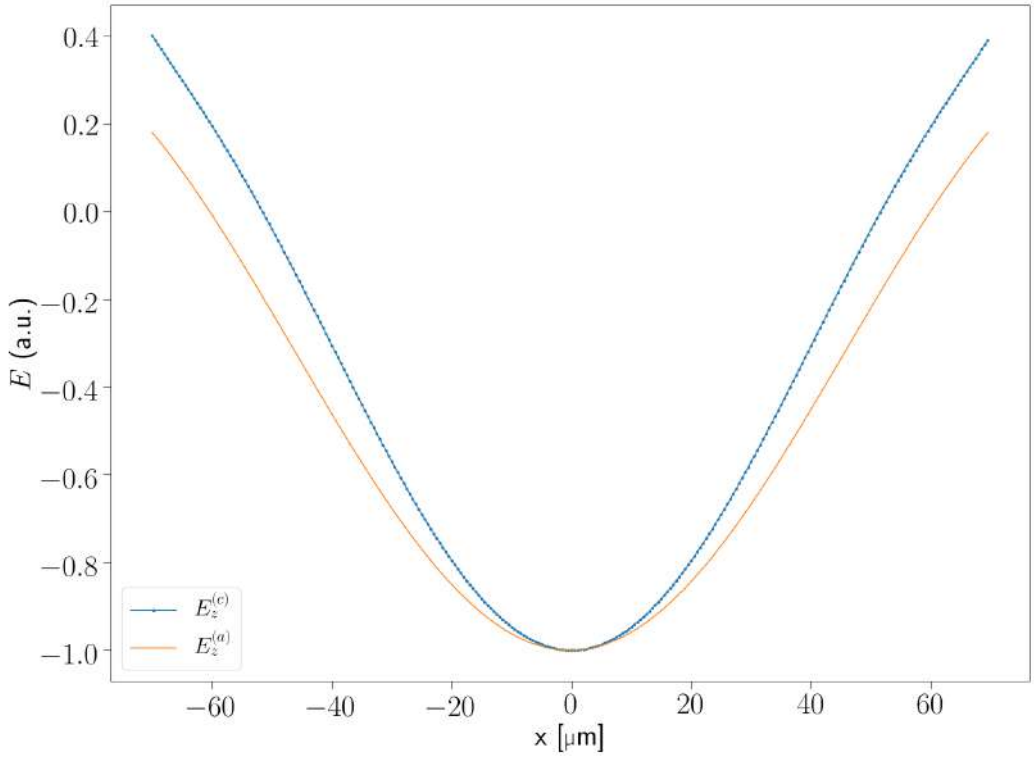

Figure 6.3: Longitudinal electric field of TM mode calculated by COMSOL $E_z^{(c)}$ and analytical formula6.1 $E_z^{(a)}$.

6.1.1 Considerations about ASTRA simulations

In this section the assumptions took for running simulations in ASTRA will be discuss. As aforementioned, first ARF modes have been simulated by COMSOL, then the fieldmaps were adapted to ASTRA format. In order to reproduce the electro-magnetic fields supported by the fiber, in ASTRA the travelling wave consists of the superimposition of two standing waves with relative phase of $\pi/2$ as discussed in [48]. In addition, the inner surfaces of the fiber were simulated by inserting a cylindrical aperture with a slightly smaller diameter than the original fiber. The reason for this difference is that in the vicinity of the capillaries, electromagnetic fields interact with the electron beam producing electron loss. Our assumption is that an electron beam propagating inside the simulated aperture (without particles loss) is able to propagate into larger fibe aperture without collisions with the fiber boundary.

Due to the relatively long simulation times required with space charge, we also compared results without space charge, to support the exploration of a large parameter space. Since the low-charge electron beam is considered in the ultra-relativistic regime (100MeV), the effect of the space-charge is anticipated to be negligible. In fact, we found negligible differences between simulations with and without space charge for the ASTRA parameters described in Table 6.2. However, the final simulation results are reported including the space-charge forces and stated explicitly.

Finally, an important consideration has made about the maximum accelerating gradient supported by the fiber. Figure 6.7b) shows the typical donuts-shape of a TM_{01} mode radially polar-

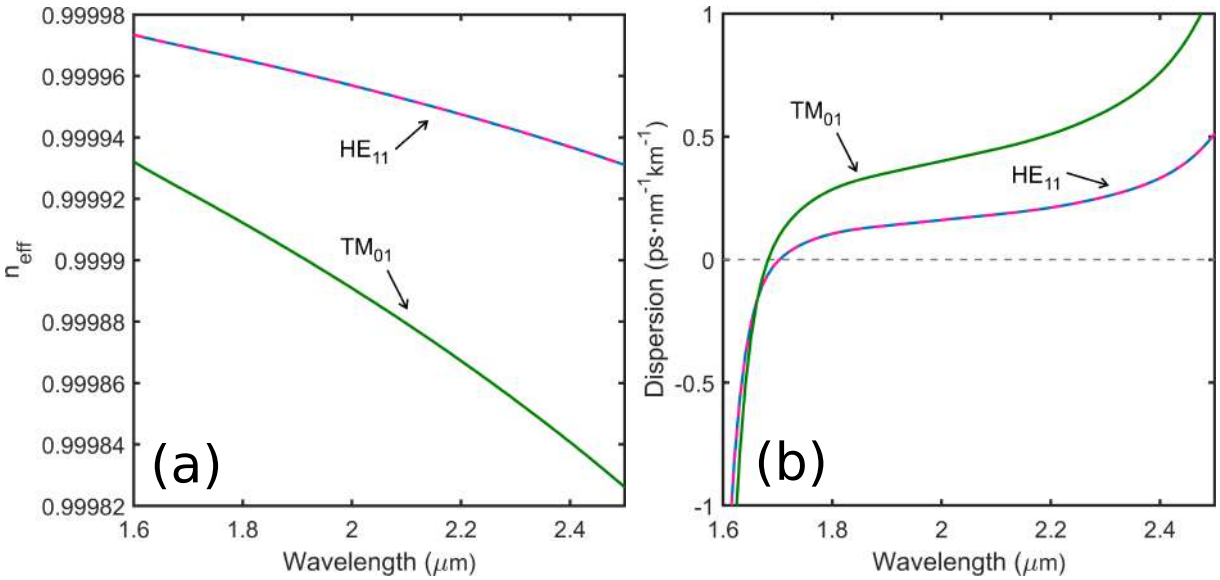

Figure 6.4: The effective refractive index (n_{eff}) and dispersion are shown in (a) and (b) respectively, for the HE_{11} and TM_{01} modes.

Table 6.2: ASTRA parameters

description	symbol	value
macroparticles	-	10^5
charge	e	-500 fC
radial SC bins	Nrad	30
long. SC bins	Nlong	100
max. Runge-Kutta timestep	H_{max}	1 fs

ized; the average power of the electromagnetic fields is estimated by integrating the time-average Poynting vector over the ARF cross-section, which is given by eq.6.2,

$$S_z = \frac{1}{2}(\vec{E} \times \vec{H}^*), \tag{6.2}$$

where E and H^* are the electric and the complex conjugate magnetic field, respectively.

Due to the laser induced damage threshold, we assume 0.5 mJ as laser energy which is compatible with the 2 μm ARES/SINBAD laser system (see chapter 7 for laser parameters) and leads to the maximum accelerating gradient of ≈180 MV/m. Larger gradients could be possible but preliminary experimental investigations into coupling/damaging seem to confirm as 0.5 W the maximum imput power supported by the ARF employing the SINBAD/ARES laser system.

6.2 Accelerating mode TM_{01}: energy gain, energy modulation, microbunching

The TM_{01} mode is the backbone of conventional radiofrequency (RF) accelerators supporting a longitudinal accelerating field routinely used to increase beam energies. It is often desired to utilize a relatively small bunch length compared to the accelerating wavelength to minimize the

energy spread of the accelerated beam. While RF linacs generally have insignificant RF focusing in the ultra-relativistic regime, the phase velocities supported by ARFs are larger than the speed of light, supporting azimuthally-symmetric transverse forces. Here we investigate the utilization of a laser driven TM_{01} mode with an electron bunch.

As aforementioned, ARF was simulated using the finite element modelling COMSOL which provides the field map plotted in Figure 6.5 and $n_{eff} = 0.999884970800487$ as effective index of refraction for the mode. Thus, the phase velocity of the mode exceeds the speed of light.

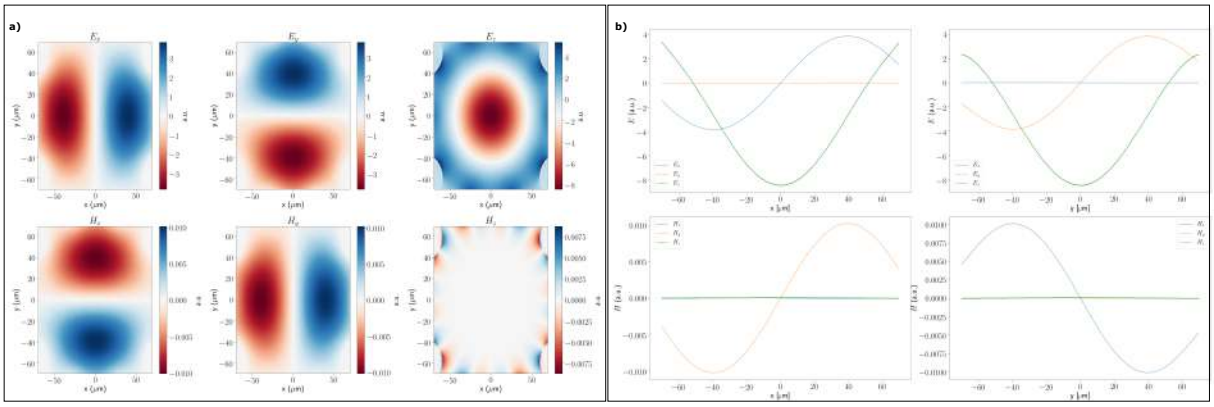

Figure 6.5: a) Electromagnetic field profile in arbitrary unit; b) Amplitude of electric and magnetic field of TM_{01} mode for the simulated ARF.

A primary limitation to electron beam interactions in ARFs is the distinction between massive particle velocities (v_e) being bound below the speed of light, in contrast to the phase velocities of modes in ARFs being bound beyond the speed of light. However, while that fiber seemingly does not support synchronous modes, it does permit mm-scale interaction lengths between the phase velocity (v_{ph}) and electron bunch velocity before the dephasing affects the electron beam quality. The interaction length before slipping by a half wavelength $\lambda/2$ is given by,

$$L < \frac{\lambda}{2(\frac{v_{ph}}{v_e} - 1)}. \tag{6.3}$$

leading to an interaction length for efficient acceleration of ~8 mm for a beam energy of 100 MeV. Millimeter scale structures powered with sub-mJ pulses are sufficient to impart significant longitudinal and transverse momentum distributions in the ultra-relativistic regime, as discussed in the following.

The fields employed in our simulations were calculated with COMSOL[53] and imported directly into ASTRA[48] for beam dynamics simulations. Figure 6.5a) illustrates the electromagnetic fields profile in arbitrary units for the simulated accelerating mode TM_{01} while the evolution of the electric and magnetic field along the horizontal x- and vertical y- direction are plotted in Figure 6.5b). Since $v_{ph} \neq c$, the longitudinal electric field, E_z, is transversely dependent, i.e. particles at a same phase will gain different energies for different radial offsets. This effect comes from Maxwell equation which for the longitudinal electric field reduces to

$$\nabla_{\perp}^2 E_z = (k_0^2 - k_z^2) E_z \neq 0 \tag{6.4}$$

resulting in E_z parabola-like shape shown in Figure 6.5b). This behaviour comes from the

Bessel function in the eq. 6.1. This effect increases the energy spreads and also transverse focusing/defocusing forces. The general forces acting on an electron with velocity $\vec{v} = v_e\hat{z}$ can be calculated by the Lorentz force:

$$\vec{F_L} = e\Big((E_r - \beta cB_\theta)\hat{r} + (E_\theta + \beta cB_r)\hat{\theta} + E_z\hat{z}\Big) \tag{6.5}$$

where e is the electron charge, $(\hat{r}, \hat{\theta}, \hat{z})$ are the identity vectors for the cylindrical coordinate system and $\beta = v_e/c$ is the normalized beam velocity for the simulated 100 MeV high energy electron beam. From eq. 6.5, the transverse forces within the ARF can be calculated, using the field approximations eq. 6.1,

$$F_r = ek_1k_0J_1(k_1r)\big(\beta - n_{eff}\big)\sin(\Psi), \tag{6.6}$$

where $\Psi = \omega t - k_z z$. This results in the formation of focusing ($\Psi \in (0, \pi)$) and defocusing ($\Psi \in (\pi, 2\pi)$) forces along the bunch and also admits points with no transverse forces for $\Psi = 0$ and $\Psi = \pi$, as illustrated in Figure6.6a).

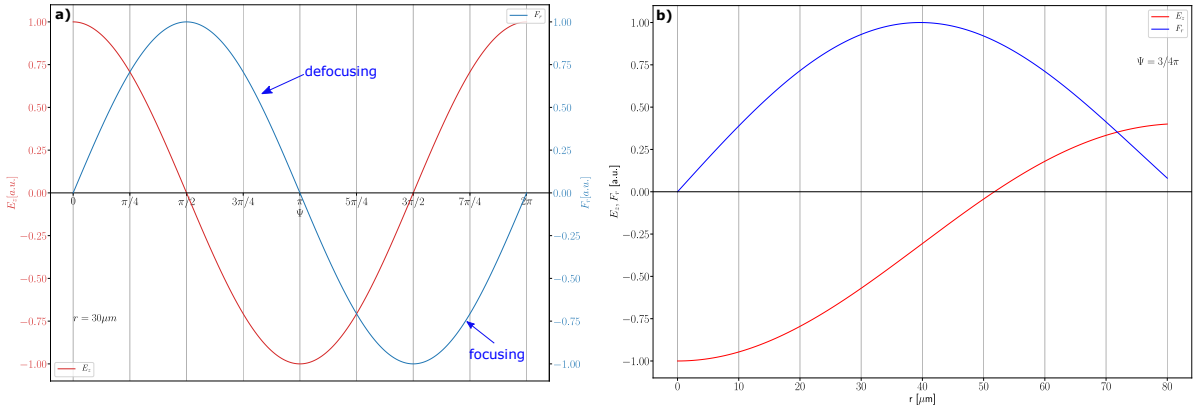

Figure 6.6: Longitudinal electric field E_z and transverse forces F_r for TM_{01} mode: a) Cosine- and Sine-like propagation behavior along the axis fixing distance from the core $r = 30\mu m$ of E_z and F_r, respectively, and b) an example of their evolution along the radial direction setting the longitudinal phase of $\Psi = 3/4\pi$.

In addition there are additional transverse force contributions due to the radial coordinates of different particles due to $k_1 \neq 0$, as shown in Figure6.6b). Electrons at various longitudinal phase and offset will feel different accelerating and defocusing/focusing forces which will affect their dynamics producing acceleration and energy modulation. We also note that the transverse force dependence is generally undesired since it leads to emittance growth, here we mitigate this effect by employing a relatively small beam size compared to the structure aperture.

6.2.1 Electron beam energy gain

For relatively long bunches $\sigma_z > \lambda$, equal portions of an electron beam will be accelerated and decelerated in the different polarities of the longitudinal electric field, E_z. The utilization of short bunches, $\sigma_z \ll \lambda/2$, overcomes this issue and provides a way to accelerate bunches with relatively small energy spreads. It has to be noted that with micron-scale wavelengths, this can

be challenging to accomplish due to limitations in laser-RF synchronizations $\mathcal{O}(100$ fs). In this section a relative short bunches will be injected into ARF powered by TM_{01} mode. From eq. 6.3, the maximum length for efficient energy gain is limited to 8 mm. As shown in Figure 6.8, the electron beam has to co-propagate with the driven laser inside the ARF. It needs to be noted that for the net acceleration application it is required any further equipment. Collimator and dispersive section will be required for the applications which will be investigated in the next section.

Figure 6.7a) shows the preliminary scan of the relative phase between the travelling wave and a 100 MeV electron bunch. The plots show that an injection phase of 250 deg allows for maximizing the energy gain and the transmitted charge while the beam quality is preserved. The injected electron beam parameters are reported in Table 6.3.

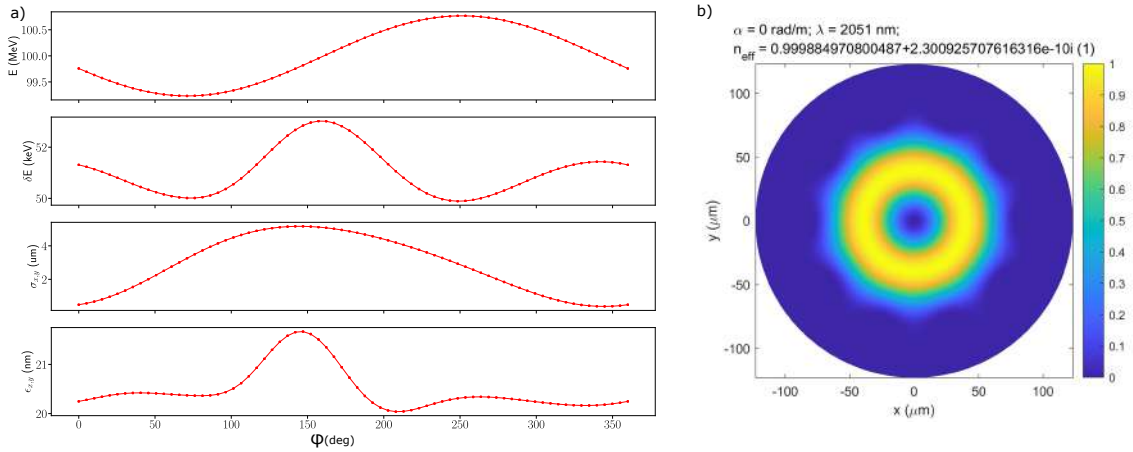

Figure 6.7: a) Final beam parameters as function of the injection phase for 8 mm long ARF: at 250 deg as relative phase the energy gain is maximized while minimizing energy spread and emittance growth. b) COMSOL electromagnetic normalized intensity for the simulated TM_{01} mode and (on top) the twist period, the selected wavelength and the complex effective index of refraction.

Table 6.3: Electron beam parameters

	initial	final
bunch length (σ_t) [fs]	0.02	0.02
transverse beam size ($\sigma_{x,y}$)[μm]	5	2.9
emittance ($\epsilon_{x,y}$)[nm]	20	20.3
aver. energy (E)[MeV]	100	100.77
energy spread (dE)[keV]	50	50
charge [fC]	5	5
accelerating gradient [MV/m]	180	
ARF structure length (L) [mm]	8	

We first investigated how to efficiently match the electron beam into laser-driven ARF by performing a parameter scan over the electron beam size (σ_r) and the correlated beam divergence (σ_r') at the entrance of the structure. Figure 6.9 shows that certain matching conditions are preferred to mitigate emittance growth and energy spread while maximizing energy gain and transmitted charge through the structure. Figure 6.9 b) shows only the final beam emittance in

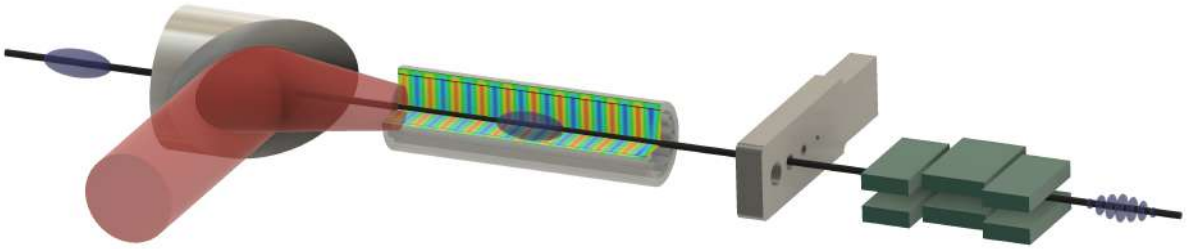

Figure 6.8: Schematic of the presented microbunching setup. An electron beam passes through a laser driven anti-resonant fiber (ARF). The resulting laser excitation produces an energy modulation, and also strongly defocuses electrons periodically. The resulting defocused or spoiled electrons are absorbed on a collimator, producing a high quality microbunched electron beam beyond the collimator. Finally, the addition of a weakly dispersive element can be used to further improve the form factor of the beam by converting the energy modulation into a density modulation.

x-direction but it should be noted that for symmetry the interaction of the bunch with the TM_{01} mode affects both the x and y transverse beam parameters similarly.

Here the initial electron beam parameters are described in Table 6.3 and are consistent with anticipated beam parameters of the ARES linac based on recent beam parameters measured at REGAE [124]. However, to avoid increasing in energy spread, 20 as (attosecond) long bunch has been taken in consideration which is not achievable at ARES/SINBAD. An electron bunch of 5 fC with initial electron beam parameters of $(\sigma_{x,y},\sigma'_{x,y})$=(5 μm,-1 mrad) has been simulated in ASTRA considering 100000 electron including space-charge. The final beam parameters are summarized in Table 6.3. Due to the extremely short bunch, only 5 fC charged beam has been simulated to mitigate the space-charge effects.

Figure 6.10(a) illustrates the average energy and energy spread evolution in a 8 mm long fiber. While the first increases achieving ~0.8 MeV as energy gain, the latter doesn't show relevant amount of change. The injection phase of 250° provides transverse focusing forces and also maximizes the energy gain via phase slippage. As shown in Figure 6.10(b) the transverse beam size is heavily influenced by the transverse forces leading to a focusing of the beam before relaxing in a portion of phase which is less influencing. The transverse emittance growth is especially small for such a nonlinear high-frequency structure making the fiber very promising. Furthermore, bunch compressor simulation results show that 1 fs compressed electron beam is achievable at ARES/SINBAD. Using such a short bunch (1 fs), more recent ARF simulations still show energy gain of 0.6 MeV while emittance and energy spread rise up to 150 nm and 312 keV, respectively.

Although these results are promising, there is at the moment no method to properly synchronize an electron bunch into such an injection phase. In such an experiment, the full range of phases would be sample, therefore the investigation of long bunches seems to be extremely interesting for a future experiment.

6.2.2 Beam manipulation via TM_{01} mode

In this section, we investigate the utilization of a laser driven TM_{01} mode with an electron bunch significantly longer to sample several oscillations along the bunch. The transverse beam dynamics are critical in a velocity mismatched structure, to especially understand the development of the electron beam quality. The transverse forces in an ARF are anticipated to be very large

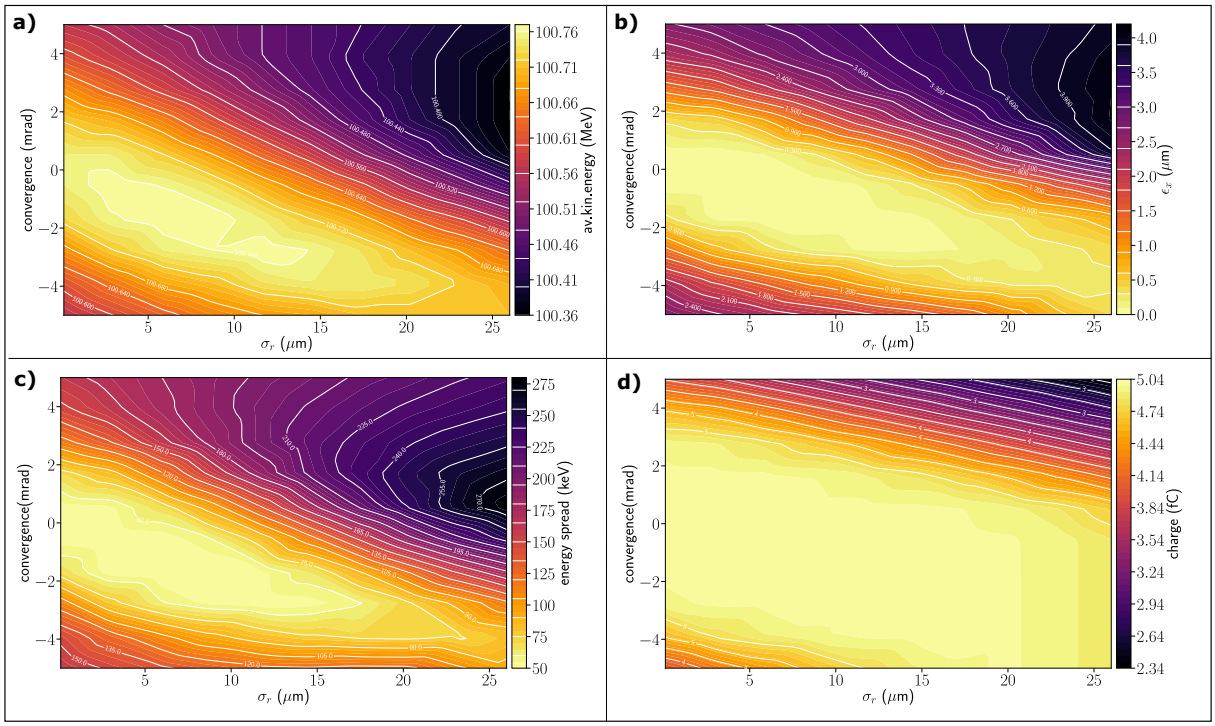

Figure 6.9: Scans of the electron beam transverse size and convergence/divergence into the fiber, i.e. matching. Various final beam parameters are illustrated for an injection phase of ϕ=250 deg. (a) shows the kinetic energy gain, (b) the final beam emittance, (c) the energy spread, and (d) the transmitted beam charge.

since the accelerating fields and driving frequencies are large and the velocity of the electron bunch and phase are mismatched. Via the oscillatory component, the transverse force focuses and defocuses the beam (see Figure6.6) and therefore a relatively long bunch is anticipated to experience interesting longitudinal bunching dynamics.

The transverse forces in the fiber are large and lead to strong focusing and defocusing of the bunch. By controlling the beam size and divergence in the fiber, the final beam properties can largely vary. We therefore first investigated how to efficiently match the electron beam into a relatively low-power laser-driven ARF by performing a parameter scan over the electron beam size (σ_r) and the correlated beam divergence (σ_r') at the entrance of the structure.

In Figure 6.11 a) and b), the resulting rms energy spread and final beam emittance are shown for a 6 mm and 8 mm long fiber, respectively. The initial and final electron beam parameters are described in Table 6.4 with reduced maximum on-axis longitudinal electric field of E_z = 12 MV/m. For a properly matched beam there is no emittance growth and the resulting energy modulation is smooth and sinusoidal, as shown in Figure 6.11 c) and d). In this preliminary example, there is no collimator or dispersive section and the maximum peak-to-peak energy modulation strength (E_{P2P}) is 254 keV and 265 keV . Comparing the two cases, while 6 mm fiber would provide the best final beam quality, the 8 mm fiber could be easier to handle achieving higher peak-to-peak energy modulation. The simulation results are reported in Table 6.4 and include the space-charge.

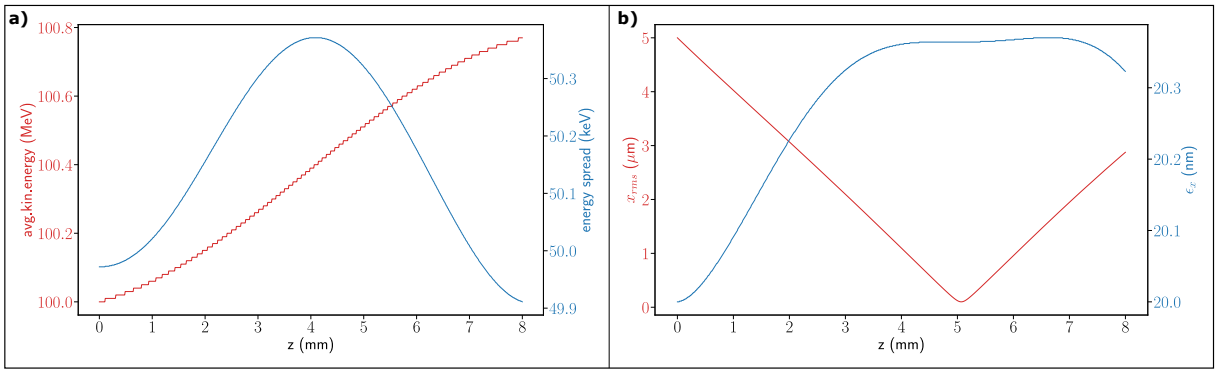

Figure 6.10: Beam parameters for the longitudinal evolution of a short electron bunch; a ~ 180 MV/m acceleration gradient is assumed for an injection phase of 250 degrees. a) The evolution of the kinetic energy (red trace) and energy spread (blue trace) is illustrated. b) Transverse beam dynamics: the evolution of the transverse beam size (red trace) in the longitudinal direction while the normalized emittance is quite constant (blue trace).

Table 6.4: Energy beam manipulation: electron beam parameters for a relatively long bunch.

	6 mm		8 mm	
	initial	final	initial	final
bunch length (σ_t) [fs]	20	20	20	20
transverse beam size ($\sigma_{x,y}$)[μm]	5.1	3.9	5.1	1.2
corr. divergence beam ($\sigma'_{x,y}$)[mrad]	-1.5	1.5	-0.5	-0.45
emittance ($\epsilon_{x,y}$)[nm]	50	50.9	50	55
aver. energy (E)[MeV]	100	100	100	100
P2P energy mod. (E_{P2P}) [keV]	0	254	0	265
energy spread (dE)[keV]	20	37	20	41
charge [fC	-500	-500	-500	-500
accelerating gradient [MV/m]	12	-	12	-

6.2.3 Microbunching with TM_{01} mode

As mentioned in chapter 2, one of the main goal at SINBAD/ARES in the context of ACHIP is to demonstrate net acceleration in a dielectric grating structure. ARES/SINBAD will provide a phase spread across the electron bunch less than $\pi/4$ allowing energy gain. To achieve this goal, i.e. a bunch length less than 1 fs, the microbunching scheme composed by undulator and magnetic chicane has been implemented. In this section we introduce a new concept of microbunching scheme based on a combination of ARF and a collimator placed downstream of the ARF as shown in the sketch of Figure6.8. A similar scheme was proposed in THz-regime by F.Lemery and coworkers in [125] employing a dielectric loaded waveguide (DLW) to modulate the energy of a sub relativistic bunch $\leq$10 MeV and then ballistically bunched to produce the final density modulation by mean drift section. Previously, Antipov et all. [126] demonstrated energy modulation in a chirp electron bunch (with energy $\sim$ 57 MeV) passing through a DLW induced by wakefield.

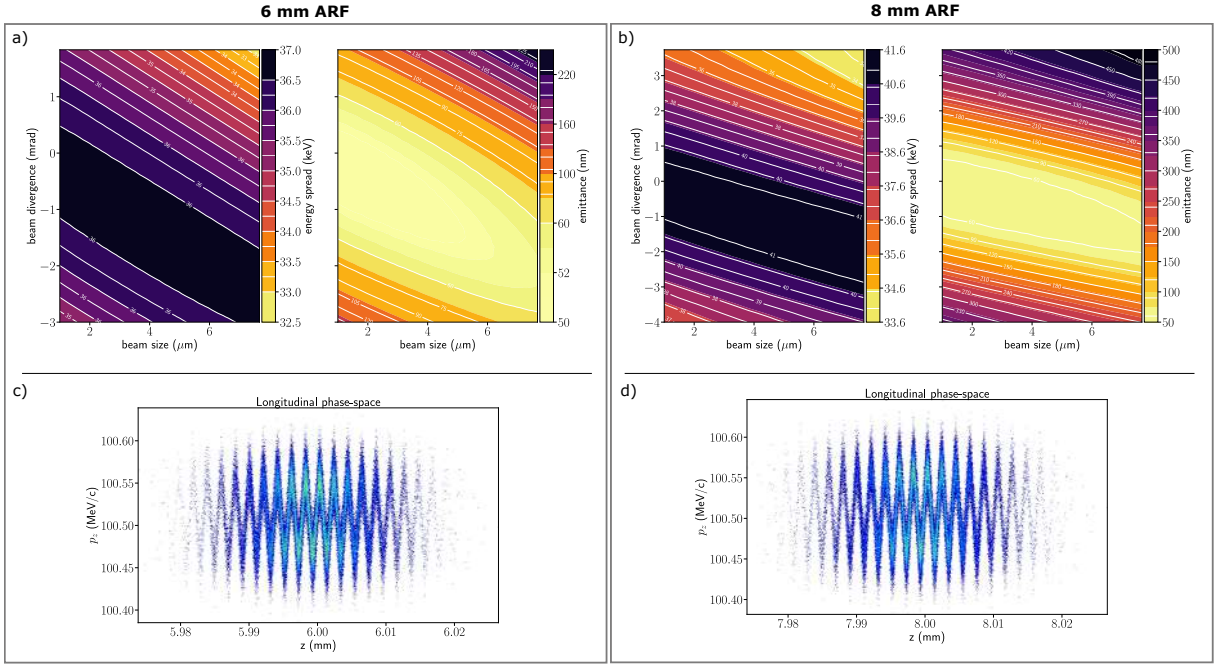

Figure 6.11: Electron beam matching into a low-power ($E_z(r=0) \sim 12$ MV/m, corresponding to an energy of ≈9 μJ) laser-driven fiber with an excited TM_{01} mode in a 6 mm and 8 mm long ARF. The 2D parameter scan of the initial beam size at the structure entrance ($\sigma_r(z=0)$) and the correlated beam divergence (σ_r') is shown. (Top) The resulting energy spread and normalized emittance are displayed in (a) and (b) for 6 mm and 8 mm long fiber, respectively. (Bottom) The sinusoidal energy modulation with the E_{P2P} of 254 keV and 265 keV is also shown for c) 6 mm and d) 8 mm long ARF . Plots c) and d) are space-charge included.

Here we investigated the beam dynamics associated with a high-power laser field near the damage threshold of the fiber, corresponding to $E_z = 180$ MV/m (and an input energy of 0.5 mJ, see [127] for an overview of damage thresholds in ARF and chapter 7 for preliminary damage threshold experiment at SINBAD/ARES laser lab). The resulting beam properties after the 700 μm diameter collimator located 1 m downstream of the 6 mm ARF are displayed in Figure 6.12. The strong transverse forces yield structured beams for both converging or diverging beams. For converging beams (i.e. negative beam divergence), the periodic defocusing forces reduce the beam convergence, leading to larger transmission through the collimator. Likewise for a diverging beam, the focusing forces reduce the divergence of the bunch periodically, also leading to larger local charge transmission through the collimator, as shown in Figure 6.13.

Maintaining a low emittance beam requires the use of smaller beam sizes $\lesssim 5$ μm. Beyond the collimator, the beam has a significant correlated energy spread which can be converted into a density modulation by incorporating a dispersive element. The necessary dispersion required for this transformation can be calculated, $R_{56} \approx \lambda/2\delta \approx -70$ μm, where $\delta = \Delta E_{P2P}/E =$ 1.4 MeV/100 MeV is the fractional energy spread; here E_{P2P} is the peak-to-peak energy modulation strength. The resulting spectral content of the bunch containing N macroparticles at a particular angular frequency, ω, can be calculated with the numerical bunch form factor (BFF)

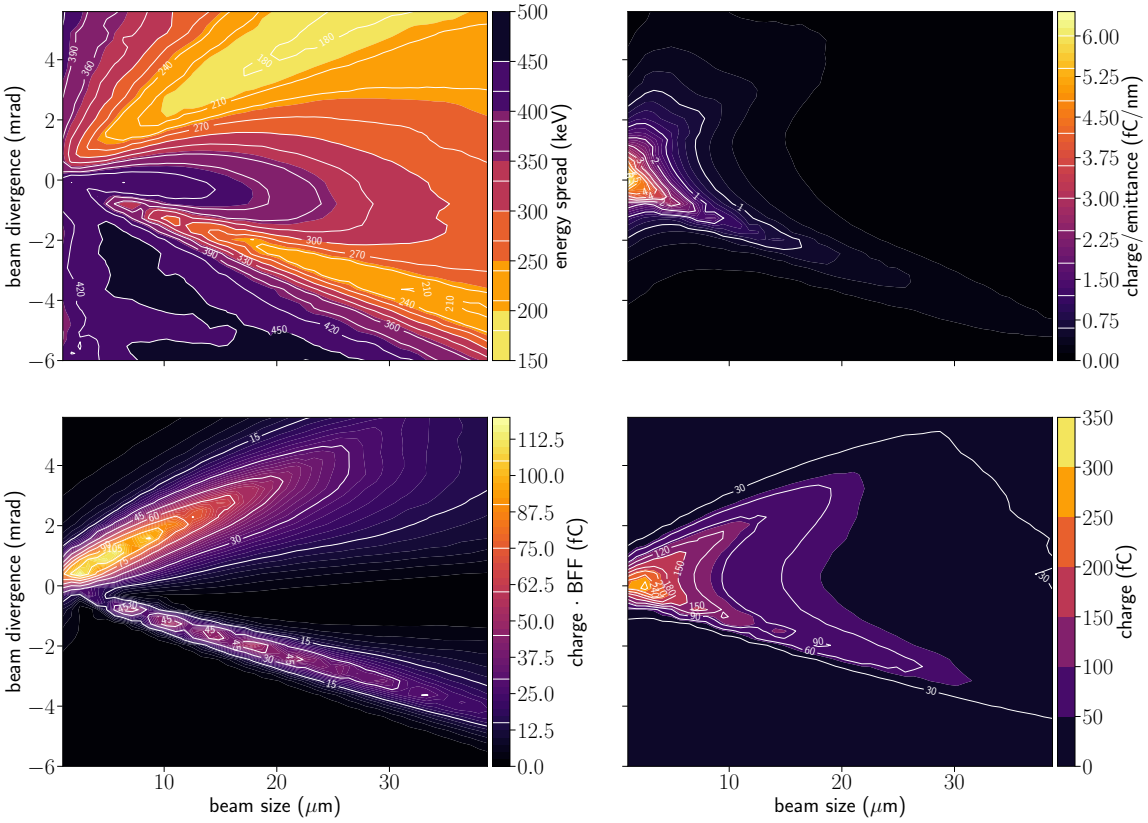

Figure 6.12: Electron beam matching into the a laser-driven fiber with an excited TM_{01} mode in a 6 mm long ARF; the maximum on axis accelerating field is $E_z = 180MV/m$. The 2D parameter scan of the initial beam size at the structure entrance ($\sigma_r(z = 0)$) and the correlated beam divergence (σ_r') is shown. The final beam properties after the collimator (placed 1 m downstream) are illustrated in the scans: energy spread (a), charge over normalized emittance (b), charge times the bunch form factor (c), and charge (d). Good matching regions are observed with large energy spreads, little emittance growth, and maximum charge transmission.

of the macroparticle distribution,

$$BFF^2(\omega) = \frac{1}{N^2}\left(\left|\sum_{i=0}^{N}\cos(\frac{\omega z_i}{c})\right|^2 + \left|\sum_{i=0}^{N}\sin(\frac{\omega z_i}{c})\right|^2\right) \tag{6.7}$$

where z_i is the position of i^{th} particle in the distribution.

In Figure 6.14 we explore how dispersion influences the final spectral content of the distribution following the collimator with radius r=350 μm. Here we apply a linear transformation to the distribution, $z_i \rightarrow z_f = z_i + R_{56}\delta$, and the resulting form factor across a spectral range is shown in (a). Strong harmonic content extends to higher frequencies and is limited by the uncorrelated energy spread of the initial beam distribution. We provide an example of the longitudinal phase space and projected current profile of the distribution immediately after the collimator without dispersion in (b) and finally in (c), we show the resulting longitudinal phase space and projected current profile with $R_{56} = -25$ μm, corresponding to dispersion with the largest spectral content.

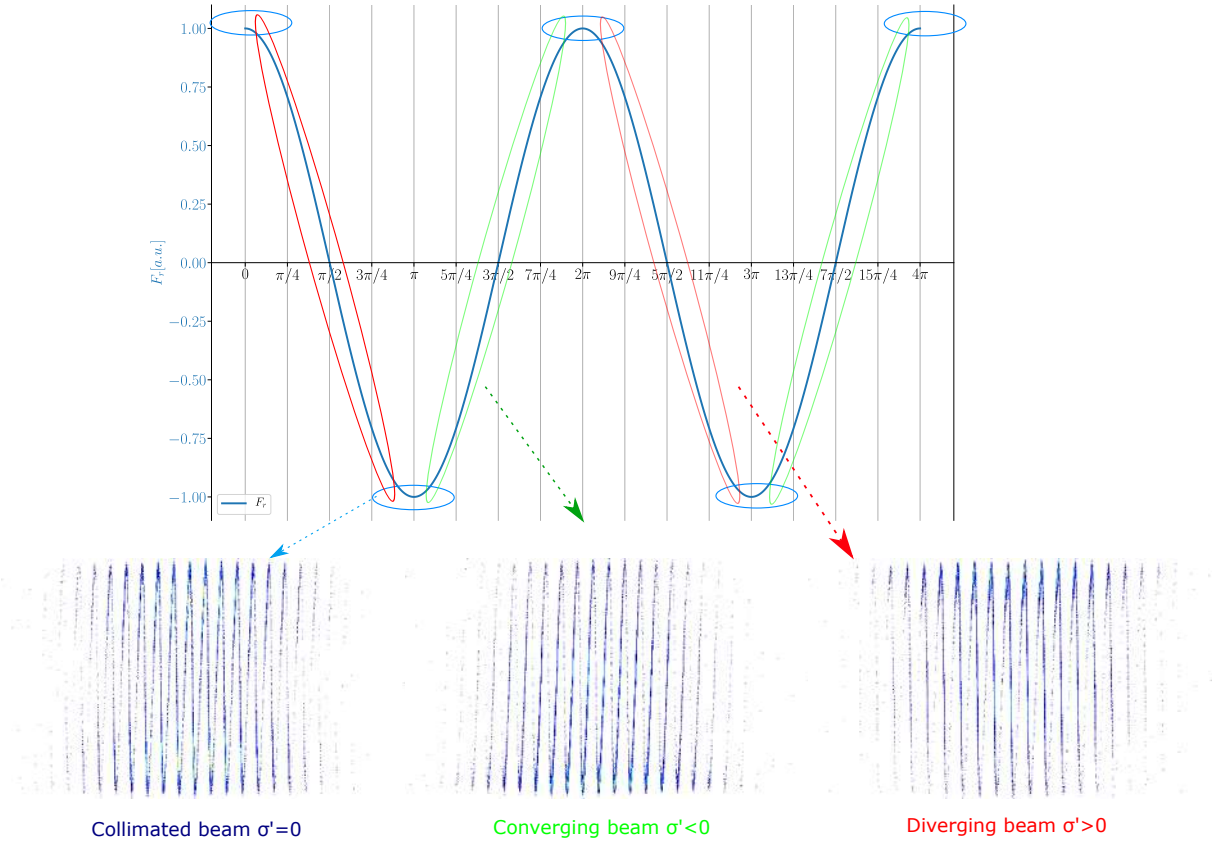

Figure 6.13: Microbunching after ARF and collimator: For a collimated beam ($\sigma' = 0$), larger transmission through the collimator is foreseen for particles in the beam which experience transverse force phases with minimum transverse momentum. For converging beam ($\sigma' < 0$), defocusing forces will reduce the convergence of the bunch for certain phases leading to larger local charge transmission while other phases will lead to blow up the beam with losses of particles on the collimator. Likewise, for a diverging beam, the main part of the beam passing through the collimator is related to the focusing phases.

We note this final density modulation has microbunches with individual FWHM bunch lengths of approximately 140 as. In Table 6.5, we show the initial electron beam parameters (initial), the resulting beam parameters after the ARF (ARF) and the final collimated beam parameters (collimated).

In the stage 2 of ACHIP experiment, the installation of a XFEL phase shifter is planned. The phase shifter is a permanent magnetic device providing enough longitudinal dispersion in order to compress the bunch into fs microbunches. The specifications of this dispersive device are presented in ref. [128] and adapted for ACHIP experiment in F.Mayet dissertation [16]. The possibility of tuning the gap between the magnets allows for controlling the momentum compaction R_{56} achievable with the XFEL phase shifter which can be evaluated as [128, 129]:

$$R_{56} = -2\frac{\lambda_p}{\gamma^2}(1 + \frac{K_p^2}{2}) \tag{6.8}$$

where γ is the average energy of the electron bunch express in unity of electron rest mass, λ_p is the phase shifter periodicity and K_p is the phase shifter parameter which is proportional to the

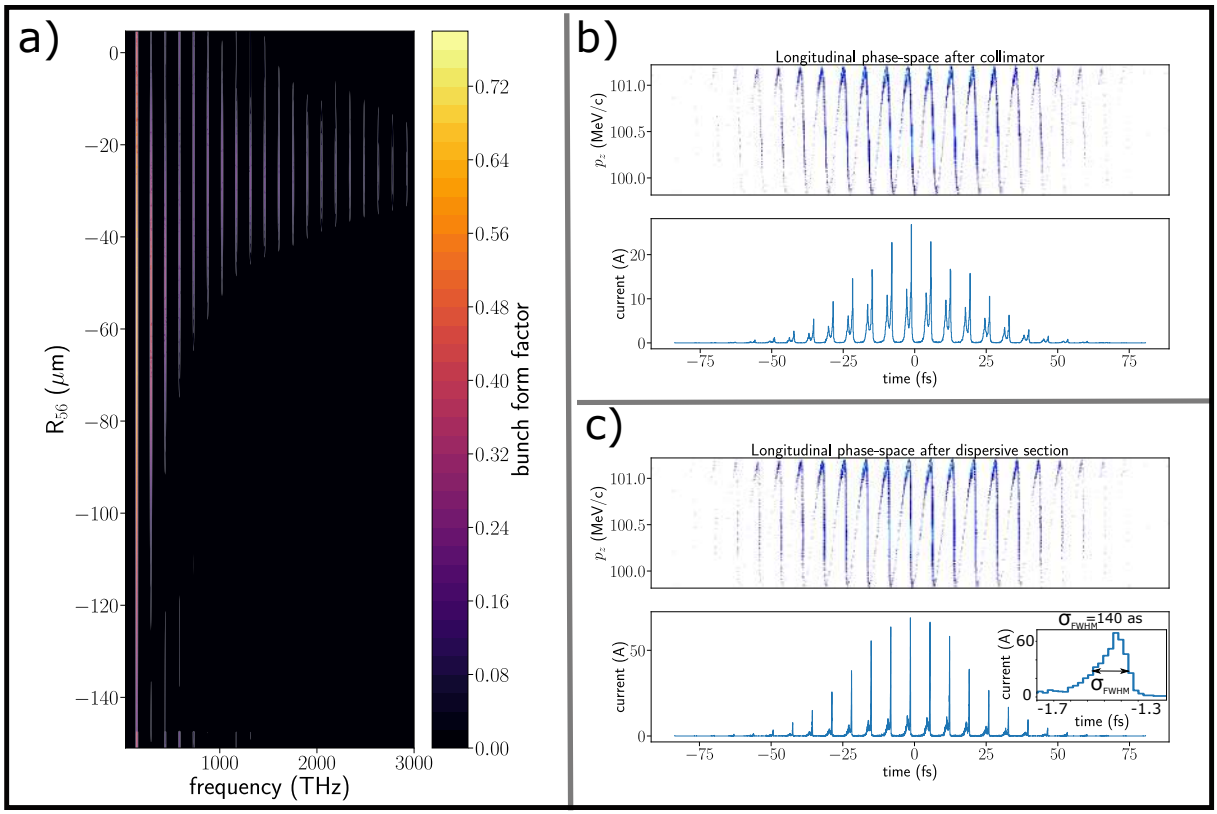

Figure 6.14: The spectral range of the distribution achieved with matching parameters (σ_r^0, σ_r') =(5 μm, 0.5 mrad) is illustrated. Figure (a) shows the BFF evolution as a function of the momentum compaction R_{56}. In (b) an example of the longitudinal phase space and current profile without dispersion is shown. We also display the resulting longitudinal phase space and current profile for the case of $R_{56} = -25$ μm, corresponding to the case of maximum harmonic content. Space charge forces are included in these results.

peak of the magnetic field and its period.

The magnetic field peak is highly influenced by the device design while the effect of the R_{56} on the electron bunch also depends on the energy of the bunch itself. For the high energy bunch simulated in this work the achievable momentum compaction ranges approximately from -54 μm to -0.6 μm corresponding to the minimum and maximum gap of 10 mm and 100 mm, respectively. Thus, the magnetic dispersion for the stage 2 of ACHIP project could be used for providing enough momentum compaction to the ARF microbunching scheme proposed in this thesis.

Table 6.5: Electron beam parameters for microbunching.

parameter	initial	ARF	collimated
bunch length (σ_t) [fs]	20	20	20
transverse beam size ($\sigma_{x,y}$)[μm]	5	8.4	140
emittance ($\epsilon_{x,y}$)[nm]	50	970	140
aver. energy (E)[MeV]	100	100	100
P2P energy mod. (E_{P2P}) [MeV]	0	1.4	1.4
energy spread (dE)[keV]	20	442	368
charge [fC]	-500	-500	-162
ARF structure length (L) [mm]	6	-	-
accelerating gradient [MV/m]	180	-	-

6.2.3.1 A different approach: Microbunching with 8 mm ARF

In this section, we present another approach to investigate the microbunching scheme introduced above. Here the simulations are setup in a similar way to the previous section. Using 8 mm long fiber we first investigate electron beam-ARF matching conditions. Then, we set the aperture of the collimator and its position downstream the ARF. Finally, we add the dispersive section.

The electron beam was matched to the ARF (only) by running simulations to find matching conditions mainly taking in consideration the emittance growth and the transmitted charge. Figure 6.15 a) shows the beam size and the beam divergence range optimizing the beam quality after the ARF. The simulated beam parameter are gathered in Table 6.6 with an electron beam

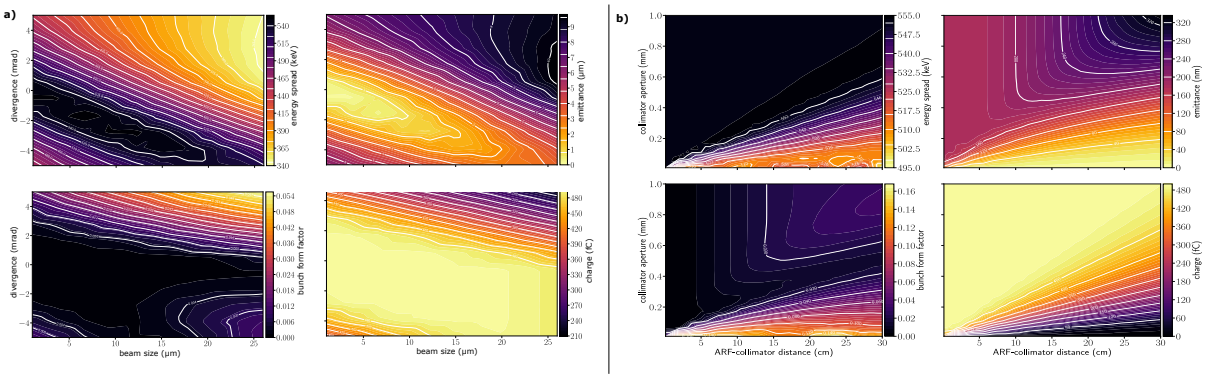

Figure 6.15: a) Beam matching: certain initial parameters mitigate the energy spread and emittance growth while maximizing BFF and transmitted charge. b) Evolution of final beam parameter and BFF while changing the distance between ARF and collimator and its aperture.

divergence of -1 mrad and transverse beam size of 5 μ m.

Figure 6.16(a) shows the phase space and the side view of the modulated beam after the ARF.

The large beam divergence for certain phases of the bunch leads to spoiled beam parameters. To improve beam quality by eliminating unwanted particles we locate a collimator downstream the ARF. Thus, we introduce a beam collimator to dispose of these unwanted electrons that deteriorate the beam parameters. In ASTRA a cylindrical aperture has been simulated changing its aperture and location downstream of the ARF.

The range of beam size and divergence which maximizes the BFF and transmitted charge while optimizing the other beam parameters is shown in Figure 6.15b). For a fixed collimator aperture,

Table 6.6: Electron beam parameters for microbunching using 8mm ARF.

parameter	initial	ARF	collimated
bunch length (σ_t) [fs]	20	20	20
transverse beam size ($\sigma_{x,y}$)[μm]	5	3.36	93
emittance ($\epsilon_{x,y}$)[nm]	50	170	65
aver. energy (E)[MeV]	100	100	100
P2P energy mod. (E_{P2P}) [MeV]	0	2.3	2.2
energy spread (dE)[keV]	100	552	530
charge [fC]	-500	-500	-222
ARF structure length (L) [mm]	8	-	-
accelerating gradient [MV/m]	180	-	-

longer distance between ARF and collimator more particle losses and thus larger BFF. Likewise, fixing the distance and changing the aperture will lead to a larger BFF for smaller collimator radius. The resulting distribution after the collimator appears in Figure 6.17. To dispose the unwanted electrons, a beam collimator with aperture of 200 μm at a location of 20 cm downstream of the ARF has been simulated. A large portion (55%) of electrons are lost into the collimator, see Table 6.6. The remaining phase space and cross section distribution after the collimator is illustrated in Figure 6.17a) while the BFF contents in Figure 6.17b) show that a significant form factor is present at the fundamental frequency with some component in the second harmonic. Finally, the energy modulated microbunches is compressed via a magnetic element which provides dispersion R_{56}. The BFF as function of the momentum compaction appears in Figure 6.18a). An example of the 1D BFF for R_{56}=55 μm along with the accompanying longitudinal phase space and current profile are shown in Figure 6.18 b)-c). A peak current of 40 Amps appears in the current profiles.

In this case, as foreseen from the microbunching model presented in the previous section and illustrated in Figure 6.13, a positive momentum compaction is required. Since the beam after the collimator has a negative energy chirp, a special chicane needs to be implemented in order to provide a positive R_{56}. For negative chirped energy bunch, the head particles of the beam has higher energy than the tail particles, thus quadrupoles needs to be included into the dispersive section, as reported by [130]. Quadrupoles flip the trajectories of the particles in order that the higher energy particles follow a longer path w.r.t. the lower particles resulting in a negative chirp bunch compressor.

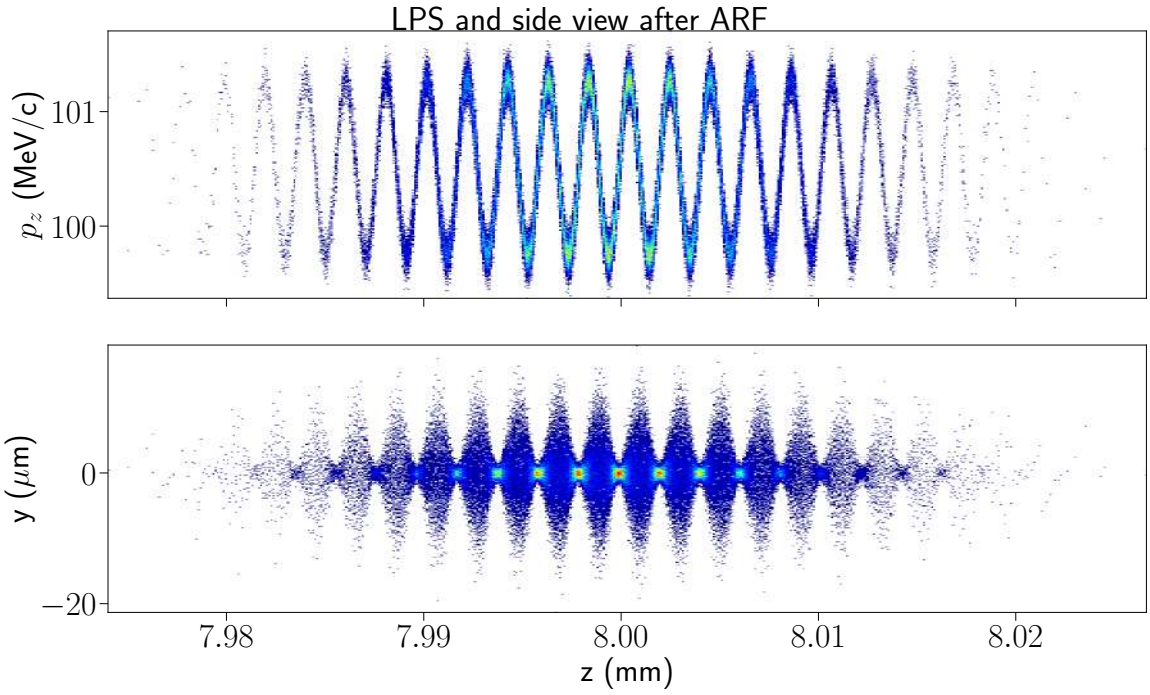

Figure 6.16: Longitudinal phase space and side view of the electron bunch after the ARF

.

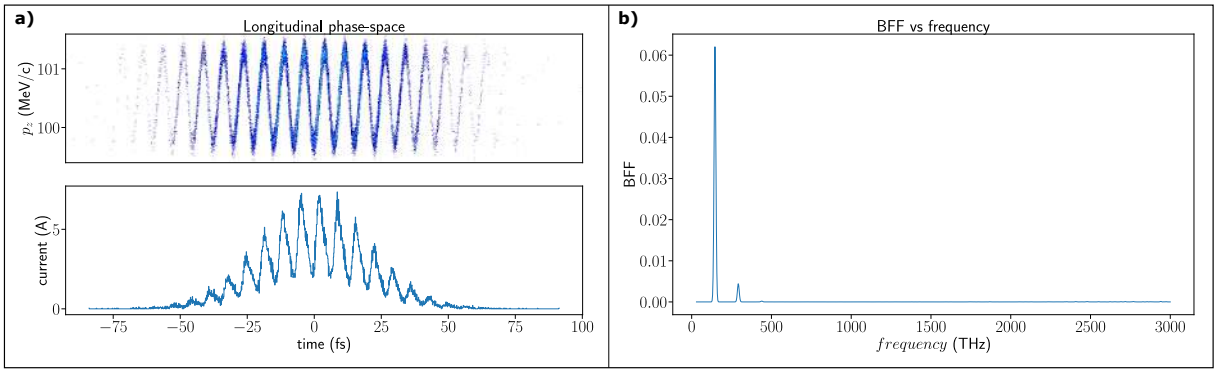

Figure 6.17: a)Longitudinal phase space (LPS) and cross section distribution of the electron bunch after the ARF. b)BFF contents with peak at the fundamental harmonic

.

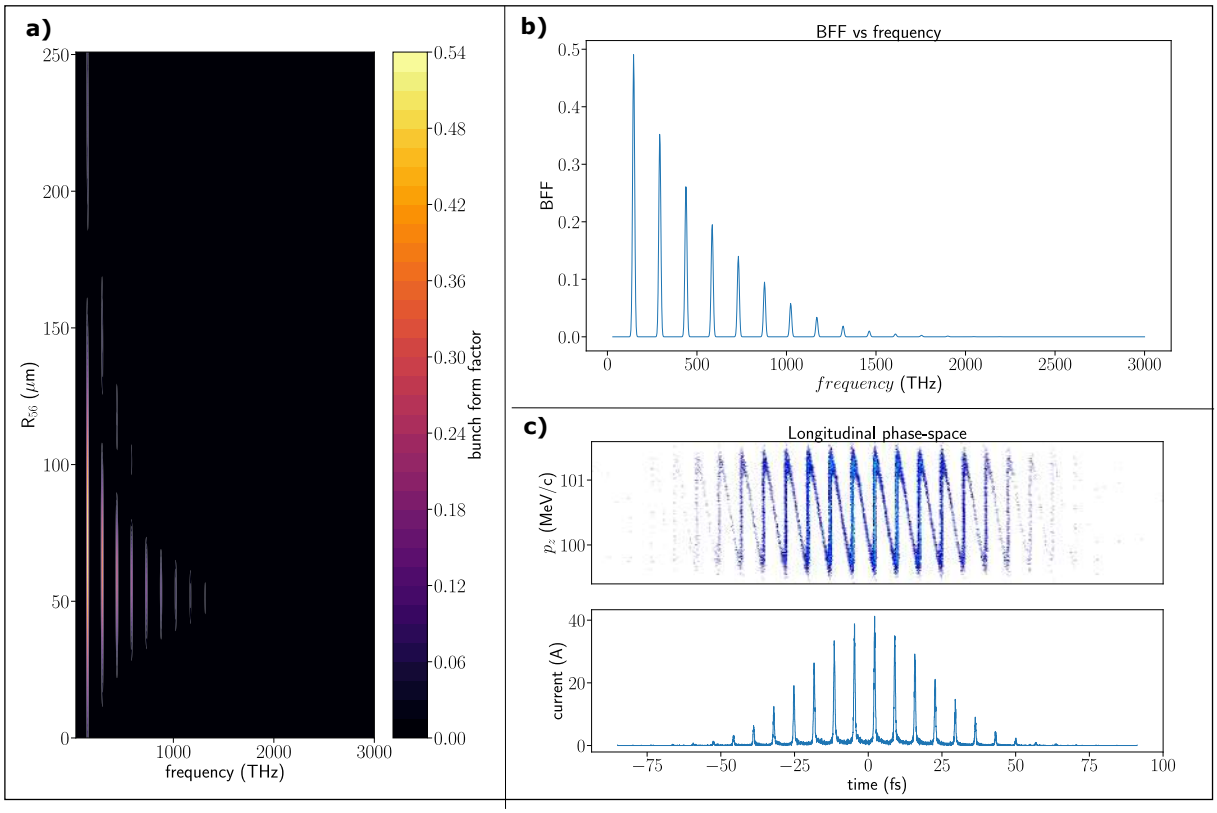

Figure 6.18: a) BFF evolution as a function of the momentum compaction R_{56} provided by a phase shifter. Assuming an $R_{56} = 55\mu m$. b) Illustrates the 1D bunch form factor for the compressed microbunches. c) The longitudinal phase space and current profile are shown for the case of b).

6.3 Streaking mode HE_{11}

The ARF fiber also supports a linearly polarized HE_{11} mode with an effective refractive index $n_{eff} = 0.999954599707247$. In conventional accelerators, the hybrid dipole HE_{11} mode is routinely used for longitudinal bunch diagnostics, supporting the measurement of electron bunch lengths and longitudinal phase spaces when used with a spectrometer. The large transverse forces shear the bunch such that the head and tail of the bunch are transversely stretched onto a screen. The electromagnetic field profile for the simulated ARF is showed in Figure 6.19. The

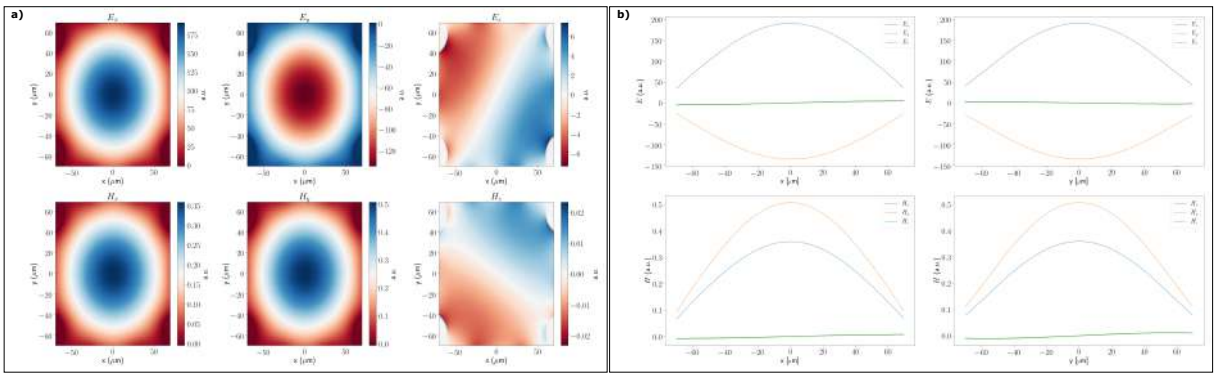

Figure 6.19: a) Electromagnetic field profile in arbitrary unit and b) Electric and magnetic field components of HE_{11} mode for the simulated ARF

field components of the streaking modes HE_{11} are reported in eq. 6.1. All the components are not null leading to a more complicated expression for the transverse forces which have both radial and azimuthal dependency:

$$F_r = \frac{e}{k_1^2}\big(A+B\big)\cos(\theta) i e^{i\Psi} \tag{6.9}$$

$$F_\theta = \frac{e}{k_1^2}\big(-A+C\big)\sin(\theta) i e^{i\Psi} \tag{6.10}$$

defining $A = \frac{k_1}{r}J_1(k_1 r)$, $B = k_z k_0\big(n_{eff}-\beta\big)J_2(k_1 r)$ and $C = k_0^2\big(1-n_{eff}\beta\big)J_2(k_1 r)$.

Transferring the eq. 6.9 and 6.10 in Cartesian coordinates, it yields to:

$$F_x = \frac{e}{k_1^2}\big[\big(A+B\big)\cos^2(\theta) + \big(A-C\big)\sin^2(\theta)\big] i e^{i\Psi} \tag{6.11}$$

$$F_y = \frac{e}{k_1^2}\big(B+C\big)\cos(\theta)\sin(\theta) i e^{i\Psi} \tag{6.12}$$

As for the accelerating mode, a long bunch w.r.t. the wavelength will experience different field polarities and transverse forces intensity at various location in the bunch. Figure 6.20 shows the transverse forces in x- and y- direction. While in the streaking direction the deflecting force will hardly affect the beam, in the y-direction a small transverse force is present due to the asynchronous propagation. In fact, for the synchronous relativistic case $\beta \to 1$,$n_{eff} \to 1$, $k_z \to k_0$, $k_1 \to 0$, the Bessel function can be expanded as:

$$\lim_{k_1 \to 0} \frac{J_n(k_1 r)}{k_1^n} = \frac{r^n}{2^n n!} \tag{6.13}$$

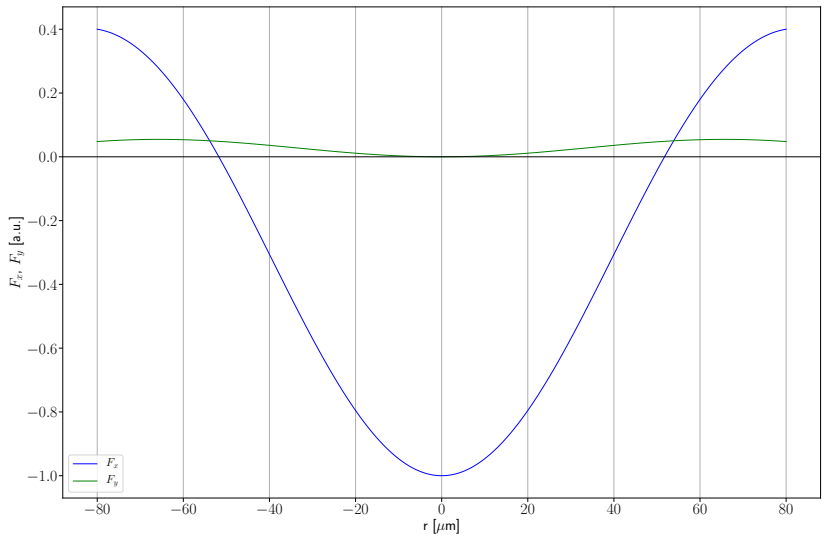

Figure 6.20: Transverse forces for HE_{11} asynchronous mode. The streaking force in x-direction will heavily deflect the electron beam while in the y-direction the strength of the forces slightly affects the beam dynamics.

which simplifies the eq.6.11 and 6.12 to the well known streaking forces:

$$F_x \approx \frac{e}{2} i e^{i\Phi} \Longrightarrow F_x \approx -\frac{e}{2} sin(\Phi) \tag{6.14}$$

$$F_y \approx 0 \tag{6.15}$$

while the longitudinal electric and magnetic fields read as:

$$E_z \approx \frac{e}{2} k_0 x e^{i\Phi} \tag{6.16}$$

$$cB_z \approx -\frac{e}{2} k_0 y e^{i\Phi} \tag{6.17}$$

where $\Phi = \omega t - k_0 z$. For the synchronous mode the deflecting force F_x is constant and F_y is zero within the core while the longitudinal electric and magnetic fields are shifted by $\pi/2$ w.r.t. the deflecting force, as reported in [77, 131]. In case of synchronous motion, the electron beam in rigid beam approximation experiences the deflecting forces F_x and due to the longitudinal magnetic field component it is also affected by a force in the direction perpendicular to the streaking direction leading to an emittance growth. For the ARF, the phase velocity of the mode doesn't match the electron bunch velocity thus synchronous propagation never happens. Hence, an emittance growth in both streaking and perpendicular to the streaking direction is anticipated.

6.3.1 Microbunching with HE_{11} mode

In this section, the linearly polarized mode, HE_{11}, is investigated. As aforementioned, this mode is conventionally used to stretch the beam on a screen and not for energy gain. Thus, in the following the effects of the mode with a relatively long bunch will be presented resulting in an improvement of the microbunching scheme. In order to have a longitudinal electric field vertically

polarized the field maps in ASTRA has been rotated by -0.62 radians and the relevant beam parameters are gathered in Table 6.7.

Table 6.7: Electron beam parameters for a relatively long bunch.

	Initial	ARF
bunch length (σ_t) [fs]	20	20
x beam size (σ_x)[μm]	1	0.8
y beam size (σ_y)[μm]	1	28
x emittance (ϵ_x)[nm]	50	50.4
y emittance (ϵ_y)[nm]	50	12000
aver. energy (E)[MeV]	100	100
energy spread (dE)[keV]	20	26.3
charge [fC]	-500	-500

As in previous section a benchmark has been provided by beam matching and the most promising results are shown in Figure 6.21. Unlike the microbunching scheme implemented using the accelerating mode, for the streaking mode the microbunches are achieved by mean the ARF without collimator or phase shifter. Figure 6.21a) shows the resulting distribution of the modulated and spoiled beam after ARF. The current distribution in the bottom shows a peak of ≈ 90 amps with microbunch length of ≈ 0.2 ps full width at half maximum (FWHM). For this distribution the BFF has been calculated and illustrated in Figure 6.21b). A BFF peak of 0.4 at the second harmonic(f=291 THz) as well as spectral contents for higher frequencies is also reported.

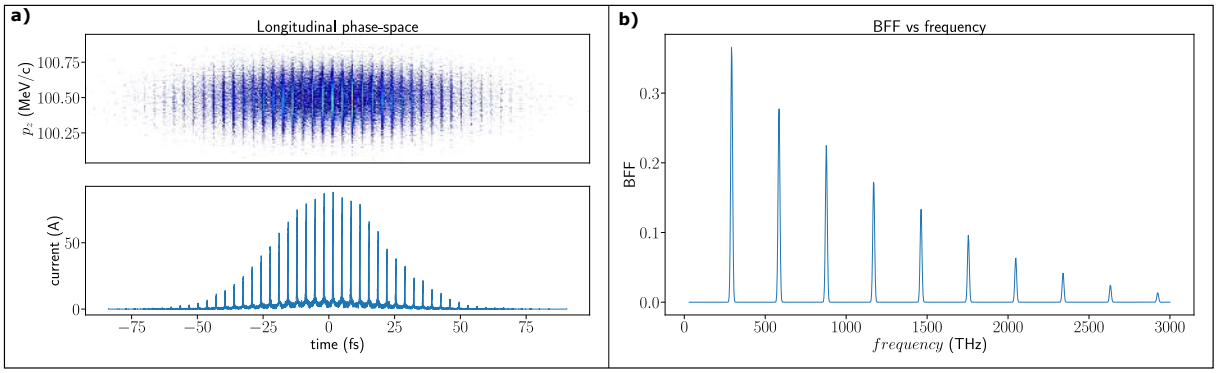

Figure 6.21: a)Longitudinal phase space and current profile of an electron microbunch after the ARF. b)BFF contents with peak at the second harmonic of 0.4 and other contribution for the higher frequencies. Space charge is included

In this case the simulation has been carried out considering a 2 mm long fiber; the large transverse forces of the streaking mode allow for the generation of a microbunched beam with very small input beam powers or with a relatively short fiber. The emittance increase is primarily due to the curvature of the fields and the large beam size employed in the simulations. Furthermore, being the mode not synchronous the emittance growth affects both horizontal and vertical direction as foreseen in the previous section.

6.3.2 Longitudinal bunch diagnostics and metrology with HE_{11}

In conventional accelerators, the hybrid dipole HE_{11} mode is routinely used for longitudinal bunch diagnostics, supporting the measurement of electron bunch lengths and longitudinal phase spaces

when used with a spectrometer.

The resolution of the streaking action is given by,

$$R = \frac{\epsilon}{\sigma_y S} = \frac{\epsilon_n m_0 c^2}{\sigma_y e k V}, \tag{6.18}$$

where ϵ is the geometric emittance, σ_y is the rms beam size in the ARF, S is the shearing parameter, m_0c^2 is the relativistic electron mass (0.511 MeV), $k = 2\pi/\lambda$ is the wavenumber of the driving field, and V is the maximum integrated voltage in the streaking plane. We note this equation relies on a phase advance in the transverse phase space of $\pi/2$ between the ARF and the imaging screen.

Achieving a high temporal resolution requires a large beam size compared to the driving wavelength which is naturally supported in ARFs. Here we explore the streaking performance of a laser-driven ARF. Similar to the previous discussion, we first investigated proper matching through the ARF. Here however, due the relatively short bunch length used in our example ($\sigma_t = 1$ fs), the injection phase plays a significant role.

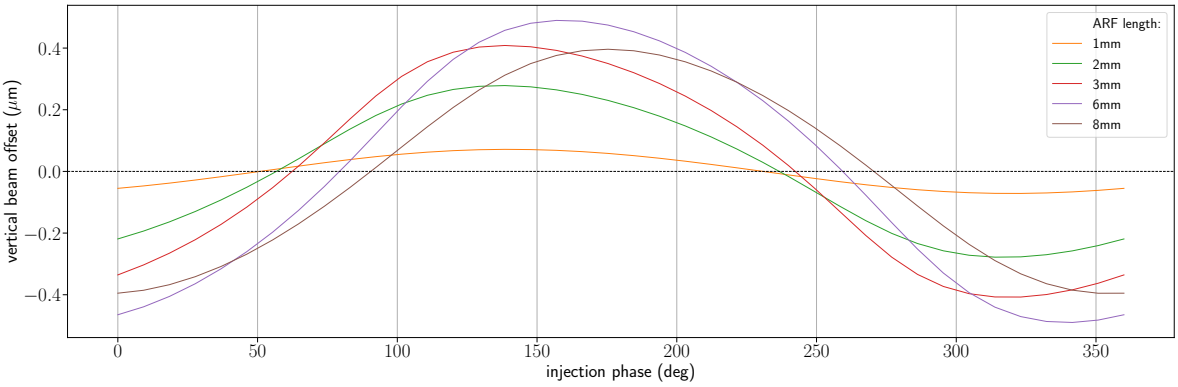

Figure 6.22: The plot shows the vertical beam offset for a single particle varying the injection phase. For a proper phase the particle will pass through the ARF without deflection. Choosing such a phase will bring the entire streaked electron beam to the screen. For a synchronous structure, the bunch will feel phases in order that it is streaked onto screen. For an ARF, the phase slippage plays an important rule. The plot give the phase which provides zero total deflection for the beam over phase experienced by the beam due to the slippage.

We limit our investigation to injecting such that the phase slippage through the structure is symmetric through the zero crossing of the sinusoidal field. Presently, synchronization at this level is beyond the scope of conventional radio frequency accelerators. However with data sorting with e.g. the beam position on a detector screen, a useful measurement could be realized. Alternative laser-based acceleration techniques e.g. plasma, dielectric-laser, or DC accelerators could possibly more easily incorporate this approach.

Here we consider a simple setup consisting of a 2 mm long laser-driven ARF and a screen placed 50 cm downstream. The distance is sufficient to support a phase advance of 80° which only limits the resolution by ∼1.5%. The Astra parameters are tabulated in Table 6.8, the resulting resolution power from Eq. 6.18 is ∼0.5 as. In Table 6.8 are also reported the parameters used for shorter and longer ARFs. In order to support full transmission charge through the fibers with different length, the maximum field strength needs to be reduced. Changing the beam size and fiber length, along with the field strength, leads to a different power resolution which is

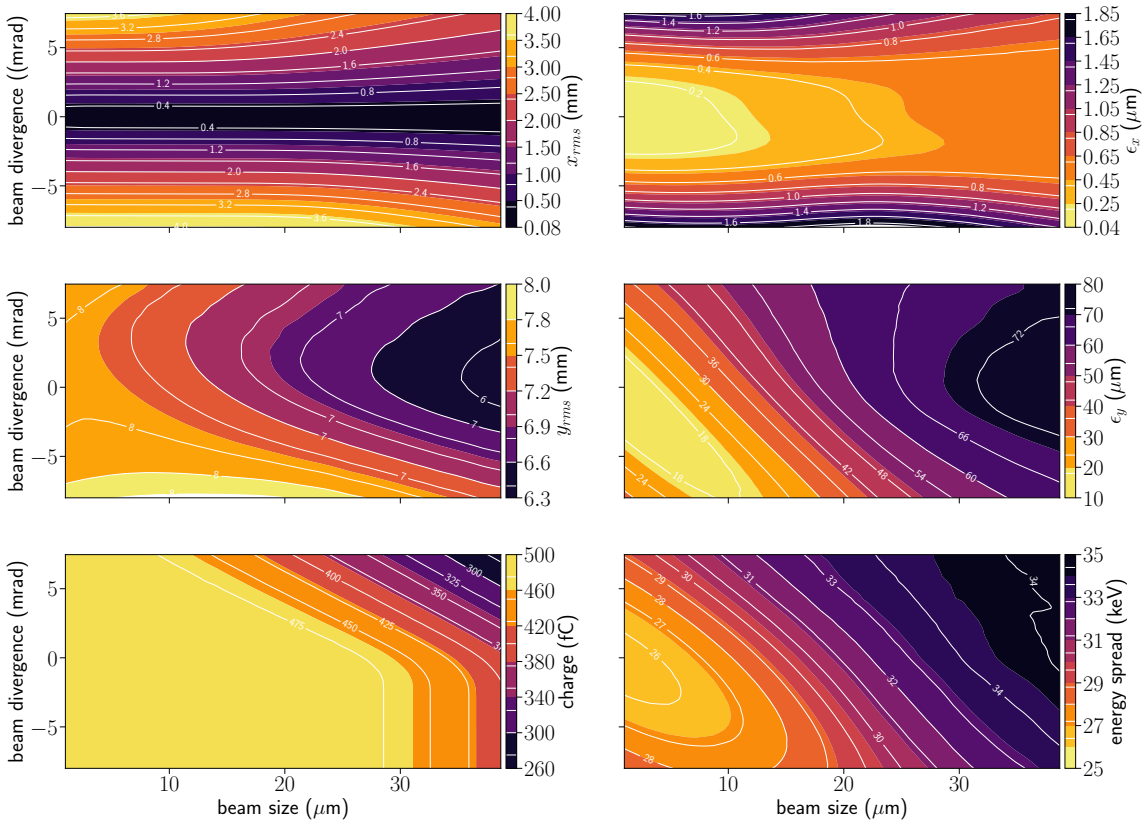

Figure 6.23: The resulting beam parameters 50 cm downstream of the laser driven 2 mm long ARF with an HE_{11} mode. A large range of available initial beam parameters lead to full transmission through the ARF.

limited by the phase advance. For each fiber we performed beam matching. The resulting beam matching scans for 2 mm ARF are illustrated in Figure 6.23 and show the final beam distribution parameters after the subsequent drift. A large range of initial beam parameters are found which show full charge transmission. For a simple configuration without focusing optics between the ARF and screen, a collimated initial beam is desired. We show the resulting streaked beam on the downstream screen for various injection phases in Figure 6.24 with initial beam parameters , (σ_r^0, σ_r'), reported in Table 6.8. In order to avoid particle losses, for a longer fiber is needed to reduce the field strength. For a properly injected phase, the electron beam is simmetrically sheared onto the scream located downstream.

Finally, we now provide an example of the temporal resolution power of the ARF streaking mode. Here we use a modified electron bunch from previous discussion with the following initial parameters: Q=50 fC, σ_E=20 keV, ϵ_r=50 nm, σ_r=15 μm, σ_r'=0 mrad, we energy modulate the bunch with E_{P2P}=30 keV and use R_{56}=-1.5 μm to produce a microbunches with a period of 10 attoseconds, see Figure 6.25. For these considered beam parameters and a field strength of 2 GV/m, the resolution power from Eq. 6.18 is ∼0.45 as. Figure 6.23 and show the final beam distribution parameters after the subsequent drift. This field strength has been achieved employing a 2 μm driving wavelength and a pulse energy below the damage threshold of the fiber. We show the resulting streaked beam 50 cm downstream of the ARF and the corresponding pro-

Table 6.8: ASTRA parameters for the HE_{11} mode for various ARF lengths

description	symbol	1 mm	2 mm	3 mm	6 mm	8 mm
charge [fC]	Q	-500	-500	-500	-500	-500
bunch length [fs]	σ_t	1	1	1	1	1
transverse beam size [μm]	$\sigma_{x,y}$	15	15	5	15	5
correlated beam divergence [mrad]	σ'_r	0	0	0	0	0
emittance [nm]	$\epsilon_{x,y}$	50	50	50	50	50
energy spread [keV]	dE	20	20	20	20	20
phase advance to the screen [degree]	ϕ	83	80	83	63	77
maximum field strength [GV/m]	E_y	2	2	1.4	0.21	0.21
drift length to the screen [cm]	-	50	50	50	50	50
zero-crossing phase [degree]	ψ	230	238	241	260	270
resolution power [as]	R	0.93	0.46	1.32	1.47	3.31

jected distribution in Figure 6.25(b). Here the corresponding microbunch spacing is ≈ 0.17 mm. In experiment, the distributions could be sorted in single-shot measurements to attain bunch length information. In addition, this could also be used to provide information on the bunch arrival time for the development of femtosecond feedback systems.

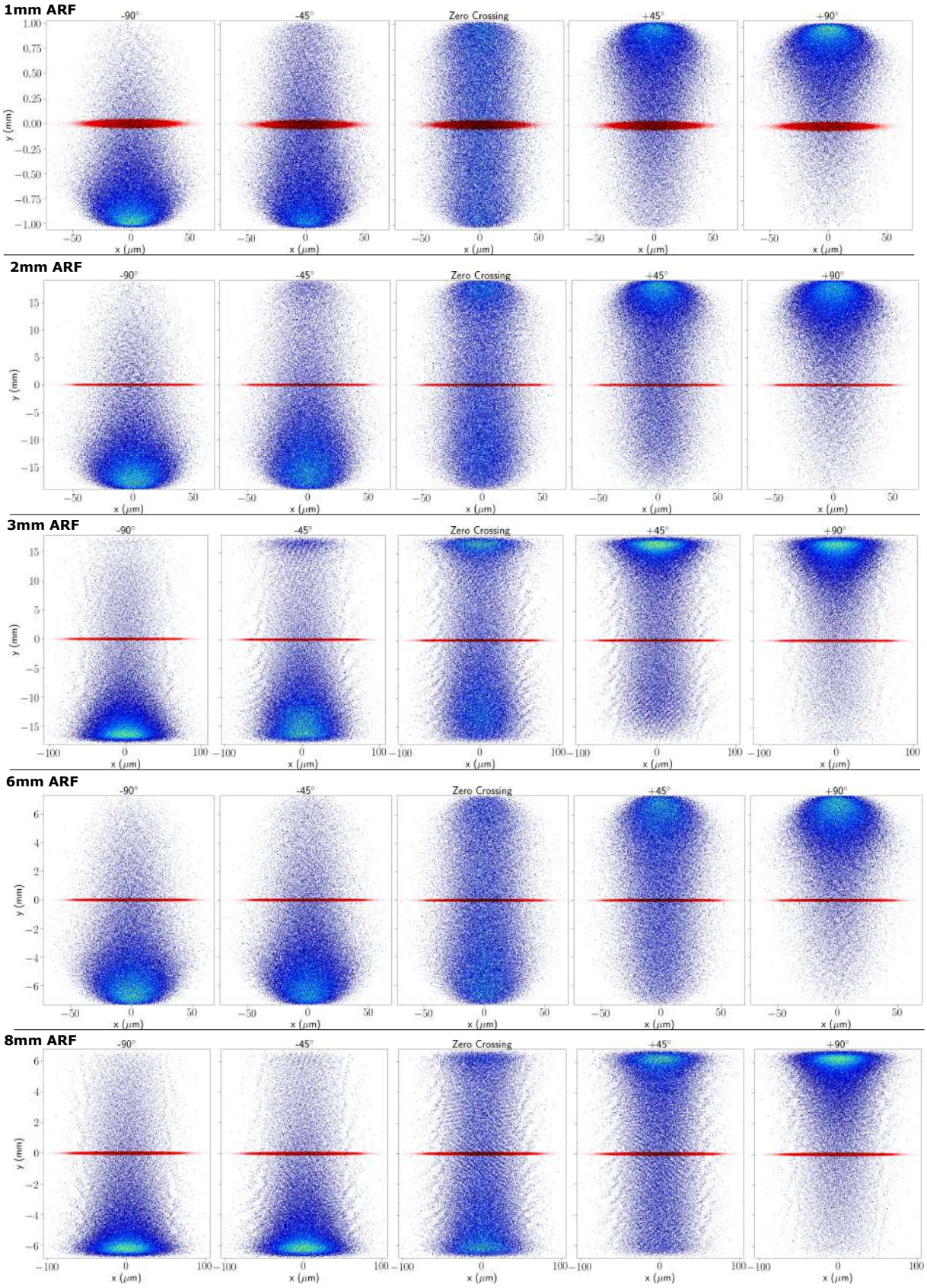

Figure 6.24: The resulting streaked beam 50 cm downstream of a laser-driven ARF with an HE_{11} mode. A 1 fs electron bunch is injected into an ARF with an HE_{11} mode with initial matching parameters reported in Table 6.8. The resulting streaked beam 50 cm downstream of the ARF is displayed for various injection phases; for comparison the unstreaked beam is also shown in red. This simulation includes space charge.

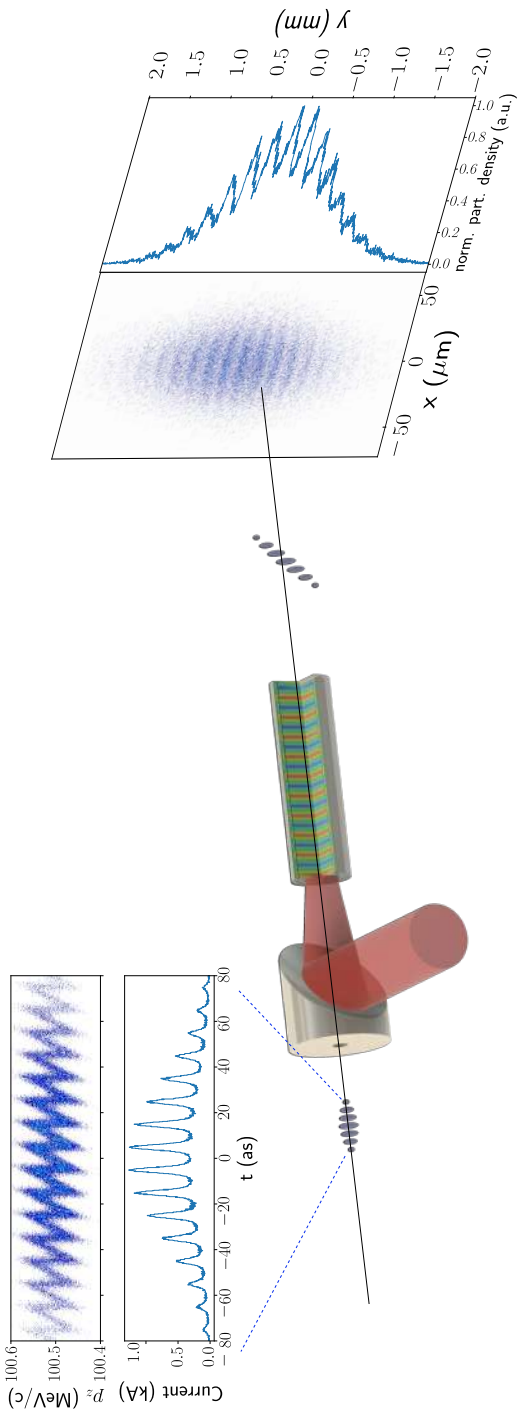

Figure 6.25: An example of the streaking power of the HE_{11} mode. Here we consider an initial electron bunch with a 10 attosecond density modulation, with Q=50 fC, σ_r=15 μm, σ'_r=0 mrad, ϵ_r=50 nm, see the initial LPS and projected current profile (top left). The electron bunch is then injected into the ARF with synchronized laser pulse. The streaking power of the ARF shears the bunch in the vertical plane onto a screen located 50 cm downstream of the ARF. The resulting transverse distribution and projection is displayed, illustrating the resolved 10 attosecond bunches.

6.4 Conclusion

We have proposed and explored the application of laser-driven anti-resonant fibers to accelerator physics. We have shown that the use of the TM_{01} mode could be used to facilitate energy modulation in conventional accelerators. In a more extreme case where the laser power is increased, we also showed that the fiber support an accelerating gradient to produce electron beam energy gain and that the resulting transverse forces could produce ≈ 140 attosecond microbunched beams at the driving wavelength by using a collimator to remove the spoiled electrons. In addition, by using a small dispersive element we showed that beams with large harmonic content could be produced. We expect the simple technique to have applications for beam manipulation, radiation generation and also electron microscopy [132, 133, 134, 135].

We also discussed how the fundamental HE_{11} mode could produce microbunches train and be employed as a bunch length diagnostic with sub-attosecond resolutions. Such a powerful diagnostic could be used to provide information on complex processes in X-ray free electron lasers, but would require data sorting due limitations in synchronization.

7

Preliminary coupling efficiency and laser induced damage threshold tests

One of the main limits for the dielectric laser accelerator is the damage due to the high field intensity of the driven radiation. Exceeding this limit may damage the dielectric material irreversibly. In literature it is common define the damage threshold fluence $F_{th} = \frac{E_{pulse}}{A}$(unit J/cm^2) as the maximum pulse energy before the damage occurs for laser spot size. Furthermore, for example in a DLA grating structure, assuming 100% coupling efficiency to the first harmonic, the maximum accelerating gradient can be estimated as the ratio between the root square of the fluence F_{th} and the pulse length τ of the driven laser. Being the damage threshold limit of a dielectric materials several order of magnitude higher than metallic structures at optical frequencies, dielectric laser accelerators are pointed out as the potential candidates for high gradient accelerators.

For hollow core fiber, coupling efficiency plays an important role in the fluence damage threshold since a better confinement will prevent for damage. ARF usually allows for low loss propagation and high-power transmission. Michieletto and coworkers [136]report an efficiency of 85% with maximum output power of 70W assuming 22 ps pulse 40 MHz rep.rate at 1032 nm laser shot into a 7 capillaries antiresonant fiber.

In this chapter, an overview of the processes leading to laser damage as well as coupling efficiency will be first presented. In the second part of the chapter the first preliminary ARF laser induced damage threshold (LIDT) and coupling experiment at ARES/SINBAD will be reported. There, we are targeting to explore the limits of ARF in terms of laser intensity for future beam manipulation experiments in ARES/SINBAD using laser-driven ARF.

7.1 Basic of laser induced material damage

Damage induced by high intense laser pulses is an event that can arise from several phenomena such as the generation of free-carriers from non-linear ionization, absorption of the laser energy by free-carriers and deformation of the material due to thermal mechanisms. For pulses longer than a few tens of picoseconds usually the damage is described as being mainly due to the transfer of energy from the electrons in the conduction band to the crystal lattice; once the material has accumulated enough energy to be melted, boiled or fractured, then the damage occurs. In this range, the damage threshold fluence shows a trend proportional to the square root of the pulse length $\tau^{1/2}$ [8]. On the other hand, for shorter pulses, it is usual to describe the damage by

first ionization process (PI). In fact, for pulses with τ<10 ps the radiated energy is more quickly absorbed by the electrons than transferred to the crystal lattice. In this case the breakdown is therefore produced by photoionization and then avalanche. This multiphoton ionization is able to produce a plasma of electrons with a density sufficient to generate damage. As reported by Stuart [8] and shown in Figure7.1 a), the transition from the regime dominated by melt, boil and fracture (τ>50 ps) to one characterized by PI (τ<10 ps) is gradual and described by Keldysch formalism.

Wavelength plays also an important role in the LIDT since small changes can affect drastically the damage threshold fluence. Simanovskii et al. [137] demonstrated that for wide-bandgap dielectrics the optical breakdown is due to tunneling ionization followed by avalanche and thus laser absorption by the made plasma considering 1ps laser pulses in the range of frequencies between 4.7 μm and 7.8 μm. For narrow-bandgap dielectric, the tunneling ionization is enough to generate plasma and subsequent damage. Soong [9] using a model based on multiphoton ionization and plasma resonance showed that silicon illuminated by 1 ps pulse within the range of $[1200 - 2200]nm$ exhibits a quasi-oscillating trend of the damage fluence, as reported in Figure7.1 b). In 2015 Gallais [138] demonstrated both theoretically and experimentally that materials with bandgaps in the range [1-10] eV exhibit a linear trend of the damage fluence with $\lambda \in$[310-1030] nm assuming 100 fs pulse length. A theory including pulse length, laser intensity,

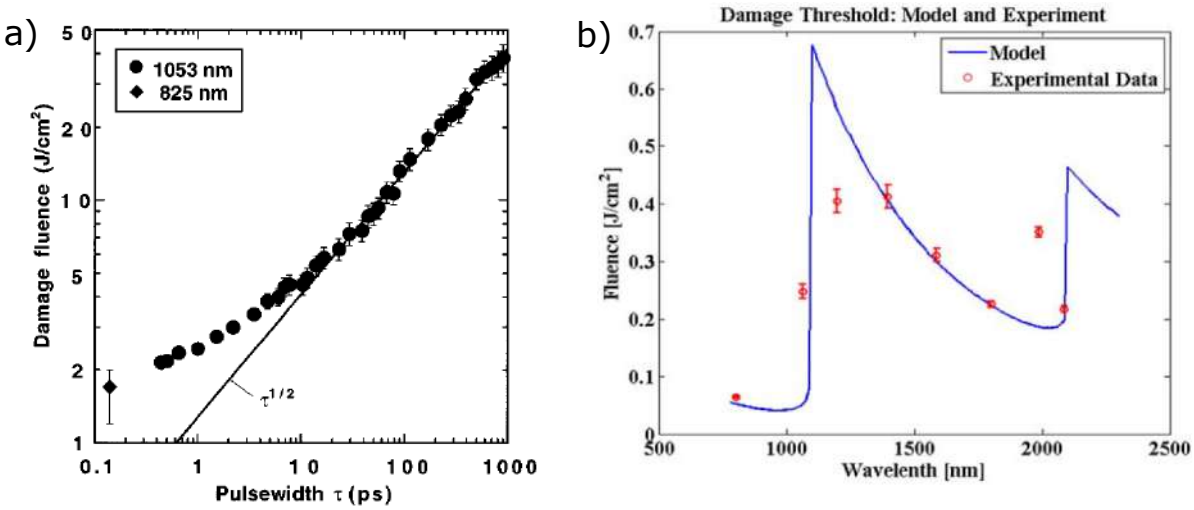

Figure 7.1: Threshold damage fluence for fused silica as function of a)pulse width and b) wavelength. Adapted from [8] and [9], respectively.

repetition rate and wavelength is not yet implemented. In particular for wavelengths of 2 μm and pulse length of 2 ps there is a lack of literature making LIDT test very attractive also in view of future experiments.

7.1.1 Photo-ionization processes

The time range of interest in this work is below the 10 ps, due to the characteristic of the 2 µm ARES laser. As aforementioned there is not a unique theory to describe the damage fluence but the scientific community agrees to identify photoionization followed by avalanche as the key process for laser induced damage materials.

Dielectric or semiconductor materials has an energy bandgap (BG) between conduction and

valence band ranging from few eV to tens of eV [9]. In the interaction between matter and light, sufficient energy needs to be supplied promoting an electron from the valence band to the conduction band. If the energy of the single photon is greater than the BG, linear absorption dominates and the valence electron is promoted to the upper band. Viceversa, if the energy of the single photon is not sufficient then photo-ionization can take place either by tunneling or by multi-photon absorption. These processes are described by Keldysch theory and depending on the value of the so-called Keldysch parameter γ, one of the two effects is dominant [138]:

$$\gamma = \omega \frac{\sqrt{m^* E_g}}{eE} \tag{7.1}$$

where ω is the laser frequency, m^* is the electron reduced mass, E_g is the bandgap energy, e the electron charge and E is the applied electric field. For long wavelength or intense electric field $\gamma << 1$, tunneling effect is the dominant process. Correspondingly, $\gamma >> 1$ is meaning of multi-photon absorption dominant mechanism.

Free electron produced by the early photo-ionization gains energy by absorbing photon from the radiated laser until it achieves sufficient energy to ionize another electron from the valence band by collision (the so-called avalanche or collisional ionization) creating plasma. Once the plasma density reaches a critical value n_c [138]:

$$n_c = \frac{\omega^2 \epsilon_0 m}{e^2} \tag{7.2}$$

the material changes its properties drastically, e.g. refractive index, showing strong absorption and metal-like properties; the energy is accumulated within a thin layer due to the finite penetration depth ($l \propto \lambda$) with damage threshold fluence inversely proportional to the wavelength for fs laser pulse length [139]. The absorbed laser energy is then transferred to the crystal lattice causing damage.

Impurities, dust or damage on the surface of the material can create interference between the scattered and the incoming waves leading to a decrease in damage threshold fluence [140]. Finally, the number of pulses plays an important role in the damage due to the thermal effect which can cause the formation of defects on the surface which trap additional energy causing an initial decrease in damage fluence and reaching saturation after a given number of pulses, as shown by Wang [10] for sapphire in air and with 150 fs 775 nm source lasers (see Figure7.2).

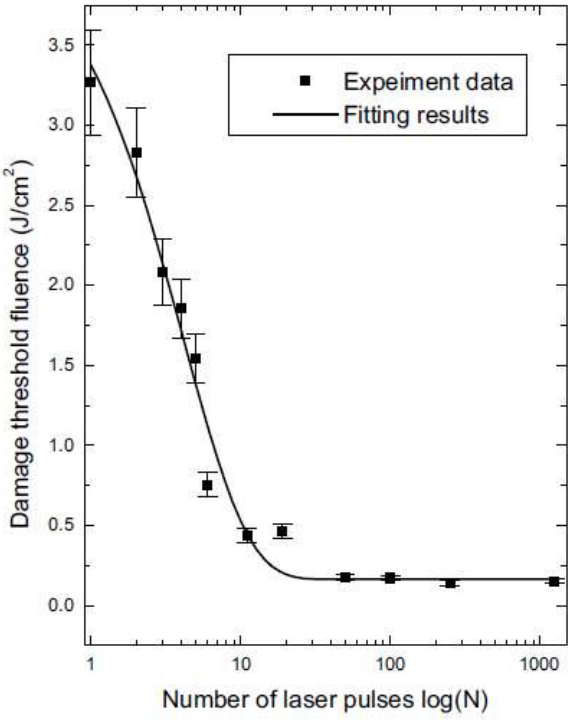

Figure 7.2: Damage fluence of a sapphire sample for different number of pulses at the same position in semi-logarithmic scale. Adapted from [10].

7.2 Basic of fiber coupling efficiency

Coupling light into a multimode optical fiber can be calculated by the overlapping integral between the fiber mode Ψ_b and the laser beam Ψ_F [11]:

$$\eta = \frac{\left| \int\int \Psi_b(x,y)\Psi_F^*(x,y)dxdy \right|^2}{\int\int \left|\Psi_b(x,y)\right|^2 dxdy \int\int \left|\Psi_F(x,y)\right|^2 dxdy} \tag{7.3}$$

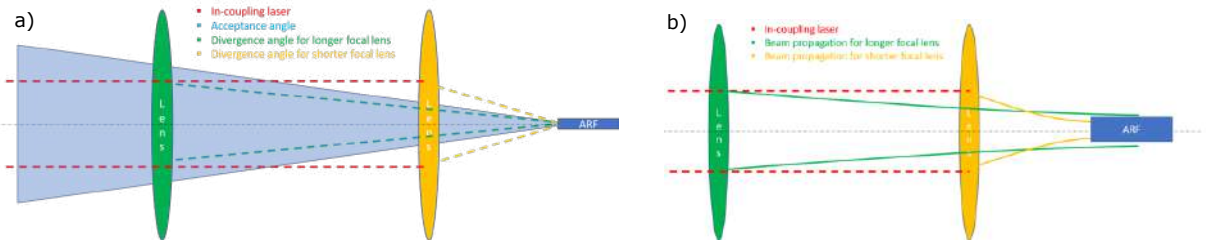

Figure 7.3: Coupling efficiency dependencies: To optimize the coupling into a hollow core fiber is needed to match (a) the acceptance angle and (b) the fiber core diameter with the beam divergence and beam waist, respectively. The sketch is not in scale and shows the aforementioned parameters for focusing lens with different focal distance.

Figure 7.3a) and b) show the parameters to be matched raising the coupling efficiency. From a geometric optics point of view, laser beam will be efficiently coupled into the fiber if the light

enters the core entirely with an incident angle θ smaller than the fiber acceptance angle θ_{acc}, reading to [141]:

$$\eta = \left(1 - e^{-\frac{2r\theta_{acc}}{w\theta}}\right)^2 \tag{7.4}$$

where r and w are the fiber radius and the laser beam size, respectively.

The acceptance angle is defined as the maximum angle of a ray w.r.t. the fiber axis over which the light can be guided by the core:

$$\theta_{acc} = \arcsin\left(\frac{1}{n_0} NA\right) \tag{7.5}$$

where n_0 is the refractive index of the medium around the fiber (=1 for air) and NA is the numerical aperture which depends on the fiber properties and, for an hollow core fiber, is given by [142]:

$$NA = \frac{1}{\sqrt{1 + \frac{\pi A_{eff}}{\lambda^2}}} \tag{7.6}$$

While λ is the incident laser beam wavelength, A_{eff} is the effective area indicating the transverse cross-section over which the total radiation propagates. For a sake of completeness, it needs to

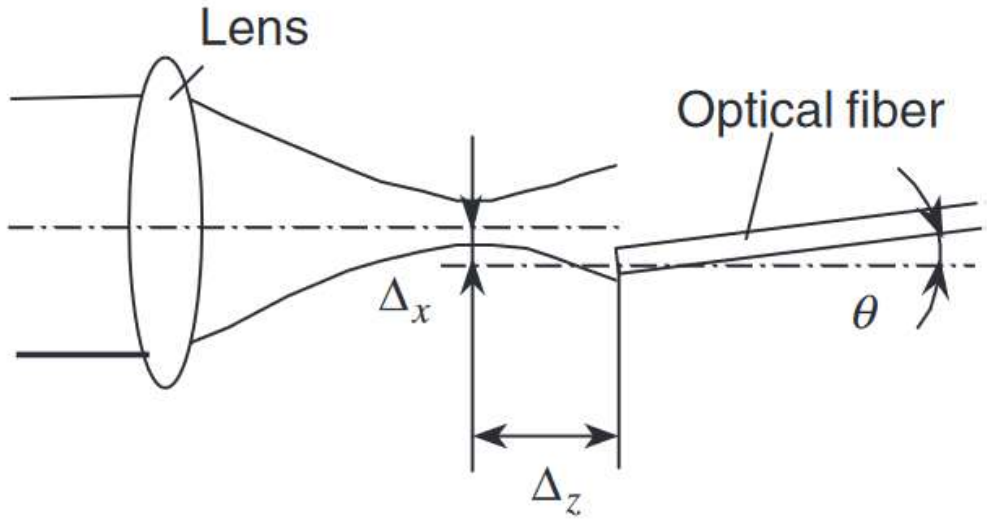

Figure 7.4: Fiber-laser beam misalignments: defocus Δz, lateral displacements Δx and Δy, and tilt angle θ. Adapted from [11].

be mentioned that a phase mismatch between the incoupling laser beam mode and the fiber mode will lead to a zero efficiency coupling [141]. Finally, Kataoka in his paper [11] calculates the coupling efficiency by Near-Field Method pointing out the effect of setup misalignments. Assuming longitudinal defocusing Δz, transversal displacements Δx and Δy, a tilt angle θ between the laser and the fiber axis (see Figure7.4 for details), the coupling efficiency reads as:

$$\eta = \eta_x \eta_y \eta_\theta \tag{7.7}$$

The defocus contribution is included into the lateral displacements coupling factors η_x and η_y. Transverse misalignment may be extremely detrimental in fundamental mode coupling as it could

introduce higher order modes [136].

Wu [143] demonstrated that for an ARF, the only contribution to material absorption is due to the distribution of the electric field inside the cladding. For PBGs carrying the fundamental mode, only 0.2% of energy propagates in the dielectric, making them, together with other hollow core fibers, very attractive for very high power laser propagation unlike solid core fibers where all the energy is concentrated in the dielectric, lowering the damage fluence [144]. Michaille et al. [145] showed that the damage threshold power of an air core is $\approx$ 25 times greater than for an equivalent solid core and also they demonstrated $\approx$95% of input laser coupling into the fundamental mode for a PBG pointing out the Gaussian nature of the fundamental mode. It is clear that other modes will have less coupling due to the different topology.

For a hollow core fiber, the damage also occurs due to other non-linear effects such as self-focusing, two-photon absorption, photoionization of the filled-gas [127] and optical discharge (OD). The latter propagating through the entire fiber in the direction of the source at a speed between 1m/s and 1 km/s could destroy it irreparably (hence the name 'destructive wave') [146, 147]. The effect of OD on hollow cores is less than on solid core fibers simply because the density of the gas filling the core is several orders of magnitude lower than inside solid core fibers. This observation is of great interest for the application of an ARF in a beam line, where vacuum conditions are required, since in a vacuum environment OD may have less impact on the hollow cores allowing to increase the laser intensity.

In 2019, Bufetov et al. [147] showed that 6 ps pulses with intensity up to $1.5 \cdot 10^{12}\ W/cm^2$ can be propagated in a hollow core fiber at a distance of 1 m without OD. ACHIP laser with a peak power of 1 GW focused in an ARF of 80 μm of radius produces a maximum intensity of about $6 \cdot 10^{12}$ W/cm^2 which could therefore induce OD. The simulations carried out in this thesis work have been made considering this effect and for this reason the pulse energy was limited to 0.5 mJ which would produce an intensity of about $1 \cdot 10^{12}$ W/cm^2 resulting below the limit value. The assumption made therefore makes the obtained simulation results even more realistic for a future experiment.

7.3 Experimental setup

7.3.1 Ho:YLF Amplifier System

For ACHIP experiments at ARES, the DLA is driven by a 2 µm Ho:YLF laser amplifier system provided by F. X. Kaertner group and managed by H. Cankaya. In April 2019 the laser system has been transported from the CFEL to the SINBAD photo-cathode laser laboratory and re-aligned for delivering a $\approx$2 mJ pulse laser energy with 2 ps pulse duration to the experimental area. The output laser parameters are gathered in Table 7.1 while Figure7.5 a) shows the clean

Table 7.1: 2μm laser parameters

	Value
Wavelength [μm]	2.051
Pulse Duration [ps]	2.2
Beam Size [mm]	3.9 x 4.0
Rep.Rate [kHz]	1
Compr. Pulse energy [mJ]	2

room environment of laser laboratory which is equipped with temperature and humidity air system control. The laser system is based on the chirped pulse amplification technique which is detailed in ref.[148] while the design of the system can be found in ref.[149]; in the following an overview of the whole laser system will be presented.

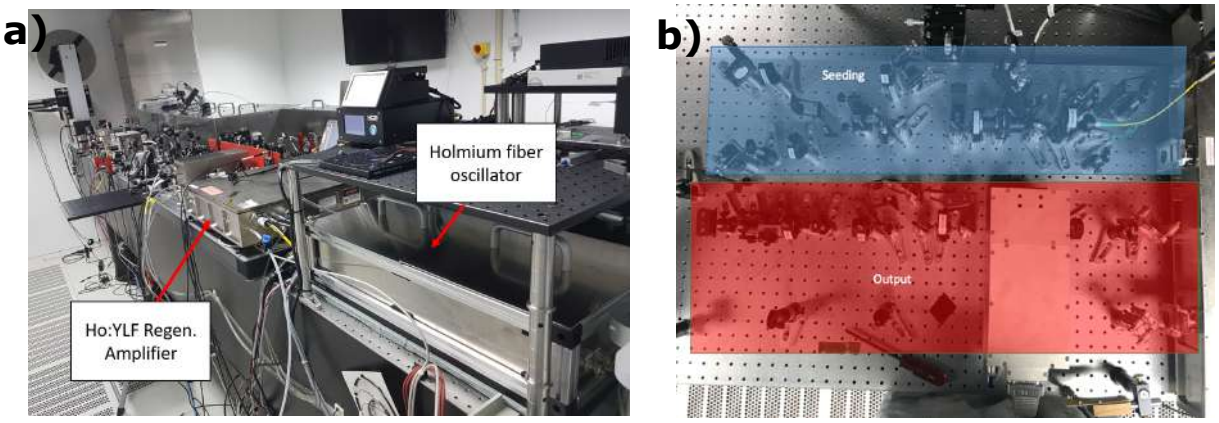

Figure 7.5: (a)A photograph of 2 μm laser amplifier system, (b) optical system for seeding and output

The near infrared laser system consists of a mode-locked homemade Homlium fiber laser oscillator which seeds a prototype Ho:YLF regenerative amplifier (RA) whose output signal is further amplified by a single-pass amplifier stage (SPA). The seeding and the output optical setup are shown in 7.5 b). Homlium fiber oscillator provides 95 pJ energy pulses and 1 ps pulse duraton at 41.6 MHz repetition rate [150]. This signal is stretched to ≈300 ps pulse duration by mean a chirped volume Bragg grating (CVBG) and injected into the amplifier system. As anticipated, the amplifier system is composed by RA and SPA which are both pumped by a continuous-wave (CW) 50 W Tm: pump laser. Figure 7.6 a-b show the efficiency curve of the amplifier system and the spectra for the stage with and without SPA.

The RA is a doped 40 mm long HY:YFL crystal delivering up to ≈700 μJ at 1 kHz repetition rate. The number of round trip (RT), which intrinsically defines the signal amplification, is fixed by a Pockels cell in combination with a quarter-wave plate (QWP) and a thin-film polarizer (TFP). This signal is subsequently amplified in the SPA stage which is a doped 70 mm long Ho:YFL crystal achieving a pulse energy up to ≈2 mJ. The output amplified signal is then injected into a Pockels cell-based pulse picker (see Figure 7.5 b)) in order to control and match the repetition rate to the ARES linac. Furthermore, it will give an opportunity to conduct a systematic damage study of the DLAs to explore the effect of accumulation of the pulses on damage mechanism. Finally, the pulses are compressed to ≈2 ps pulse duration using another CVBG which brings the laser system to the working parameters of Table7.1. This compressed pulses are characterized by an home-made second harmonic frequency resolved optical gating technique (FROG) and illustrated in Figure 7.7 a-d.

7.3.2 Tested fiber and experimental setup

The fiber used in this experiment was fabricated using the stack and drawn method described in the chapter 4, on behalf of the collaboration undertaken with Erlangen MPL. Figure 7.8 a) and table 7.2 show a sketch of the fiber cross section and the geometrical parameters, respectively. Unlikely the fiber used in the simulations of the previous chapter, the tested fiber has a smaller

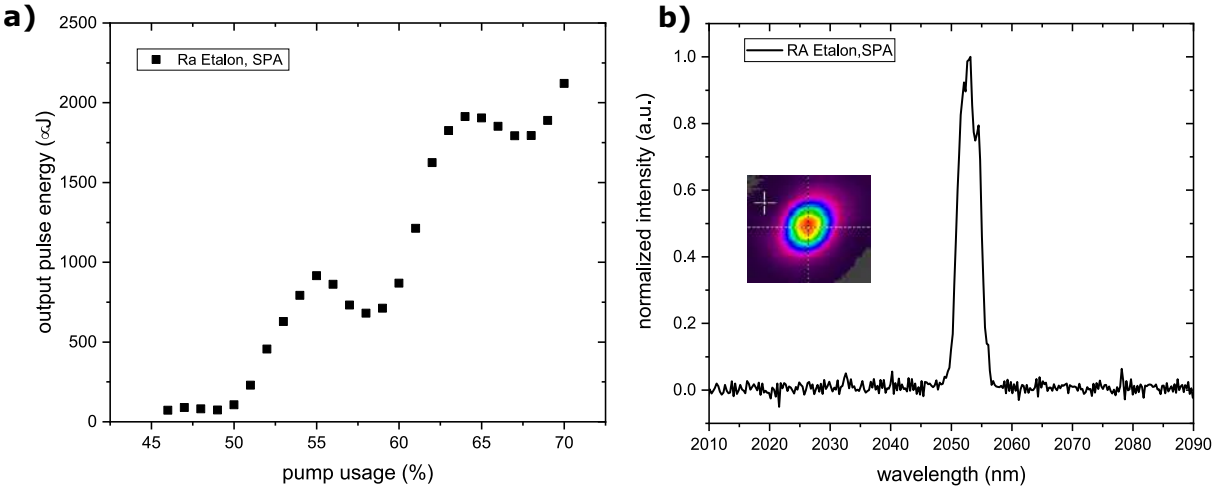

Figure 7.6: a) Output pulse energy of the amplifier system consistent of RA and SPA as a function of pump usage. b) Spectra of the pulses in the amplifier system.

Table 7.2: Tested ARF parameters

	Value
Core diameter [μm]	160
ARE diameter [μm]	85
ARE wall thickness [μm]	1
Number of AREs	6

number as well as thinner thickness of the capillaries. However, the COMSOL simulation based on the scanning electron microscope of the fiber cross-section shows a phase velocity ($\beta_{\text{tested}} - \beta_{\text{simulated}} \approx \mathcal{O}(10^{-6})$) and field intensity very close to those simulated in this work of thesis.

Figure 7.8 c)-d) show a schematic (along with a possible further optimization) of the setup and the implemented one for coupling and damage test experiments in the ARES laser lab. Two mirrors are used to align the delivered amplified pulsed signal to the ARF. On a three-dimensional micro-translational stage, the CaF lens is located focusing on the ARF which is supported by a Thorlabs V-grooves with adjustable fiber clamp placed on a three-axis micrometer stages. Finally, the Pyrocamera captures the beam after propagation through the fiber and/or a power meter detects the transmitted averaged power. The experiment could be optimized by using a telescope downstream the focusing lens in order to improve the coupling efficiency by tuning the laser beam size at focusing lens position, as discussed in the following section.

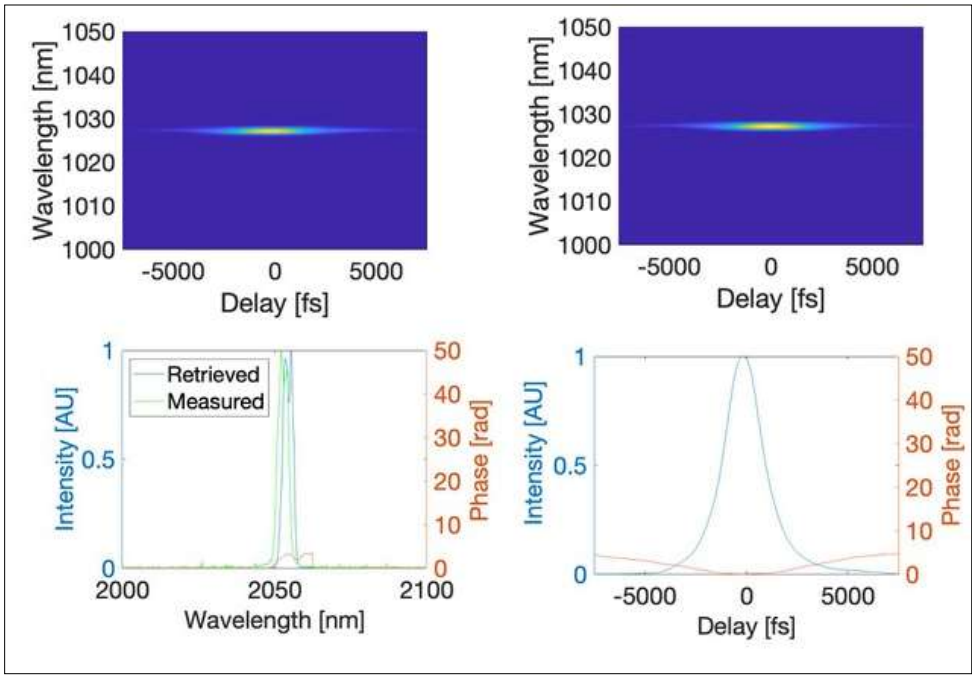

Figure 7.7: FROG analysis for the compressed pulse: On the top, the plots show the measured (left) and retrieved (right) FROG trace. On the bottom it is shown the measured and retrieved spectra of the pulse (left) and the temporal pulse profile (right). Courtesy of H. Cankaya

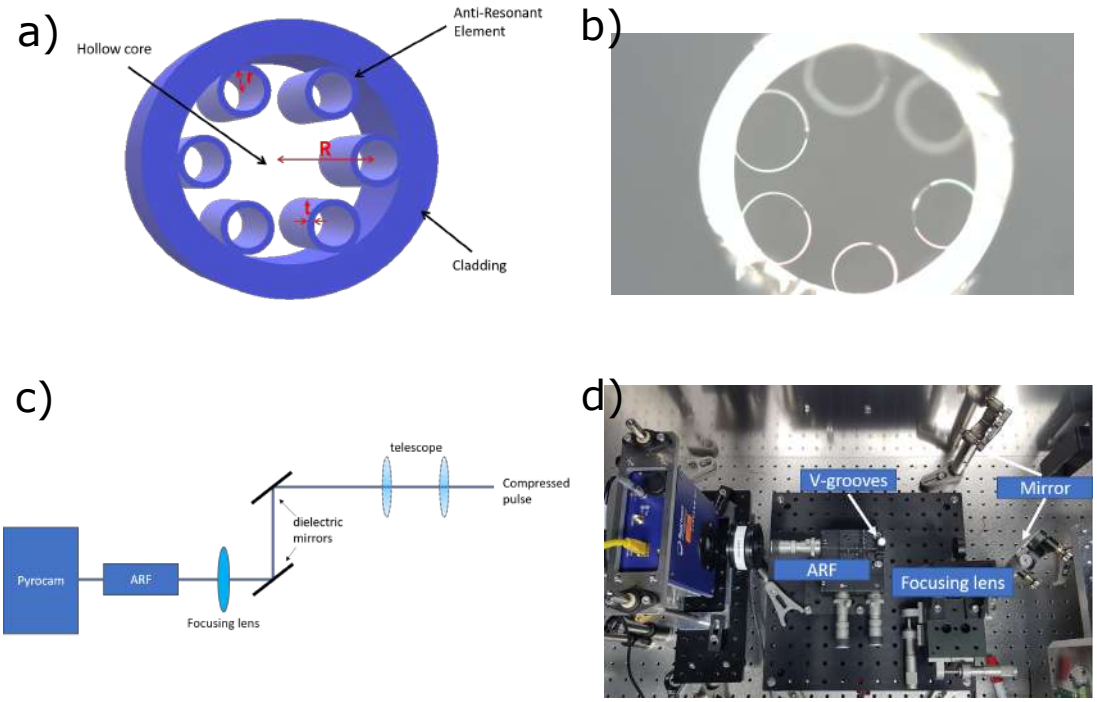

Figure 7.8: Experimental setup and tested fiber: a) Sketch of the used fiber and b) a picture from optical microscope (x20); c) schematic of the experimental setup: two dielectric coated mirrors deliver the compressed beam to a focusing lens focalizing the beam at ARF entrance while Pyrocam and/or power meter detect the transmitted beam. Also, a telescope can be located upstream. c) The implemented setup for coupling efficiency and damage threshold limit experiments.

7.4 Coupling efficiency and laser induced damage experiment

7.4.1 Cleaving of fiber and bending considerations

The fiber sample preparation plays an important role in the optimization of the coupling efficiency and the maximum power transmitted into the fiber without damage. When a laser beam should be launched into the fiber, cleaving is an important technique providing fiber ends as clean, flat and perpendicular to the axis as possible. Cleaving is a controlled breaking of the bare fiber which begins with making a scratch on one side of the fiber and ends with applying a tension to the fiber causing a break propagates from the fractured point to the full fiber cross section. Various fiber cleaver tools are currently being developed and range from the simplest and cheapest to much higher quality and more expensive techniques such as mechanical precision fiber cleavers which use a vibrating diamond blade to cause the required scratch for the breaking.

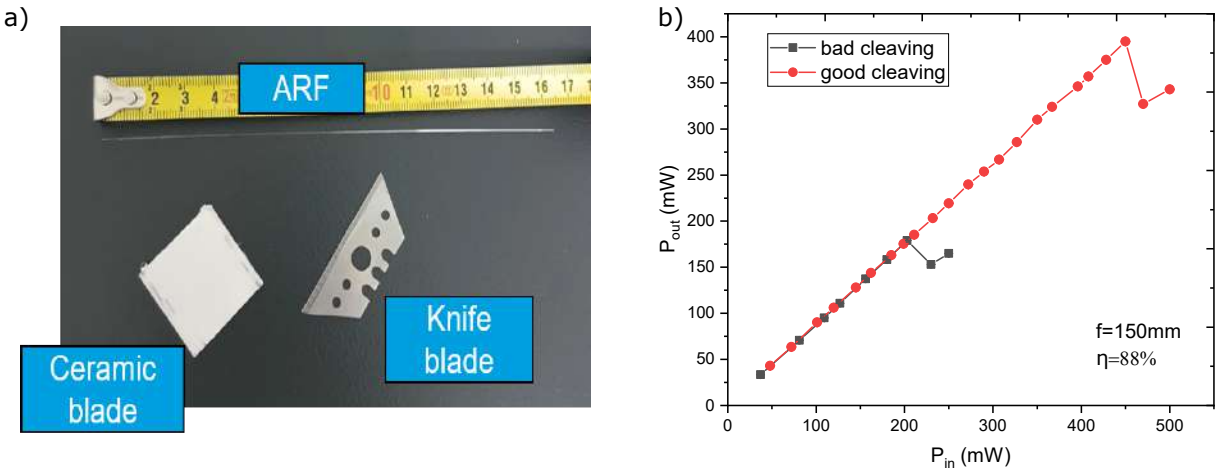

Figure 7.9: a)Cleaver fiber used in the preliminary test at ARES/SUNBAD laser lab along with a sample fiber; b) Output power as function of input power for two differently cleaving fibers: for the identical experimental setup parameters such as the focusing lens of 150 mm, the fiber with a better quality in the cleaving process supports higher incoupled power.

Before cleaving, fiber coating needs to be stripped off with,e.g., a slave blade leading to the bare fiber. On one side of the fiber, a scratch in the perpendicular direction of the fiber axis needs to be made with, e.g., ceramic thermal insulator "blade" (usually it is used a sharp diamond). Holding the fiber on one side and giving the other end a kick with a finger, the cleaver occurs. Figure 7.9 a) is a picture of the fiber cleaver used in this work along with a tested cleaved fiber. The experiment results may be dependent on the operator cleaving skill using such technique as showed in Figure7.9 b) where it is plotted the maximum transmitted power through two different cleaving fibers. Although the two fibers have the same coupling efficiency, the better-cleaving one can support more power before it is damaged. This effect may be due to the fact that for a surface not flat and/or not perpendicular to the fiber axis, the laser beam may unintentionally hit a part of the cladding generating damage at a lower power than for a better cleaving fiber where the beam has completely entered the fiber core and the damage is generated by an avalanche process triggered by the radiation inside the fiber.

Finally, the author would like to point out that, as this is a preliminary test with the aim of testing an ARF for the first time at ARES/SINBAD laser lab, the experimental setup is not

optimized. In fact, the fiber is subjected to uncontrolled bending since it is supported only on one end by V-grooves, as shown in the Figure7.8c). Considering a fiber diameter D and a λ laser beam wavelength, the presence of a bending introduces a bend loss becoming significant as a critical bending radius value, which scales as $R_{cr} \approx \frac{D^3}{\lambda^2}$, is reached [104]. Due to the curvature($R < R_{cr}$), the light can couple from the core mode to the capillary mode resulting into a slightly less coupling efficiency of the fundamental mode. However, by using fibers of the same length it is plausible to assume that all the tested fibers are affected by the same bend loss, and therefore the coupling efficiency will be decreased and suffer from the same systematic error making the results of the tests described below comparable.

7.4.2 Results

The experiment purpose is to test for the first time an ARF at ARES/SINBAD laser lab carrying out first coupling efficiency and power threshold. As discussed above, the coupling efficiency strongly depends on the matching between the beam divergence and fiber acceptance angle, as well as the beam size at the fiber entrance.

By mean the cleaving fiber technique describes above, 16 cm as fiber length has been cut. As the laser is assumed to be a collimated beam, the beam size at focusing lens position is considered constant. Under this ansatz, by the micrometer translation stage the focusing lens position has been changed w.r.t. the fiber entrance. As foreseen from eq.7.7, the coupling efficiency shows a maximum achieved value as the longitudinal misalignment is zero i.e. at beam waist position, as shown in Figure7.10 a). Since the beam size at waist is minimum it can better match the fiber core increasing the efficiency, here defined as the ratio of the coupled transmitted power P_{out} and the incoupling P_{in} power. It is known that lens with weaker focus strength, i.e. longer

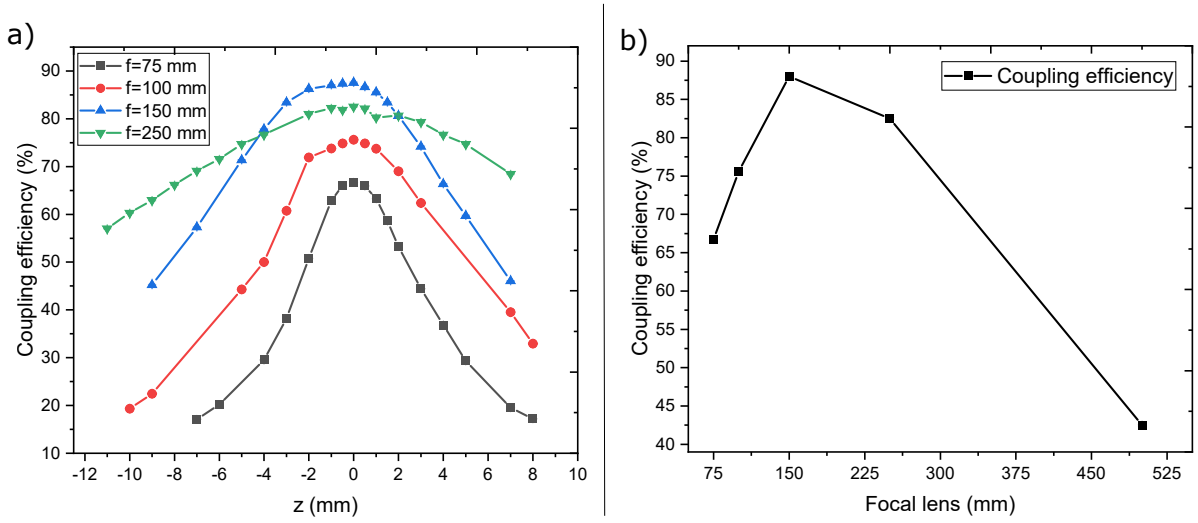

Figure 7.10: Coupling efficiency: a) efficiency reaches the maximum value at the waist position while decreases for defocus positions; b) maximum efficiency for the used focusing lens adding a longer one with f=500 mm.

focus position, will bring a more relaxed divergence, viceversa the shorter focus distance the bigger divergence angle. Figure 7.10a)- b) show the maximum coupling efficiency for different focusing lenses whereas the results are gathered in Table 7.3. In this preliminary coupling test a maximum value of $(87.5 \pm 0.1)\%$ was achieved for a 150 mm as focusing lens. The second

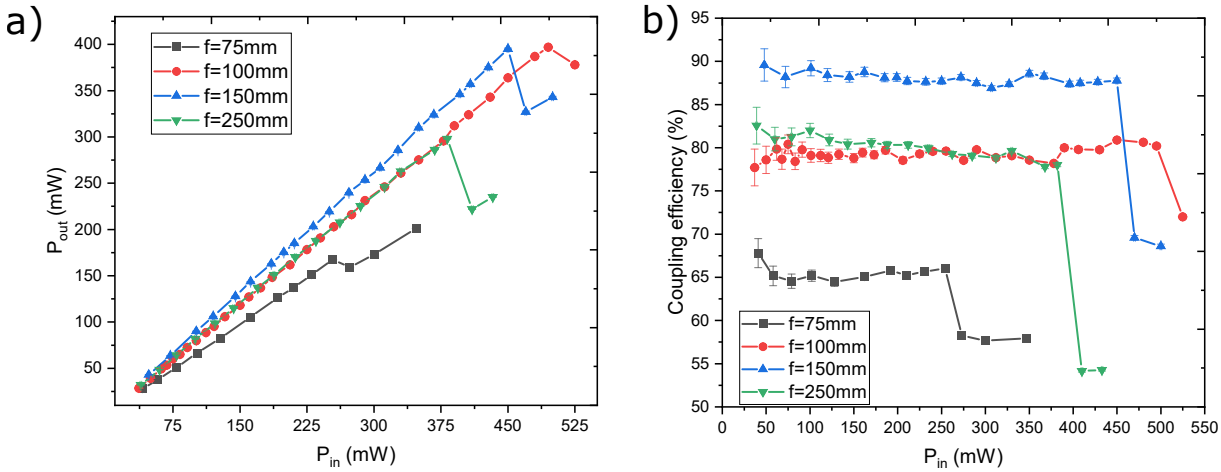

Figure 7.11: a)Measured transmitted power and b) coupling efficiency as function of the measured incoupled signal. Transmitted power increases linearly until damage occurs leading to an irreversible drop into the efficiency.

part of the experiment was to measure the maximum incoupling power supported by the fiber before damage occurs. Figure 7.11 a) shows the transmitted power as function of the input power for different focusing lens. The linear trend drops suddenly as the damage occurs into the fiber leading to a drastically decrease of the coupling efficiency as shown in Figure 7.11 b). Maximum incoupling power results are summarized in Table7.3. The damage is an irreversible effect: as the fiber gets damage the coupling irreversibly drops to much lower value. It is clear that better coupling corresponds to an increase in the incoupling supported power. In particular, for a 150 mm focal lens and $\approx 88\%$ efficiency a maximum incoupling power of (450 ± 1) mW is reached. The maximum pulse energy supported by the fiber is thus estimated to be around ≈ 0.45 mJ which is very close to the 0.5 mJ manufacturer's suggested value. The discrepancy may be due to the experimental environment and sample preparation. In view of a future experiment at ARES/SINBAD, a properly well-designed setup needs to be implemented in order to catch up the manufacturer's supported energy value.

Table 7.3: Coupling efficiency and damage test results

focal lens [mm]	η[%]	max incoupling power [mW]	Fluence[J/cm^2]
75	66.7±0.1	254.1±0.1	2.08±0.05
100	75.6±0.1	495±1	2.28±0.06
150	87.5±0.1	450±1	0.92±0.03
250	82.5±0.1	382±1	0.281±0.008
500	42.5±0.1	–	–

As already mentioned at beginning of the chapter, an usual quantity to characterize the damage is the damage fluence, i.e. the energy for irradiated area $F[J/cm^2] = Energy/Area$. For that reason, a spot size value as precise as possible is an important requirement. Assuming an ideal gaussian, M^2=1, in paraxial approximation and negligible aberrations, the beam waist as function of the used focusing lens f can be calculated by:

$$w_0 = \frac{M^2 \lambda f}{\pi w}, \tag{7.8}$$

where w is the beam size at focusing lens position. Figure 7.12 shows the calculated damage fluence for the experimental used lens carrying out a maximum of $\approx 2J/cm^2$ as damage fluence for the tested ARF. Calculated fluence and the other experimental results of this works are summarized in Table 7.3.

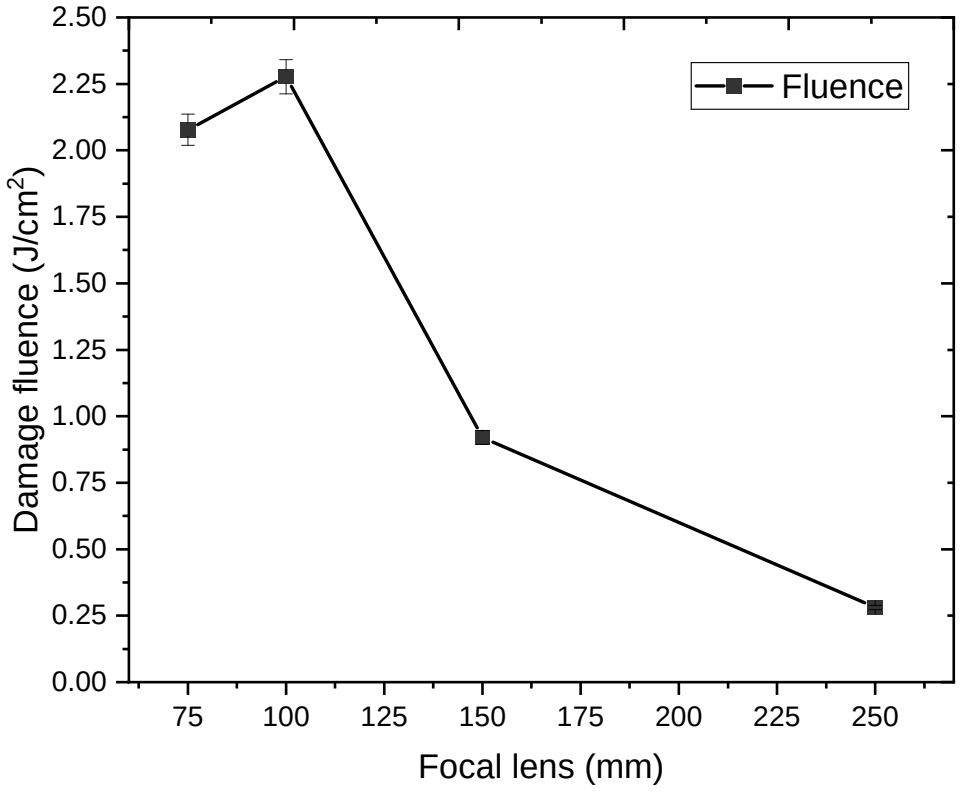

Figure 7.12: Fluence for different focusing lenses reaching a maximum of ≈ 2.3 J/cm^2 at f=100mm.

7.4.2.1 M-squared measurements by knife-edge method

In order to estimate the spot size but also in view of a future experiment aiming to evaluate the fluence of different materials, a setup for the measurement of M^2 was implemented. This experiment has been performed before the upgrade of the laser system and thus before the ARF coupling/damage tests. Here the seeding laser was a Menlo System oscillator which provided 10 nJ pulses with 10 MHz as repetition rate. The seeding signal was then streaked by the CVBG, amplified by the Ho:YFL regenerative amplifier, and compressed to 1.6 ps pulse duration.

The beam propagation factor M^2 is a figure of merit for the quality of the laser system. It compares the shape of the beam laser with the ideal gaussian beam and in case the beam matches exactly the Gaussian shape, M^2 is equal to 1. In the real beam this parameter is greater than

the 1 as the laser beam has worse quality than the ideal Gaussian beam. M^2 is usually given by:

$$M^2 = \frac{\pi w_0 \theta}{\lambda} = \frac{\pi w_0^2}{\lambda z_R} \tag{7.9}$$

where w_0 is the beam waist, λ is the wavelength, θ is the beam divergence and z_R is the Rayleigh lenght (distance from the beam waist where the beam radius is increased by a factor $\sqrt{2}$. The usual method used for M^2 measurements is knife-edge techniques. The sketch and the implemented setup hosted in the photocathode laser lab are shown in Figure7.13.

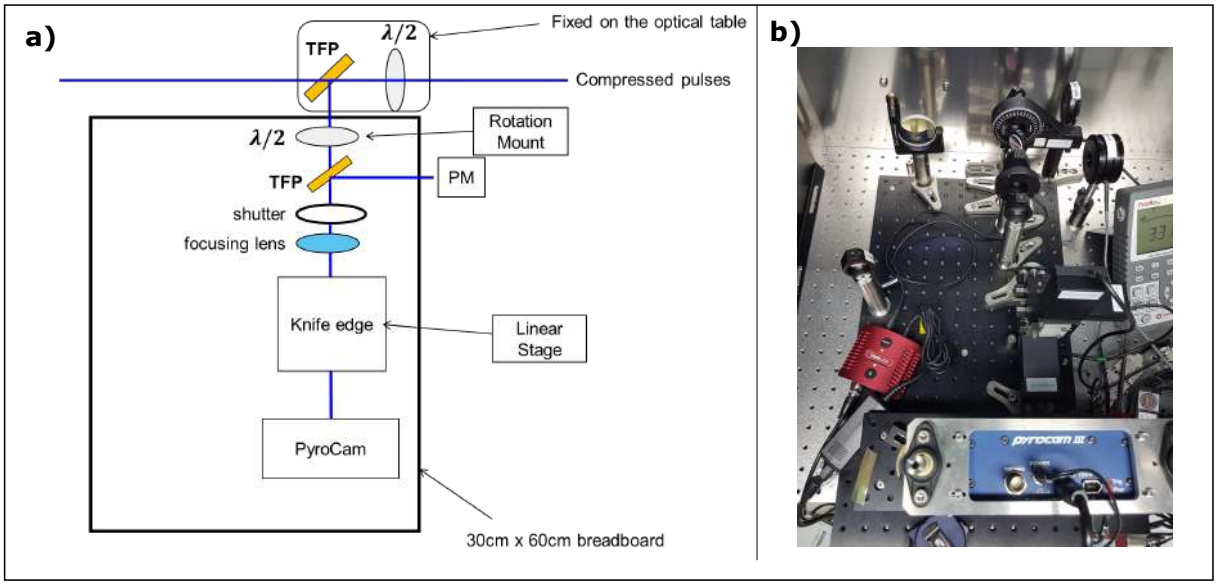

Figure 7.13: a)M^2 setup sketch and b) implemented setup used for measurements.

As shown in Figure7.13a) 2μm laser from the Ho:YLF amplifier is delivered to the 60 mm x 30 mm breadboard by the combination of a half-wave plate (WP) and a thin film polarized (TFP). The whole setup is as much compact as possible due to space constrains in the lab. The measure has been automatized by LabVIEW software (implemented by another colleague [37]) which controls the linear stages and a DAQ system. A half wave plate on a motorized rotational mount combined with a TFP works as a beam splitter to control the pulse energy delivered to the linear motorized translational stage which can be adapted to support the razor blade. Upstream the linear stage is located a coated CaF lens for beam focusing while downstream the Pyrocamera monitors the beam. Finally, shutter located between the beam-splitter and the focusing lens is used for controlling the exposure time and thus the number of laser pulses.

The implemented experimental setup is shown in Figure7.13 b). The beam is focused by 150 mm focusing lens and the knife edge on the linear translational stage covers step by step the beam a variable longitudinal position from the waist. The transmitted beam is captured by the Pyrocam which gives the total transmitted power. The acquired data are fitted to the error function of a Gaussian distribution:

$$P = P_0 + \frac{P_{max}}{2}\Big(1 - erf\big(\frac{\sqrt{2}(x - x_0)}{w}\big)\Big) \tag{7.10}$$

where P_0 and P_{max} are the background and the maximal power, respectively, and x_0 is a position

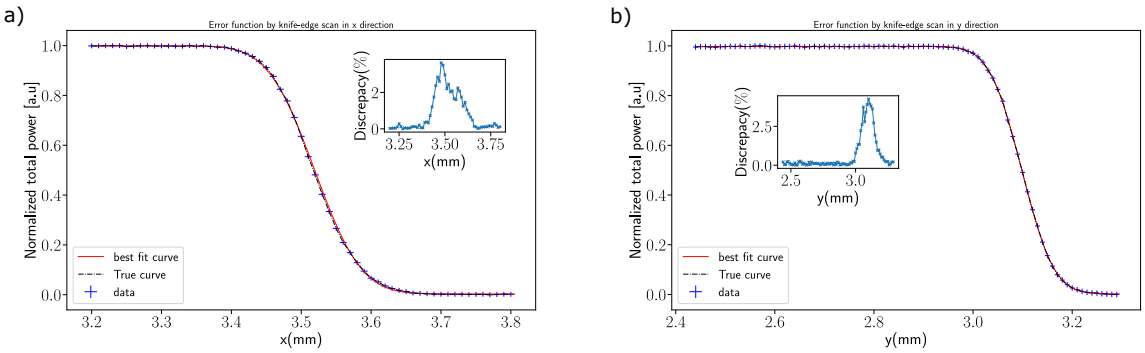

Figure 7.14: Example of a normalized total power scanning a)x- and b) y- direction for a fixed longitudinal position. The inserts show the discrepancy of the experimental data w.r.t. the fitted ideal function 7.10.

of shift with the half of real power. Figure7.14a) shows the fit of data for a fixed z position using the eq.7.10 from which one obtains a value of the beam radius w. This procedure is repeated changing the longitudinal position z.

For the calculation of the waist w_0 and its position on the longitudinal stage z_0, and Rayleigh length z_R, the obtained data have been fitted by:

$$w = w_0 \sqrt{1 + \left(\frac{z - z_0}{z_R}\right)^2} \tag{7.11}$$

while Figure 7.15 shows the beam evolution for the both transverse beam directions.

Finally, M^2 values are calculated by eq.7.9 providing a mean value $M^2 = 1.12 \pm 0.01$ and beam waist $w_{0x} = 55.1 \pm 0.3$ and $w_{0y} = 55.5 \pm 0.3$. All the results of this experiment are gathered in Table7.4 below:

Table 7.4: M-squared results

Parameter	x-direction	y-direction
w_0 [μm]	55.1±0.3	55.5±0.3
z_R [mm]	4.1±0.1	4.2±0.2
M^2	1.131±0.001	1.117±0.001

The results show that the implemented setup can be used for knife-edge measurements providing M^2 and beam size. Thus, the setup may measure the current laser beam parameters in order to provide precise values for the beam spot. It should be noted that the difference in the waist position for the different scan direction is mainly due to aberration which comes from the slight lenses and mirror misalignment in the whole setup, i.e. from the seeding laser, amplifier and damage test setup.

7.4.3 Further remarks

From the Gaussian beam propagation theory, beam waist and beam divergence are given by:

$$\begin{cases} w_0 = \frac{2M^2\lambda f}{\pi D} \\ \theta = \frac{M^2\lambda}{\pi w_0} \Rightarrow \theta = \frac{D}{2f} \end{cases}$$

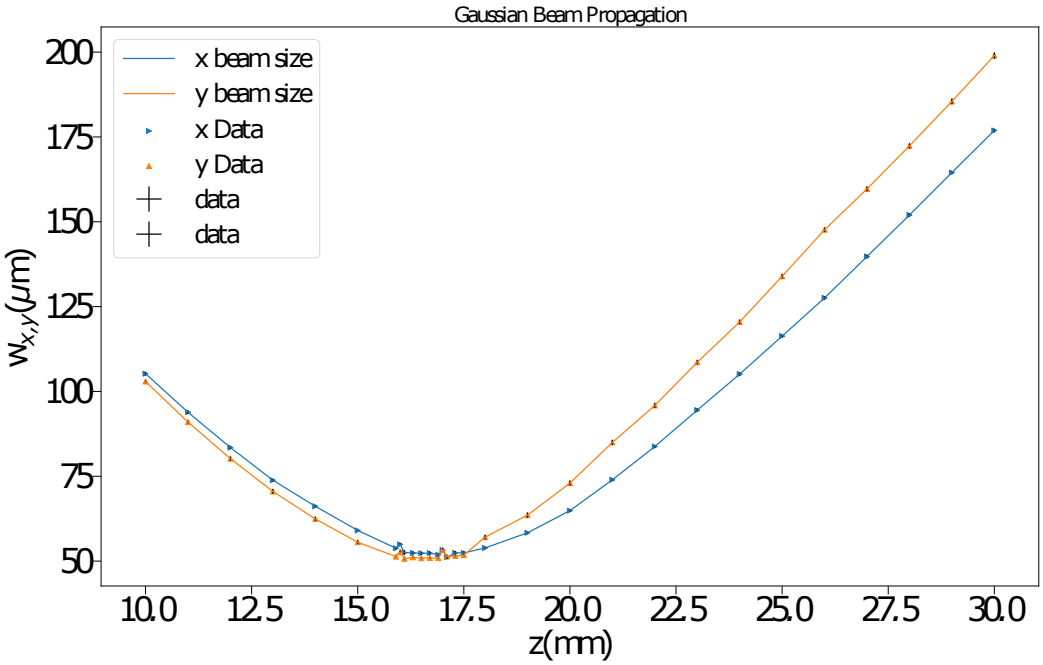

Figure 7.15: Gaussian beam parabola envelope for both transverse direction x and y. Data has been acquired with a shorter step around the waist in order to limit the uncertainty.

Figure 7.16 shows the beam waist and the divergence evolution as function of the focusing lens, along with their values for the experimental used lens (dot). It is clear that there is a tradeoff between these two parameters: increasing the focal distance the divergence angle decreases reaching value below the acceptance angle θ_{acc}, but at same time the beam waist increases exceeding the core radius value. The optimization of these parameters may therefore be necessary to further increase the efficiency. For this reason the implementation of a telescope before the focusing lens (as shown on the sketch in Figure 7.8) which changes the beam size D at focusing lens position could allow to further increase the coupling efficiency and therefore the maximum supported power.

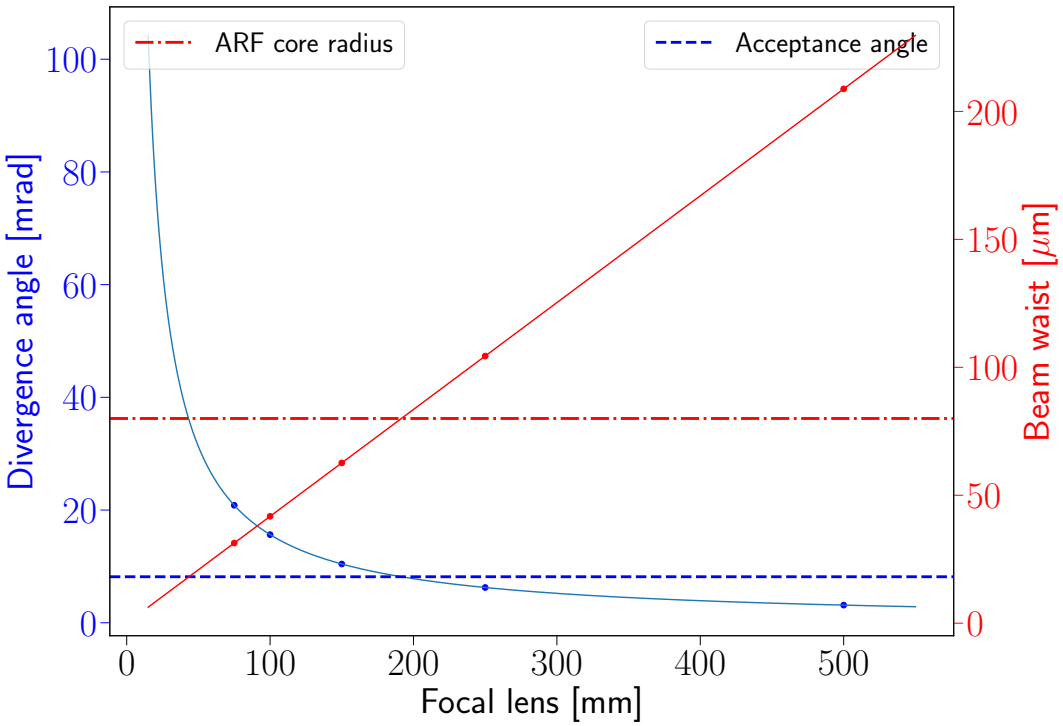

Figure 7.16: Tradeoff between the beam divergence and waist. For coupling efficiency optimization, a compromise for the two parameters needs to be achieved in order that the beam waist and the divergence are below the fiber core and acceptance angle, respectively. Finally, experimental values for the used lenses are shown (dots).

7.5 Conclusion

After the moving of the 2 μm laser system from the CFEL to the ARES/SINBAD photocathode laser laboratory, alignment and recommissioning has been performed. A setup for the M^2 measurements by knife-edge method has been implemented and tested. After the upgrade of the seeding oscillator, a preliminary coupling and damage test of an ARF at ARES/SINBAD laser laboratory has been performed showing that the tested fiber is suitable for the 2 μm laser wavelength. Furthermore, the cleaving method and the experimental setup are able to confine and propagate the laser through the fiber with a coupling efficiency of $\approx 88\%$. Although the obtained efficiency and maximum supported power values are slightly below the manufacturer's limit, the experimental results can be improved into the next experimental campaign. By employing a telescope and high-quality fiber cleavers, the coupling efficiency may reach the above 95% value while increasing the maximum propagating power through the fiber before the damage occurs.

Finally, the automatized setup used for beam propagation factor M^2 estimation could be used for the characterization of the upgraded laser system as well as for the measurement of damage fluence for different materials. The lack of literature for wavelength into the MIR range and the possibility to tune the repetition rate by means pulse picker makes this experiment attractive in the next future.

8

Conclusions and Outlook

Modern accelerators are mainly based on radio-frequency technologies which limit the maximum achievable acceleration gradient to $\mathcal{O}(100$ MV/m). The utilization of laser in the accelerator allows for higher gradients. Plasma-based accelerators are one of the advanced concepts able to provide accelerating field intensity in the order of GV/m. However, Joule-laser systems at lower repetition rates (up to few kHz) are required to achieve high gradients while spoiling the final beam quality, e.g. energy spread and beam divergence. A huge amount of work has been made to fill-in this promising accelerator concept and to overcome the related challenges. Laser-driven optical structures are another candidate for future compact accelerators. These structures are able to support at least one order of magnitude more than metallic cavities due to the higher damage threshold. Modern conventional laser systems routinely produce µJ pulsed energy at high repetition rate (up to MHz) and are used to power dielectric structures.

Laser-driven dielectric grating structures can support $\approx$ GV/m gradient but the evanescent fields inside the µm aperture limit the interaction path due to the spoiling of the beam quality. Ideally, a PBG fiber may confine the light into the core with few db/km as losses enabling meter-scale acceleration channel. For fixed lattice period, capillaries and hollow core radius, six-hold symmetry PBG fiber supports synchronous TM_{01}-like mode. Since the size of the core is comparable with the driven-wavelength, the manufacturing runs at the edge of the modern fabrication techniques. Thus, imperfections need to be considered motivating the tolerance study which has been performed in this work of thesis. A linear trend among the phase velocity of the mode and geometrical parameters changes has been shown pointing out that the core radius affects mode properties more than the others.

However, laser-driven the pulse length limits the interaction path to 0.5 m while the number of layers of capillaries surrounding the core can improve the light confinements reducing the losses. The trade-off between the loss coefficient and the quality factor in such a fiber is a crucial behavior to handle to increase the confined power. As the number of layers increases the loss coefficient decreases exponentially leading to a longer accelerating channel. Likewise, the quality factor of the coupled mode increases exponentially too. As the bandwidth of the mode is inverse proportional to the quality factor, it will decrease exponentially. This trend leads to the conclusion that for an efficient acceleration in a photonic bandgap fiber, ns-pulse laser system is required.

The current status of the 2 µm ARES/SINBAD laser system would provide ps pulse duration leading to a 70 % of incoupled power loss using 1 mm Lin-fiber with 6 layers. An upgrade of the laser system may be a valid solution to this limitation. An optical parametric amplifier (OPA)

could be installed to provide ns tunable wavelength pulses. Also, current commercial laser can provide the required laser beam parameters but the costs for a preliminary photonic crystal fiber experimental campaign at SINBAD/ARES would be challenging. Furthermore, synchronous accelerating mode propagates into PBG fiber with hollow core radius value comparable to the driven wavelength which for the optical regime requires an aperture $\mathcal{O}(\mu m)$ making both the fabrication of the fiber and the electron beam parameters very challenging to achieve.

Alternatively, the larger hollow-core anti-resonant fiber (ARF) consists of only a single ring of anti-resonant elements (capillaries) surrounding the core. The easier geometry and the larger aperture compared to the Lin-fiber makes both fabrication and the application to the modern electron beam technologies more suitable. Being a multimode fiber, it can support several asynchronous modes. Phase velocity of the modes exceeds the speed of light limiting the interaction path between the driven mode and the ultra-relativistic electron beam to mm-scale due to the phase slippage. In this work of thesis we have been particularly interested in the accelerating TM_{01} and the fundamental deflecting HE_{11} modes. We have investigate the application of laser driven TM_{01} and HE_{11} modes onto relatively short and long bunches. From damage threshold considerations based on SINBAD/ARES laser system, the fiber can support an accelerating gradient up to 180 MV/m. Limiting the interaction of a short ultra-relativistic electron bunch to the portion of the sinusoidal modes over which net energy gain is provided by the modes, the beam gains almost 1 MeV as energy over 8 mm of fiber length while maintaining the initial beam quality e.g. energy spread and emittance. Although the results are promising, there is at the moment no method to properly synchronize an electron bunch into such an injection phase. Synchronization between an externally injected electron bunch and optical acceleration structure is challenging. Due to the synchronization capability, the investigation of long bunches is more appealing. In such an experiment, the full range of phases would be sampled by the injected bunch.

Modern concepts of electron beam manipulation rely on interaction of the electron beam inside a laser-driven undulator providing energy modulation. Modulated beam is then injected into a magnetic chicane resulting into microbunch trains. This scheme is foreseen to be installed at ARES/SINBAD experimental area in the behalf of the Accelerator on a Chip International Project (ACHIP). In this thesis we have proposed a novel scheme for energy modulation based on the combination of ARF, collimator and dispersive section. For a simpler scheme composed of just 6 mm ARF driven by TM_{01} mode far from the damage threshold limitation (e.g. $E_z \approx 10 MV/m$), a peak-to-peak energy modulation of ≈250 KeV has been simulated. Furthermore, increasing the field strength inside the fiber up to the damage threshold produces microbunch train. Longer electron bunch (σ_t=20 fs) experiences transverse forces amplitude varying with the relative phase. For certain phases, portions of the electron beam are defocused leading to a microbunch train production by geometrical effect. The spoiled electrons are then removed by a collimator producing microbunched beam at the driving wavelength. Using a dispersive section, the correlated energy spread of the beam can be converted into density modulation resulting into the prodcution of ≈ 100 attosecond FWHM microbunch trains with the periodicity of the driving wavelength. A bunch form factor of ≈0.6 is calculated at the fundamental harmonic with a peak current of 50 Amps. We expect the simple technique to have applications for beam manipulation and radiation generation. As the simulated beam parameters are achievable at ARES/SINBAD experimental area, a first proof-of-principle experiments could be performed by small changes of the hexapod base-plate in the experimental chamber. Discussion on the coupling of the optical laser to the ARF while injecting electron beam is already ongoing and may foresee the utilization

of a holed off-axis paraxial mirror.

In this thesis, we also have discussed how the deflecting HE_{11} mode could be employed. In conventional accelerators, the deflecting mode is used for longitudinal bunch diagnostic enabling measurement of bunch length and longitudinal phase space when combined with a spectrometer. A short bunch (σ_t=1 fs) properly injected into the ARF driven by deflecting mode will be streaked on a screen located downstream. Simulations show that ARF can be used for bunch length measurements with sub-attosecond resolution. Such a powerful diagnostic could be used to provide information on complex process in X-ray free electron lasers. The effect of edge fields in the coupling process is not discussed in this thesis and could be the topics for future investigations. Finite-different time-domain software such as VSIM or CST could be used for further investigations. Also, ARF could be an interesting topic for the investigation of radiation generation. High charged beam travelling through the ARF hollow core could produce high intensity wakefield motivating investigation in such an application.

Finally, the laser induced damage threshold limits the maximum achievable gradient in the ARF. In the SINBAD/ARES laser laboratory, we implemented an optical experimental setup to perform a preliminary coupling efficiency and damage threshold measurements. Our results show a coupling efficiency of ≈ 88 % while a maximum laser pulse energy of 0.45 mJ is injected. These measurements will be particularly important at ARES/SINBAD for performing first beam manipulation experiments as they set rough limitations for this fiber.

Summarizing, in this thesis we proposed a novel scheme for beam manipulation using a laser-driven anti-resonant fiber. We investigated the accelerating and the deflecting modes interaction with an ultra-relativistic energy beam demonstrating energy modulation, microbunch trains production and possible bunch length measurements with sub-attosecond time resolution. These results are very promising and motivate further investigations and first experimental campaign at SINBAD/ARES for a laser-driven ARF.

References

[1] E. Panofski, et al. Commissioning results and electron beam characterization at the s-band photoinjector at sinbad-ares, 2021.

[2] K. Wille. *The physics of particle accelerators: An introduction*. 2000.

[3] S. Di Mitri. Bunch Length Compressors. *CERN Yellow Rep. School Proc.*, 1:363, 2018.

[4] P. Russell. Photonic crystal fibers. *Science*, 299(5605):358–362, 2003.

[5] C. Markos, et al. Hybrid photonic-crystal fiber. *Rev. Mod. Phys.*, 89:045003, Nov 2017.

[6] C. R. F., et al. Single-mode photonic band gap guidance of light in air. *Science*, 285(5433):1537–1539, 1999.

[7] D. M. Chow, et al. Fabrication of photonic crystal fibers. In *2012 IEEE 3rd International Conference on Photonics*, pages 227–230, 2012.

[8] B. C. Stuart, et al. Nanosecond-to-femtosecond laser-induced breakdown in dielectrics. *Phys. Rev. B*, 53:1749–1761, Jan 1996.

[9] K. Soong, et al. Laser damage threshold measurements of optical materials for direct laser accelerators. *AIP Conference Proceedings*, 1507(1):511–515, 2012.

[10] X. Wang, et al. Femtosecond pulse laser ablation of sapphire in ambient air. *Applied Surface Science*, 228(1):221–226, 2004.

[11] K. Kataoka. Estimation of coupling efficiency of optical fiber by far-field method. *Optical Review - OPT REV*, 17:476–480, 09 2010.

[12] W. P. Leemans, et al. Multi-gev electron beams from capillary-discharge-guided subpetawatt laser pulses in the self-trapping regime. *Phys. Rev. Lett.*, 113:245002, Dec 2014.

[13] E. Peralta, et al. Demonstration of electron acceleration in a laser-driven dielectric microstructure. *Nature*, Nov 2013.

[14] J. Breuer and P. Hommelhoff. Laser-based acceleration of nonrelativistic electrons at a dielectric structure. *Phys. Rev. Lett.*, 111:134803, Sep 2013.

[15] D. Cesar, et al. Enhanced energy gain in a dielectric laser accelerator using a tilted pulse front laser. *Opt. Express*, 26(22):29216–29224, Oct 2018.

[16] F. Mayet. *Acceleration and Phase Space Manipulation of Relativistic Electron Beams in Nano- and Micrometer-Scale Dielectric Structures.* Dissertation, Universität Hamburg, Hamburg, 2019. Dissertation, Universität Hamburg, 2019.

[17] X. E. Lin. Photonic band gap fiber accelerator. *Phys. Rev. ST Accel. Beams*, 4:051301, May 2001.

[18] F. Benabid, et al. Stimulated raman scattering in hydrogen-filled hollow-core photonic crystal fiber. *Science*, 298(5592):399–402, 2002.

[19] C. Wei, et al. Negative curvature fibers. *Adv. Opt. Photon.*, 9(3):504–561, Sep 2017.

[20] F. Yu, et al. Low loss silica hollow core fibers for 3–4 μm spectral region. *Opt. Express*, 20(10):11153–11158, May 2012.

[21] S.-f. Gao, et al. Hollow-core conjoined-tube negative-curvature fibre with ultralow loss. *Nature Communications*, 9(1):2828, Jul 2018.

[22] U. Dorda, et al. Status and objectives of the dedicated accelerator r& d facility sinbad at desy. *Nuclear Instruments and Methods in Physics Research Section A: Accelerators, Spectrometers, Detectors and Associated Equipment*, 909:239 – 242, 2018. 3rd European Advanced Accelerator Concepts workshop (EAAC2017).

[23] B. Marchetti, et al. Electron-beam manipulation techniques in the sinbad linac for external injection in plasma wake-field acceleration. *Nuclear Instruments and Methods in Physics Research Section A: Accelerators, Spectrometers, Detectors and Associated Equipment*, 829:278 – 283, 2016. 2nd European Advanced Accelerator Concepts Workshop - EAAC 2015.

[24] J. Zhu, et al. Sub-fs electron bunch generation with sub-10-fs bunch arrival-time jitter via bunch slicing in a magnetic chicane. *Phys. Rev. Accel. Beams*, 19:054401, May 2016.

[25] J. Zhu. *Design Study for Generating Sub-femtosecond to Femtosecond Electron Bunches for Advanced Accelerator Development at SINBAD.* Dissertation, University of Hamburg, 2017. Dissertation, University of Hamburg, 2017.

[26] N. Matlis, et al. Acceleration of electrons in thz driven structures for axsis. *Nuclear Instruments and Methods in Physics Research Section A: Accelerators, Spectrometers, Detectors and Associated Equipment*, 909:27 – 32, 2018. 3rd European Advanced Accelerator Concepts workshop (EAAC2017).

[27] F. Kärtner, et al. Axsis: Exploring the frontiers in attosecond x-ray science, imaging and spectroscopy. *Nuclear Instruments and Methods in Physics Research Section A: Accelerators, Spectrometers, Detectors and Associated Equipment*, 829:24 – 29, 2016. 2nd European Advanced Accelerator Concepts Workshop - EAAC 2015.

[28] N. Delbos, et al. Lux – a laser–plasma driven undulator beamline. *Nuclear Instruments and Methods in Physics Research Section A: Accelerators, Spectrometers, Detectors and Associated Equipment*, 909:318–322, 2018. 3rd European Advanced Accelerator Concepts workshop (EAAC2017).

[29] E. Panofski, et al. Status report of the SINBAD-ARES RF photoinjector and linac commissioning. *Journal of Physics: Conference Series*, 1350:012019, nov 2019.

[30] F. Lemery, et al. Overview of the ares bunch compressor at sinbad *. 05 2019.

[31] D. Marx, et al. Simulation studies for characterizing ultrashort bunches using novel polarizable x-band transverse deflection structures. *Scientific Reports*, 9(1):1–17, 2019.

[32] P. Craievich, et al. Novel x-band transverse deflection structure with variable polarization. *Physical Review Accelerators and Beams*, 23(11):112001, 2020.

[33] B. Marchetti, et al. Conceptual and technical design aspects of accelerators for external injection in lwfa. *Applied Sciences*, 8:757, 05 2018.

[34] K. Floettmann. Emittance compensation in split photoinjectors. *Phys. Rev. Accel. Beams*, 20:013401, Jan 2017.

[35] D. Lipka, et al. Dark current monitor for the european xfel. 2011.

[36] M. Ferrario, et al. Experimental demonstration of emittance compensation with velocity bunching. *Phys. Rev. Lett.*, 104:054801, Feb 2010.

[37] W. Kuropka. *Studies towards Acceleration of Relativistic Electron Beamsin Laser-driven Dielectric Microstructures*. Dissertation, Universität Hamburg, Hamburg, 2020. Dissertation, Universität Hamburg, 2020.

[38] D. Marx. *Characterization of Ultrashort Electron Bunches at the SINBAD-ARES Linac*. Dissertation, Universität Hamburg, Hamburg, 2019. Dissertation, Universität Hamburg, 2019.

[39] R. Akre, et al. A Transverse RF deflecting structure for bunch length and phase space diagnostics. *Conf. Proc. C*, 0106181:2353–2355, 2001.

[40] Acceleration on a chip program. `https://achip.stanford.edu/`.

[41] T. Plettner and R. L. Byer. Proposed dielectric-based microstructure laser-driven undulator. *Phys. Rev. ST Accel. Beams*, 11:030704, Mar 2008.

[42] K. Soong, et al. Electron beam position monitor for a dielectric microaccelerator. *Opt. Lett.*, 39(16):4747–4750, Aug 2014.

[43] F. Mayet, et al. Simulations and plans for possible dla experiments at sinbad. *Nuclear Instruments and Methods in Physics Research Section A: Accelerators, Spectrometers, Detectors and Associated Equipment*, 909:213 – 216, 2018. 3rd European Advanced Accelerator Concepts workshop (EAAC2017).

[44] E. Hemsing, et al. Beam by design: Laser manipulation of electrons in modern accelerators. *Reviews of Modern Physics*, 86(3):897, 2014.

[45] Accelerator research and innovation for european science and society. `https://aries.web.cern.ch/about-aries`.

[46] H2020 projects-aries. `https://eu-projektbuero.desy.de/h2020/h2020_projects/aries/index_eng.html`.

[47] Wikipedia-vsim. `https://en.wikipedia.org/wiki/VSim`.

[48] K. Floettmann. A space charge tracking algorithm. `https://www.desy.de/~mpyflo/`.

[49] Cudos mof utilities. http://www.physics.usyd.edu.au/~borisk/CUDOS_MOF_Utilities/index.php/Main_Page.

[50] The university of sydney. https://www.sydney.edu.au/science/our-research/research-areas/physics/eggleton-research-group.html.

[51] T. P. White, et al. Multipole method for microstructured optical fibers. i. formulation. *J. Opt. Soc. Am. B*, 19(10):2322–2330, Oct 2002.

[52] B. T. Kuhlmey, et al. Multipole method for microstructured optical fibers. ii. implementation and results. *J. Opt. Soc. Am. B*, 19(10):2331–2340, Oct 2002.

[53] Comsol multiphysics. https://www.comsol.com/.

[54] Max-planck-institute for the science of light-russel division. https://mpl.mpg.de/divisions/russell-division/.

[55] H. Wiedemann. *Particle accelerator physics: Third edition*. 01 2007.

[56] M. Martini. An introduction to transverse beam dynamics in accelerators. Technical Report CERN-PS-96-011-PA, CERN, Geneva, Mar 1996.

[57] K. Floettmann. Some basic features of the beam emittance. *Phys. Rev. ST Accel. Beams*, 6:034202, Mar 2003.

[58] J. Buon. Beam phase space and emittance; rev. version. (LAL-RT-90-15-REV. LAL-RT-92-03):27 p, Feb 1992.

[59] K. L. Brown and R. Servranckx. First- and second-order charged particle optics. *AIP Conf. Proc.*, 127:62–138, 1985.

[60] A. Latina. Introduction to transverse beam dynamics-lecture 5: Insertions / particle tracking / beam stability. 2015.

[61] P.Castro. Beam trajectory calculationsin bunch compressors of ttf2. *DESY-Technical Note TN-2003-01*, 2003.

[62] M. Reiser. *Theory and design of charged particle beams*. 5 1995.

[63] M. Ferrario, et al. Space Charge Effects. (arXiv:1601.05214. arXiv:1601.05214):331–356. 26 p, Jan 2016. 26 pages, contribution to the CAS - CERN Accelerator School: Advanced Accelerator Physics Course, Trondheim, Norway, 18-29 Aug 2013.

[64] T. P. Wangler. *Introduction to linear accelerators*. May 1998.

[65] N. Chauvin. Space-charge effect. *CAS-CERN Accelerator School: Ion Sources - Proceedings*, 10 2014.

[66] L. Serafini and J. B. Rosenzweig. Envelope analysis of intense relativistic quasilaminar beams in rf photoinjectors:ma theory of emittance compensation. *Phys. Rev. E*, 55:7565–7590, Jun 1997.

[67] C.-x. Wang. Universal envelope equation and emittance evolution of high-brightness beam in linac. *Phys. Rev. ST Accel. Beams*, 12:044201, Apr 2009.

[68] D. Alesini. Linac, 2021.

[69] F. Tecker. Longitudinal beam dynamics. *arXiv: Accelerator Physics*, pages 1–22, 2014.

[70] CERN. *CAS - CERN Accelerator School: Free Electron Lasers and Energy Recovery Linacs: CERN, Geneva, Switzerland 31 May - 10 Jun 2016. CAS - CERN Accelerator School: Free Electron Lasers and Energy Recovery Linacs*, Geneva, 2018. CERN.

[71] F. Tecker. Longitudinal beam dynamics. *arXiv preprint arXiv:1601.04901*, 2016.

[72] V. Paramonov and K. Floettmann. Fundamental characteristics of transverse deflecting field, 2019.

[73] E. A. J. Marcatili and R. A. Schmeltzer. Hollow metallic and dielectric waveguides for long distance optical transmission and lasers. *The Bell System Technical Journal*, 43(4):1783–1809, 1964.

[74] J. Stratton. *Electromagnetic Theory*. 1941.

[75] S. Frankel. Tm0,1 mode in circular wave guides with two coaxial dielectrics. *Journal of Applied Physics*, 18(7):650–655, 1947.

[76] J. D. Jackson. *Classical electrodynamics*. 1999.

[77] V. Paramonov and K. Floettmann. Fundamental characteristics of transverse deflecting field, 2019.

[78] P. Russell. A neat idea [photonic crystal fibre]. *IEE Review*, 47:19–23(4), September 2001.

[79] S. F.Poli, A. Cucinotta. *Photonic Crystal Fibers- Properties and Applications*. 2007.

[80] J. C. Knight, et al. All-silica single-mode optical fiber with photonic crystal cladding. *Opt. Lett.*, 21(19):1547–1549, Oct 1996.

[81] J. D. Joannopoulos, et al. *Photonic crystals - Molding the flow of light*. 2008.

[82] S. Libori. *Photonic crystal fibers -: from theory to practice*. PhD thesis, August 2002.

[83] T. A. Birks, et al. Endlessly single-mode photonic crystal fiber. *Opt. Lett.*, 22(13):961–963, Jul 1997.

[84] P. S. Russell. Photonic-crystal fibers. *J. Lightwave Technol.*, 24(12):4729–4749, Dec 2006.

[85] C. Croënne, et al. Band gaps in phononic crystals: Generation mechanisms and interaction effects. *AIP Advances*, 1, 12 2011.

[86] F. Poletti, et al. Hollow-core photonic bandgap fibers: Technology and applications. *Nanophotonics*, 2, 11 2013.

[87] P. Russell. Optics of floquet-bloch waves in dielectric gratings. *Applied Physics B*, 39:231–246, 1986.

[88] X. Zhang, et al. 7-cell hollow-core photonic bandgap fiber with broad spectral bandwidth and low loss. *Opt. Express*, 27(8):11608–11616, Apr 2019.

[89] B. J. Mangan, et al. Low loss (1.7 db/km) hollow core photonic bandgap fiber. In *Optical Fiber Communication Conference*, page PD24. Optical Society of America, 2004.

[90] A. A. Lanin, et al. Air-guided photonic-crystal-fiber pulse-compression delivery of multi-megawatt femtosecond laser output for nonlinear-optical imaging and neurosurgery. *Applied Physics Letters*, 100(10):101104, 2012.

[91] F. Couny, et al. Large-pitch kagome-structured hollow-core photonic crystal fiber. *Opt. Lett.*, 31(24):3574–3576, Dec 2006.

[92] G. J. Pearce, et al. Models for guidance in kagome-structured hollow-core photonic crystal fibres. *Opt. Express*, 15(20):12680–12685, Oct 2007.

[93] F. Couny, et al. Generation and photonic guidance of multi-octave optical-frequency combs. *Science*, 318(5853):1118–1121, 2007.

[94] J. . Archambault, et al. Loss calculations for antiresonant waveguides. *Journal of Lightwave Technology*, 11(3):416–423, 1993.

[95] N. M. Litchinitser, et al. Application of an arrow model for designing tunable photonic devices. *Opt. Express*, 12(8):1540–1550, Apr 2004.

[96] H. Stawska, et al. Anti-resonant hollow core fibers with modified shape of the core for the better optical performance in the visible spectral region-a numerical study. *Polymers*, 10:899, 08 2018.

[97] M. Hou, et al. Antiresonant reflecting guidance mechanism in hollow-core fiber for gas pressure sensing. *Opt. Express*, 24(24):27890–27898, Nov 2016.

[98] M. Duguay, et al. Antiresonant reflecting optical waveguides in sio2-si multilayer structures. *Applied Physics Letters*, 49(1):13–15, 1986. Copyright: Copyright 2007 Elsevier B.V., All rights reserved.

[99] M. Zeisberger and M. Schmidt. Analytic model for the complex effective index of the leaky modes of tube-type anti-resonant hollow core fibers. *Sci Rep 7, 11761*, 2017.

[100] L. Vincetti and L. Rosa. A simple analytical model for confinement loss estimation in hollow-core tube lattice fibers. *Opt. Express*, 27(4):5230–5237, Feb 2019.

[101] R. Beravat. *Twisted Photonic Crystal Fibers.* doctoralthesis, Friedrich-Alexander-Universität Erlangen-Nürnberg (FAU), 2018.

[102] M. Heiblum and J. Harris. Analysis of curved optical waveguides by conformal transformation. *IEEE Journal of Quantum Electronics*, 11(2):75–83, 1975.

[103] R. T. Schermer and J. H. Cole. Improved bend loss formula verified for optical fiber by simulation and experiment. *IEEE Journal of Quantum Electronics*, 43(10):899–909, 2007.

[104] M. H. Frosz, et al. Analytical formulation for the bend loss in single-ring hollow-core photonic crystal fibers. *Photon. Res.*, 5(2):88–91, Apr 2017.

[105] S. J. Garth. Birefringence in bent single-mode fibers. *Journal of Lightwave Technology*, 6(3):445–449, 1988.

[106] M. S. Alam, et al. High group birefringence in air-core photonic bandgap fibers. *Opt. Lett.*, 30(8):824–826, Apr 2005.

[107] V. Kaur and S. Singh. Extremely sensitive multiple sensing ring pcf sensor for lower indexed chemical detection. *Sensing and Bio-Sensing Research*, 15:12 – 16, 2017.

[108] K. Suzuki, et al. Optical properties of a low-loss polarization-maintaining photonic crystal fiber. *Opt. Express*, 9(13):676–680, Dec 2001.

[109] L. Genovese, et al. Tolerance Studies and Limitations for Photonic Bandgap Fiber Accelerators. pages 3605–3608. 10th International Particle Accelerator Conference, Melbourne (Australia), 19 May 2019 - 24 May 2019, JACoW Publishing, Geneva, Switzerland, May 2019.

[110] J. Breuer, et al. Dielectric laser acceleration of nonrelativistic electrons at a single fused silica grating structure: Experimental part. *Phys. Rev. ST Accel. Beams*, 17:021301, Feb 2014.

[111] R. J. Noble, et al. Hollow-core photonic band gap fibers for particle acceleration. *Phys. Rev. ST Accel. Beams*, 14:121303, Dec 2011.

[112] C.-K. Ng, et al. Transmission and radiation of an accelerating mode in a photonic band-gap fiber. *Phys. Rev. ST Accel. Beams*, 13:121301, Dec 2010.

[113] S. G. Johnson and J. D. Joannopoulos. Block-iterative frequency-domain methods for maxwell's equations in a planewave basis. *Opt. Express*, 8(3):173–190, Jan 2001.

[114] A. F. Oskooi, et al. Meep: A flexible free-software package for electromagnetic simulations by the fdtd method. *Computer Physics Communications*, 181(3):687 – 702, 2010.

[115] R. J. England, et al. Dielectric laser accelerators. *Rev. Mod. Phys.*, 86:1337–1389, Dec 2014.

[116] N. Kroll, et al. Photonic band gap structures: A new approach to accelerator cavities. *AIP Conference Proceedings*, 279(1):197–211, 1992.

[117] Vsim. `https://txcorp.com/vsim/`.

[118] R. J. England, et al. Input coupling for photonic bandgap fiber accelerators. *IEEE Journal of Selected Topics in Quantum Electronics*, 22(2):178–186, 2016.

[119] L. Allen, et al. Orbital angular momentum of light and the transformation of laguerre-gaussian laser modes. *Phys. Rev. A*, 45:8185–8189, Jun 1992.

[120] D. Naidoo, et al. Intra-cavity vortex beam generation. *Proceedings of SPIE - The International Society for Optical Engineering*, 8130, 09 2011.

[121] I. Kimel and L. Elias. Relations between hermite and laguerre gaussian modes. *IEEE Journal of Quantum Electronics*, 29(9):2562–2567, 1993.

[122] L. Genovese, et al. Attosecond bunch trains and sub-attosecond temporal resolutions with laser-driven anti-resonant fibers. *Submission on PRX ongoing.*

[123] P. Uebel, et al. Broadband robustly single-mode hollow-core pcf by resonant filtering of higher-order modes. *Opt. Lett.*, 41(9):1961–1964, May 2016.

[124] M. Hachmann and K. Flöttmann. Measurement of ultra low transverse emittance at regae. *Nuclear Instruments and Methods in Physics Research Section A: Accelerators, Spectrometers, Detectors and Associated Equipment*, 829, 09 2016.

[125] F. Lemery and P. Piot. Ballistic bunching of photoinjected electron bunches with dielectric-lined waveguides. *Phys. Rev. ST Accel. Beams*, 17:112804, Nov 2014.

[126] S. Antipov, et al. Experimental observation of energy modulation in electron beams passing through terahertz dielectric wakefield structures. *Phys. Rev. Lett.*, 108:144801, Apr 2012.

[127] P. Russell, et al. Hollow-core photonic crystal fibres for gas-based nonlinear optics. *Nature Photonics*, 8(4):278–286, April 2014.

[128] H. Lu, et al. The permanent magnet phase shifter for the european x-ray free electron laser. *Nuclear Instruments and Methods in Physics Research Section A: Accelerators, Spectrometers, Detectors and Associated Equipment*, 605(3):399–408, 2009.

[129] Y. Li and J. Pflüger. Investigation of the r56 of a permanent magnet phase shifter, Aug 2010.

[130] A. He, et al. Design of low energy bunch compressors with space charge effects. *Physical Review Special Topics - Accelerators and Beams*, 18, 01 2015.

[131] V. Paramonov. Field distribution analysis in deflecting structures, 2013.

[132] R. K. Li and P. Musumeci. Single-shot mev transmission electron microscopy with picosecond temporal resolution. *Phys. Rev. Applied*, 2:024003, Aug 2014.

[133] P. Denham and P. Musumeci. Space-charge aberrations in single-shot time-resolved transmission electron microscopy. *Phys. Rev. Applied*, 15:024050, Feb 2021.

[134] D. Xiang, et al. Accelerator-based single-shot ultrafast transmission electron microscope with picosecond temporal resolution and nanometer spatial resolution. *Nuclear Instruments and Methods in Physics Research Section A: Accelerators, Spectrometers, Detectors and Associated Equipment*, 759:74–82, 2014.

[135] S. V. Yalunin, et al. Tailored high-contrast attosecond electron pulses for coherent excitation and scattering. *Phys. Rev. Research*, 3:L032036, Aug 2021.

[136] M. Michieletto, et al. Hollow-core fibers for high power pulse delivery. *Opt. Express*, 24(7):7103–7119, Apr 2016.

[137] D. M. Simanovskii, et al. Midinfrared optical breakdown in transparent dielectrics. *Phys. Rev. Lett.*, 91:107601, Sep 2003.

[138] L. Gallais, et al. Wavelength dependence of femtosecond laser-induced damage threshold of optical materials. *Journal of Applied Physics*, 117(22):223103, 2015.

[139] E. G. Gamaly, et al. Ablation of solids by femtosecond lasers: Ablation mechanism and ablation thresholds for metals and dielectrics. *Physics of Plasmas*, 9(3):949–957, 2002.

[140] J. E. Sipe, et al. Laser-induced periodic surface structure. i. theory. *Phys. Rev. B*, 27:1141–1154, Jan 1983.

[141] J. Niu and J. Xu. Coupling efficiency of laser beam to multimode fiber. *Optics Communications*, 274:315–319, 06 2007.

[142] M. A. Habib, et al. Numerical modeling of a rectangular hollow-core waveguide for the detection of fuel adulteration in terahertz region. *Fibers*, 8(10), 2020.

[143] D. Wu, et al. Understanding the material loss of anti-resonant hollow-core fibers. *Opt. Express*, 28(8):11840–11851, Apr 2020.

[144] G. Humbert, et al. Hollow core photonic crystal fibers for beam delivery. *Opt. Express*, 12(8):1477–1484, Apr 2004.

[145] L. Michaille, et al. Damage threshold and bending properties of photonic crystal and photonic band-gap optical fibres. *Proceedings of SPIE - The International Society for Optical Engineering*, 5618, 11 2004.

[146] I. A. Bufetov and E. M. Dianov. Optical discharge in optical fibers. *Physics-Uspekhi*, 48(1):91–94, jan 2005.

[147] I. A. Bufetov, et al. Catastrophic damage in hollow core optical fibers under high power laser radiation. *Opt. Express*, 27(13):18296–18310, Jun 2019.

[148] A. Dergachev. High-energy, kHz-rate, picosecond, 2-μm laser pump source for mid-IR nonlinear optical devices. In *Proc. SPIE 8599, Solid State Lasers XXII: Technology and Devices*, page 85990B, March 2013.

[149] K. Murari, et al. Intracavity gain shaping in millijoule-level, high gain ho:ylf regenerative amplifiers. *Opt. Lett.*, 41(6):1114–1117, Mar 2016.

[150] C. Mahnke, et al. A passively mode-locked holmium fiber oscillator based on a nonlinear amplifying loop mirror operating at 2050 nm. *EPJ Web of Conferences*, 243:04002, 01 2020.

[151] I. Hofmann. Emittance Growth. In *13th International Linear Accelerator Conference*, pages TU2–1, 1986.

[152] F. J. Sacherer. Rms envelope equations with space charge. *IEEE Transactions on Nuclear Science*, 18(3):1105–1107, 1971.

[153] D. Moehl. Transverse dynamics ii : Emittances. `https://cas.web.cern.ch/sites/cas.web.cern.ch/files/lectures/zeegse-2005/moehl-final.pdf`.

[154] D. Moehl. Sources of emittance growth. 2006.

[155] T. Birks, et al. Full 2-d photonic bandgaps in silica/air structures. *Electronics Letters*, 31:1941 – 1943, 11 1995.

[156] N. M. Litchinitser, et al. Antiresonant reflecting photonic crystal optical waveguides. *Opt. Lett.*, 27(18):1592–1594, Sep 2002.

[157] S. Yerolatsitis, et al. Birefringent anti-resonant hollow-core fiber. *J. Lightwave Technol.*, 38(18):5157–5162, Sep 2020.

[158] F. Lemery, et al. Synchronous acceleration with tapered dielectric-lined waveguides. *Phys. Rev. Accel. Beams*, 21:051302, May 2018.

[159] W. Kuropka, et al. Full pic simulation of a first achip experiment @ sinbad. *Nuclear Instruments and Methods in Physics Research Section A: Accelerators, Spectrometers, Detectors and Associated Equipment*, 909:193 – 195, 2018. 3rd European Advanced Accelerator Concepts workshop (EAAC2017).

[160] S. Davtyan, et al. Polarization-tailored raman frequency conversion in chiral gas-filled hollow-core photonic crystal fibers. *Phys. Rev. Lett.*, 122:143902, Apr 2019.

[161] G. K. L. Wong, et al. Excitation of orbital angular momentum resonances in helically twisted photonic crystal fiber. *Science*, 337(6093):446–449, 2012.

[162] R. Ulrich and A. Simon. Polarization optics of twisted single-mode fibers. *Appl. Opt.*, 18(13):2241–2251, Jul 1979.

[163] X. Ma, et al. Angular-momentum coupled optical waves in chirally-coupled-core fibers. *Opt. Express*, 19(27):26515–26528, Dec 2011.

[164] M. Xu, et al. Continuous-wave mid-infrared gas fiber lasers. *IEEE Journal of Selected Topics in Quantum Electronics*, 24(3):1–8, 2018.

[165] E. Hass. *Longitudinal Electron Bunch Shape Reconstruction from Form Factor Modulus based on Spectrally Resolved Measurements of Coherent Transition Radiation.* Dissertation, Universität Hamburg, Hamburg, 2018. Dissertation, Universität Hamburg, 2018.

[166] O. Grimm and P. Schmüser. Principles of longitudinal beam diagnostics with coherent radiation. *TESLA-FEL Report (2006),*, 01 2006.

[167] F. Lemery. *Beam manipulation and acceleration with Dielectric-Lined Waveguides.* PhD thesis, Northern Illinios U., 2015.

[168] K. Murari, et al. Kagome-fiber-based pulse compression of mid-infrared picosecond pulses from a ho:ylf amplifier. *Optica*, 3(8):816–822, Aug 2016.

[169] D. Grojo, et al. Long-wavelength multiphoton ionization inside band-gap solids. *Phys. Rev. B*, 88:195135, Nov 2013.

[170] E. Esarey, et al. Physics of laser-driven plasma-based electron accelerators. *Rev. Mod. Phys.*, 81:1229–1285, Aug 2009.

[171] E. Saldin, et al. Longitudinal space charge-driven microbunching instability in the tesla test facility linac. *Nuclear Instruments and Methods in Physics Research Section A: Accelerators, Spectrometers, Detectors and Associated Equipment*, 528(1):355–359, 2004. Proceedings of the 25th International Free Electron Laser Conference, and the 10th FEL Users Workshop.

[172] G. Stupakov. Using the beam-echo effect for generation of short-wavelength radiation. *Phys. Rev. Lett.*, 102:074801, Feb 2009.

[173] E. Hemsing, et al. Echo-enabled harmonics up to the 75th order from precisely tailored electron beams. *Nature Photonics*, 10(8):512–515, Aug 2016.

[174] P. Rebernik Ribič, et al. Coherent soft x-ray pulses from an echo-enabled harmonic generation free-electron laser. *Nature Photonics*, 13(8):555–561, Aug 2019.

[175] E. Hemsing and D. Xiang. Cascaded modulator-chicane modules for optical manipulation of relativistic electron beams. *Phys. Rev. ST Accel. Beams*, 16:010706, Jan 2013.

[176] N. Sudar, et al. High efficiency energy extraction from a relativistic electron beam in a strongly tapered undulator. *Phys. Rev. Lett.*, 117:174801, Oct 2016.

[177] N. Sudar, et al. Demonstration of cascaded modulator-chicane microbunching of a relativistic electron beam. *Phys. Rev. Lett.*, 120:114802, Mar 2018.

[178] N. Kroll, et al. Free-electron lasers with variable parameter wigglers. *IEEE Journal of Quantum Electronics*, 17(8):1436–1468, 1981.

Publications

1. L. Genovese, et al. Attosecond bunch trains and sub-attosecond temporal resolutions with laser-driven anti-resonant fibers. *Submission on PRX ongoing*

2. E. Panofski, et al. Commissioning results and electron beam characterization at the s-band photoinjector at sinbad-ares, 2021

3. L. Genovese, et al. Tolerance Studies and Limitations for Photonic Bandgap Fiber Accelerators. pages 3605–3608. 10th International Particle Accelerator Conference, Melbourne (Australia), 19 May 2019 - 24 May 2019, JACoW Publishing, Geneva, Switzerland, May 2019

Acknowledgements

This work of thesis wouldn't be possible without the support of many people. I would like to thank Dr. Ralph W. Assmann and Prof. Wolfgang Hillert for advising my thesis and give me the opportunity to work in one of the most inspiring environment in world wide. I want to thanks my previous supervisor Dr. Ulrich Dorda for the many fruitful discussions.

I would like to express my gratitude to my mentor and office mate Dr. Francois Lemery. He always pushed me in the right direction. He was an inspiration with his physical understanding and enthusiasm. I would like to thank Dr. Frank Mayet who was always ready to answer my countless questions about different topics.

Also, I would like to thank all my colleagues from MPY-1, in particular Dr. Klauss Floettmann, Dr. Thomas Vinatier, Dr. Willi Kuropka, Dr. Florian Burkart and Max Kellermeier. I am grateful for having had the opportunity to work into laser laboratory. It would not be possible without the supervision of Dr. Huseyin Cankaya. I learned a lot from his passion and experience.

I would like to thank Prof. Dr. Philip Russell and his team at Max Planck Institute for the Science of Light in Erlangen. Their support and the constructive discussions make this work possible.

Special thanks goes to the European Union's Horizon 2020 Research and Innovation program for funding this project (Grant Agreement No 730871).

Last, but not least, I have to thank my family. The constant support of my wife Marina was fundamental during my PhD, especially in the dark situation of the pandemic crisis. It can't rain all the time!

E a te piccola Francesca, GRAZIE!!!

Eidesstattliche Versicherung

Hiermit versichere ich an Eides statt, die vorliegende Dissertationsschrift selbst verfasst und keine anderen als die angegebenen Hilfsmittel und Quellen benutzt zu haben. Die eingereichte schriftliche Fassung entspricht der auf dem elektronischen Speichermedium. Die Dissertation wurde in der vorgelegten oder einer ähnlichen Form nicht schon einmal in einem früheren Promotionsverfahren angenommen oder als ungenügend beurteilt.

Ort, Datum	Unterschrift